

# High Power Laser Processing of Semiconductor Germanium for Optoelectronic Devices

---

A Dissertation

Presented to  
the faculty of the School of Engineering and Applied Science  
University of Virginia

---

in partial fulfillment  
of the requirements for the degree

Doctor of Philosophy

by

Keye Sun

August

2015

APPROVAL SHEET

The dissertation  
is submitted in partial fulfillment of the requirements  
for the degree of  
Doctor of Philosophy

---

AUTHOR

The dissertation has been read and approved by the examining committee:

Mool. C. Gupta

---

Advisor

Lloyd R. Harriott

---

Arthur W. Lichtenberger

---

Andreas Beling

---

Joshua Choi

---

Accepted for the School of Engineering and Applied Science:



Dean, School of Engineering and Applied Science

August  
2015

## Abstract

Recently germanium semiconductor material is receiving renewed interest both in microelectronic and optoelectronic applications. Due to its higher carrier mobilities than silicon, germanium is a candidate for high speed metal oxide semiconductor field effect transistors. Also germanium can effectively absorb near infrared light, so it has applications in near infrared optoelectronic devices. The germanium-based photodetectors, imaging sensors and thermophotovoltaic devices have been widely investigated.

Conventional fabrication steps of germanium-based optoelectronic and microelectronic devices include surface microtexturing, doping, surface antireflection coating and metallization. Unlike silicon, the process steps for germanium are neither well established nor fully understood. Among them, two critical steps are surface microtexturing and doping. The special material properties of germanium result in lots of challenges in these two steps. Cost-effective methods for microtexturing of germanium surface for reflection reduction do not exist. Problems such as dopant out-diffusion, substrate loss and shallow junction formation occur for conventional doping methods. These challenges encountered by conventional fabrication methods can be effectively overcome by laser-based methods.

In addition, the performance of germanium-based optoelectronic devices still needs to be improved further in order to stand out among devices based on other materials. Chalcogen hyperdoping has been proven to bring high photo-gain and sub-bandgap photoresponse to silicon-based photodiodes. Since germanium and silicon are similar materials, chalcogen hyperdoping can be expected to be a potential way to improve the performance of germanium-based optoelectronic devices. This hyperdoping can only be achieved by means of short pulsed

lasers due to the fast heating and cooling process which results in super-saturation of chalcogen atoms in the semiconductor material.

In this work, laser microtexturing method was developed to reduce the optical reflection over broad spectral and angular range and good performance of germanium photodetector was demonstrated. Secondly, the formation of germanium p-n junction was demonstrated by means of pulsed laser doping process and the performance was characterized. Lastly, sulfur as a deep level dopant was incorporated into germanium by short pulsed laser and from which a photodiode was fabricated. The novel photodiode based on sulfur-doped germanium showed higher external quantum efficiency than conventional germanium photodetectors over broad spectral range. We have demonstrated that pulsed laser can be effectively used to enhance performance of Ge optoelectronic devices and for the development of novel device concepts.

## **Acknowledgement**

I would like to thank my advisor professor Mool. C. Gupta for his encouragement, advice and support during as I pursue my Ph.D. degree.

I would like to thank professor Joe C. Campbell for the permission to use their equipment.

I would like to thank the NASA Langley Professor program and the NSF IUCRC programs for their support of my research project.

I would like to thank my friend and group members for the helpful discussion and help.

Lastly, I would like to thank my family and friends for their help and support throughout the time. Without them, I couldn't finish my Ph.D. study.

# Contents

<b>List of Figures</b> .....	iii
<b>List of Tables</b> .....	ix
<b>Chapter 1: Introduction: Ge-based Semiconductor Devices and Laser-Based Fabrication</b> ..	1
1.1 Renewed interest in germanium.....	1
1.2 Challenges for Ge-based optoelectronic devices fabrication.....	3
1.3 Laser-based fabrication for microelectronic and optoelectronic devices .....	5
1.4 Objective of this research.....	6
1.5 Organization of the dissertation .....	7
<b>Chapter 2: Laser Microtexturing of Germanium for Broad Wavelength Photodetector Applications</b> .....	9
2.1 Introduction.....	9
2.2 Experimental .....	10
2.2.1 Laser microtexturing of Ge.....	10
2.2.2 Photodiode fabrication on laser microtextured Ge .....	11
2.3 Results and discussion .....	12
2.3.1 Laser microtexturing of Ge surfaces.....	12

2.3.2 Optical and structural properties of microtextured Ge surfaces .....	16
2.3.3 Device results.....	22
2.4 Summary .....	31
<b>Chapter 3: Laser Doping of Ge for Microelectronic and Photonic Device Applications.....</b>	<b>32</b>
3.1 Introduction.....	32
3.2 Ge n <sup>+</sup> -p junction formation and photodiode fabrication .....	35
3.3 Results and discussion .....	36
3.4 Summary .....	45
<b>Chapter 4: Sulfur-Hyperdoping of Germanium by Pulsed Laser .....</b>	<b>47</b>
4.1 Introduction.....	47
4.2 Experimental .....	48
4.2.1 S doping .....	48
4.2.2 Photodiode fabrication.....	49
4.3 Results and Discussion .....	50
4.3.1 Results of device hyperdoped using 532 nm wavelength nanosecond pulsed laser .....	50
4.3.2 S doping profile.....	52
4.3.3 Effects of thermal activation .....	54

4.3.4 Results of devices on 10 ~ 15 $\Omega$ -cm wafer hyperdoped using 1064 nm wavelength nanosecond pulsed laser .....	56
4.3.5 Results of devices on undoped wafer and hyperdoped using 1064 nm nanosecond laser .....	66
4.3.6 DLTS results .....	70
4.4 Summary .....	71
<b>Chapter 5: Conclusion and Future Work.....</b>	<b>73</b>
5.1 Conclusion .....	73
5.2 Future work.....	75
5.2.1 Ge device with nanoscale textured surface .....	75
5.2.2 Sub-bandgap optical absorption of S-hyperdoped Ge .....	77
5.2.3 Determination of sulfur defect levels.....	80
5.2.4 Investigation of the physical mechanism for lower photo-gain of device based on S-hyperdoped Ge .....	81
<b>Chapter 6: Laser Sintering of Silicon Nanoparticles for Photovoltaic Applications .....</b>	<b>82</b>
6.1 Introduction.....	82
6.2 Experimental .....	83
6.3 Results and discussion .....	84

6.3.1 Si nanoparticle sintering .....	84
6.3.2 Device characterization.....	87
6.4 Summary .....	91
<b>Bibliography</b> .....	<b>93</b>
<b>List of Publications</b> .....	<b>104</b>

## List of Figures

### Chapter 2

- Fig. 2.1. SEM images of Ge surfaces after laser treatment at different power densities (a) 0.68 J/cm<sup>2</sup> (b) 0.9 J/cm<sup>2</sup> (c) 2.6 J/cm<sup>2</sup> .....13
- Fig. 2.2. Evolution of surface structures under laser power density about 1.9 J/cm<sup>2</sup> as number of laser shots increases (a) 27 shots (b) 40 shots (c) 67 shots (d) 80 shots. ....14
- Fig. 2.3. SEM images of surface morphology microtextured Ge surfaces under laser power density of 2.3 J/cm<sup>2</sup> for (a) 40, (b) 29 and (c) 22 laser shots. The corresponding cross sectional SEM images for 40, 29 and 22 laser shots are shown in (d), (e) and (f). .....15
- Fig. 2.4. (a) Total integrated scattering of laser-microtextured Ge surface and flat surface. (b) Total integrated scattering of laser-microtextured Ge surface at different incident angle. ....16
- Fig. 2.5. XRD results of microtextured Ge and chemically-etched microtextured Ge. The inset shows the magnified plot of Ge (100) peak. ....18
- Fig. 2.6. Total integrated light scattering of microtextured Ge surface after various amount of chemical etching. ....19
- Fig. 2.7. SEM images of the laser-microtextured Ge surfaces after different amount of chemical etch (a) as-microtextured (b) 6 minutes (c) 15 minutes (d) 20 minutes (e) 30 minutes and (f) 50 minutes. ....20
- Fig. 2.8. (a) Dark I-V characteristics of mesa device with SiO<sub>2</sub> and Si<sub>3</sub>N<sub>4</sub> coatings on it. (b) Schematic shows the mechanism of inverted surface layer caused by Si<sub>3</sub>N<sub>4</sub> layer. The white

positive signs indicate the accumulated positive charges at the interface between $\text{Si}_3\text{N}_4$ layer and Ge. The red arrows indicate the current path way through the inverted surface layer. ....	21
Fig. 2.9. Optical reflection of flat and laser-microtextured surfaces before and after $\text{SiO}_2$ deposition.....	22
Fig. 2.10. SEM images of (a) 2 minutes (b) 30 minutes and (c) 50 minutes post-microtexture etched Ge surface.....	23
Fig. 2.11. Optical reflection of flat and microtextured Ge surface (a) without $\text{SiO}_2$ coating (b) with 100 nm $\text{SiO}_2$ ARC layer on top. ....	24
Fig. 2.12. (a) I-V characteristics of devices with flat, 30 minutes and 50 minutes post-microtexture etched surfaces. Device mesa size was 180 $\mu\text{m}$ in diameter. (b) Plots of dark current at -1 V bias as a function of mesa diameter. ....	26
Fig. 2.13. Schematic shows the shadowing effect during ion implantation. The red arrow indicates the incoming ions. The red circles indicate the possible regions which are shaded from incoming ions. Those areas are also likely to have insufficient capping layers. ....	26
Fig. 2.14. Calculation of activation energy from the dark current at -1 V at various temperatures. ....	27
Fig. 2.15. EQE at -1 V bias for the flat and microtextured device. ....	28
Fig. 2.16. Junction capacitance of 180 $\mu\text{m}$ mesa device as a function of reverse bias voltage. ....	29
Fig. 2.17. (a) Transient response to the 1550 nm wavelength picosecond laser pulse under -1 V bias. (b) -3 dB bandwidth determined by Fast Fourier transform of the transient response. Mesa size is 180 $\mu\text{m}$ in diameter. ....	30

### Chapter 3

- Fig. 3.1. SEM image of morphology of the Ge surface after thermal diffusion with high concentration SOD (P509) at 580 °C for 4 minutes. ....34
- Fig. 3.2. SEM images of Ge surface morphology after laser doping at laser energy density of (a) 2.65 J/cm<sup>2</sup> (b) 1.77 J/cm<sup>2</sup> and (c) 0.85 J/cm<sup>2</sup>. ....37
- Fig. 3.3. Phosphorus doping profile obtained by SIMS measurements and qualitative calculation. The carrier concentration of the p-type Ge substrate was  $5 \times 10^{16}$  atoms/cm<sup>3</sup>. The junction depth was 850 nm. ....38
- Fig. 3.4. (a) I-V characteristics of n<sup>+</sup>-p junctions formed by laser-doping and rapid thermal diffusion process. (b) Numerical fitting of n<sup>+</sup>-p junctions of 180 μm mesa diameter formed by laser-doping and rapid thermal diffusion process. ....41
- Fig. 3.5. Dark current as a function of the mesa radius for the SiO<sub>2</sub>-passivated Ge photodetectors with laser-doped junctions. ....42
- Fig. 3.6. (a) Dark current at different temperature. The arrow indicates the varying temperature from 220 K to 300 K in step of 20 K. (b) Activation energy of dark current at -1 V bias for Ge n<sup>+</sup>-p junction mesa device formed by laser-doping. ....43
- Fig. 3.7. I-V characteristics of Ge photodetector with laser-doped junction under dark and 1.55 μm wavelength light illumination. ....44
- Fig. 3.8. (a) Transient response of the Ge photodetector of 130 μm mesa diameter to a 1.55 μm wavelength picosecond laser pulse under 0 V bias condition, and (b) Fourier transform of the

transient response. Dash line is for thermally diffused device and solid line is for laser-doped device.....45

## Chapter 4

Fig. 4.1. (a) I-V characteristics of S-doped Ge photodiode using a 532 nm wavelength nanosecond pulsed laser. (b) SEM images of the mesa device.....51

Fig. 4.2. Black material deposited on the quartz cover slide during thermal activation at 300 °C for 2 minutes. The black material in the red circle is speculated to be out-diffused sulfur.....52

Fig. 4.3. S doping profile obtained by SIMS measurement for the laser-hyperdoped Ge sample before and after thermal annealing. ....54

Fig. 4.4. Dark I-V characteristics of devices that underwent (a) no activation and 500 °C, (b) 300 °C and 400 °C 2 minutes activation.....55

Fig. 4.5. I-V characteristics of S-doped Ge photodiode of mesa diameter 180 μm fabricated on 10 ~ 15 Ω·cm p-type Ge wafer using different laser fluence.....57

Fig. 4.6. I-V characteristics of S-doped Ge photodiode of mesa diameter 500 μm. The inset shows the circuit schematic of the device.....58

Fig. 4.7. (a) EQE of S-doped Ge photodiode fabricated on 10 ~ 15 Ω·cm resistivity Ge wafers using different laser fluences. (b) Optical reflection of Ge with 100 nm SiO<sub>2</sub> ARC. ....61

Fig. 4.8. EQE of S-doped Ge photodiode fabricated on different resistivity Ge wafers at various reverse bias voltages. EQE of a commercial Ge photodetector is also shown in the figure.....61

Fig. 4.9. Temporal response of S-doped Ge photodiode hyperdoped using laser fluences of (a)  $2.0 \text{ J/cm}^2$ , (b)  $2.3 \text{ J/cm}^2$  and (c)  $2.6 \text{ J/cm}^2$  to a picosecond laser pulse of 1330 nm wavelength at 0.2 and 0.5 V reverse bias voltage. ....63

Fig. 4.10. -3 dB bandwidth of the S-doped photodiode calculated from Fourier transform of the temporal response. ....64

Fig. 4.11. Transient response of the device to a 100 ns laser pulse of 1310 nm wavelength. ....66

Fig. 4.12. (a) I-V characteristics of S-doped Ge photodiode of mesa diameter  $180 \text{ }\mu\text{m}$  on undoped Ge wafer using different laser fluence. (b) Schematics of the three devices in (a). ....68

## Chapter 5

Fig. 5.1. (a) microtextured Ge surface before applying P507. (b) after applying P507. ....76

Fig. 5.2. (a) microtextured Ge surface before applying P509. (b) after applying P509. (c) after thermal diffusion at  $580 \text{ }^\circ\text{C}$  for 2 minutes and removal of P509 coating. ....76

Fig. 5.3. Experimental setup for sub-bandgap optical absorption measurement. ....80

## Chapter 6

Fig. 6.1. Morphology of sintered layer under different incident laser power (a) 4 W (b) 6 W (c) 8 W (d) 10 W (e) 12 W (f) 14 W (g) cross section of laser-sintered sample using 14 W. ....85

Fig. 6.2. XRD results of (100) c-Si substrate, raw coating and sintered sample. ....86

Fig. 6.3. IQE of the devices with sintered and standard emitter. ....87

Fig. 6.4. Base minority carrier lifetime of the device with sintered and standard emitter. ....89

Fig. 6.5. Laser-induced melting pool at the interface. The melted pools are labeled by red circles and the blue arrows indicate the laser scan path. ....89

Fig. 6.6. LBIC results of the device with laser-sintered emitter. The solid black regions are the front metal contact areas. The inset shows the magnified image. ....91

## List of Tables

### Chapter 3

Table 3.1. Sheet resistance values at different laser power density.....	37
--	----

### Chapter 4

Table 4.1. EQE at -0.5 V bias of three different types of S-hyperdoped Ge device at four different wavelength. ....	68
---	----

Table 4.2. DLTS result of trap levels in S-hyperdoped Ge photodiode. ....	71
---	----

### Chapter 5

Table 5.1 Optical absorption measurement of S-hyperdoped Ge samples at 2.35 $\mu\text{m}$ wavelength. ....	80
--	----

## **Chapter 1:**

# **Introduction: Ge-based Semiconductor Devices and Laser-Based Fabrication**

### **1.1 Renewed interest in germanium**

Germanium (Ge) is one of the oldest semiconductor materials. After the invention of the first solid state diode, Ge was a dominant semiconductor material for solid state devices. In the 1950s, the Ge diodes were widely used in various applications including radios, telephone exchanges, radar receivers, etc. Ge was soon replaced by silicon (Si) in the late 1950s due to its more stabilized surface. After the invention of metal-oxide-semiconductor field effect transistor (MOSFET), Si became the indispensable material in electronic industries because of several facts as stated below. The main reason for this transition from Ge to Si was the lack of effective surface passivation methods. It is well known that a working MOSFET depends heavily on the good passivation of semiconductor surfaces on the channel region. In the case of Si, thermally grown  $\text{SiO}_2$  provides excellent passivation on Si surfaces. However,  $\text{GeO}_2$  is water soluble and thermally unstable and hence the  $\text{GeO}_2/\text{Ge}$  system cannot be used as a straightforward analog of the  $\text{SiO}_2/\text{Si}$  system. The ineffective surface passivation causes the lower inversion channel mobility of the Ge MOSFETs than their Si counterparts in spite of the higher intrinsic carrier mobility of Ge. The ill-passivated Ge surface can even make the gate terminal lose control of the channel region, which in turn causes the failure of the device. In addition to surface passivation,

another major bottleneck towards high performance Ge CMOS is the poor quality of n<sup>+</sup>-p junctions. For modern CMOS technology, very shallow junctions with high level of dopant activation are required. This is very challenging for Ge n<sup>+</sup>-p junctions. There exists a trade-off between the dopant out-diffusion during the ion implantation defects thermal annealing and the formation of shallow junctions with little residual defects. Finally, the low cost of Si material due to its abundance makes it preferable than Ge from economical point of view. All these facts make the CMOS technology rely mostly on Si instead of Ge.

Recently, Ge has been gaining a great deal of renewed interest. The everlasting need for faster speed and lower power consumption of computing hardware leads to the miniaturization of transistors on chips. As the size becomes smaller, the manufacturing cost rises higher. An alternative route to increase the device speed, while keeping the manufacturing cost low, is to fabricate large devices using semiconductor materials with higher carrier mobilities. Ge has much higher carrier mobility (3900 cm<sup>2</sup>/V s for electrons and 1900 cm<sup>2</sup>/V s for holes) than Si (1450 cm<sup>2</sup>/V s for electrons and 500 cm<sup>2</sup>/V s for holes) [1]. It therefore possesses a great potential for high speed MOSFETs. Recently effective ways of passivating Ge surface by GeO<sub>2</sub> [2] or GeON [3] have been demonstrated and considerable success has been achieved to realize Ge-based MOSFETs [4, 5]. Furthermore, the first CMOS circuit based on Ge has been demonstrated recently [6]. Consequently, Ge is seriously considered as a candidate to replace Si for the next generation integrated circuits. Not only in microelectronics, Ge is widely used in optoelectronic devices as well. It can effectively absorb near infrared (IR) light, and thus has many applications in near IR photodetectors and imaging devices. Both epitaxial Ge layers on Si [7, 8] and Ge bulk photodetectors [9, 10] have been extensively investigated. Compared to photodetectors based on epilayers of III-V semiconductors [11, 12], the cost of the bulk Ge

photodetector is lower because of the material and the fabrication process. Thus, monolithic integration of Ge-based electronic circuits and optoelectronic devices on a single Ge chip for various applications such as photonic integrated circuits seems promising.

## **1.2 Challenges for Ge-based optoelectronic devices fabrication**

The conventional process flow of fabricating a p-n junction photodetector or solar cell includes surface microtexturing, doping, surface passivation and metallization. As a thoroughly investigated material, the Si process flow is well established. Although Si and Ge are the same group elements, they differ a lot in their physical and chemical properties. As a result, the conventional Si process flow cannot be directly applied to Ge. The Ge process flow is neither fully understood nor well established. Among the conventional fabrication steps, two critical steps are surface microtexturing and doping. The less favorable material properties of Ge cause lots of challenges in these two processing steps, some of which will be addressed below.

First, the surface of the wafer is usually microtextured for some optoelectronic devices such as solar cells and photodetectors as a way to reduce the optical reflection. Chemical microtexturing is a well-established low-cost method for Si. However, to our knowledge, there is no low cost way of surface microtexturing of Ge using methods like chemical microtexturing. Thus effective surface microtexturing method needs to be investigated to improve the Ge-based optoelectronic devices.

Second, ion implantation is the conventional method for creating junctions in integrated circuit fabrication. Thermal annealing is needed to eliminate the defects caused by the violent bombardment of dopant ions and restore the crystalline structures. This process step is less well

known for Ge than for Si. Various problems such as dopant out-diffusion [13], Ge substrate loss [13] and fast diffusion of n-type dopants [13] need to be overcome to form high quality junctions.

These challenges encountered by conventional processing method during Ge device fabrication can be effectively overcome by laser-based methods. Laser-based microtexturing can provide an effective and low-cost way to fabricate Ge surfaces with extremely low optical reflection over a broad spectral and incidence angular range. Laser-based doping method can effectively avoid the problems in ion implantation process.

Besides the unfavorable material properties of Ge which needs to be overcome during the fabrication, the performance of the Ge-based devices still needs to be improved in order to stand out among other competitors in addition to the cost advantage. The dark current needs to be reduced further and the quantum efficiency should be further improved. Although conventional Ge photoconductors have a high photoconductive gain, they are notorious for high dark current and not suitable for many sensitive applications. Alternative effective methods to improve the performance of Ge-based optoelectronic devices are highly desired. Chalcogen element hyperdoping in Si have been widely investigated [14]. The ultrafast laser microtexturing of Si in SF<sub>6</sub> environment generates intermediate energy bands to achieve optical absorption up to around 4 μm in wavelength, which is well beyond the bandgap of bulk Si [15]. Moreover, rectifying junctions have been formed based on the chalcogen-incorporated Si due to the donor nature of the chalcogen impurities. Photodetectors based on chalcogen-incorporated Si material have demonstrated high photo-gain [16]. This hyperdoping can only be achieved by means of short pulsed laser since only the ultrafast heating and cooling process can cause supersaturation of chalcogen dopant atoms in Si. Since Ge and Si are similar semiconductor materials, chalcogen

hyperdoping by means of short pulsed laser can be expected to enhance the Ge-based optoelectronic device performance.

### **1.3 Laser-based fabrication for microelectronic and optoelectronic devices**

Lasers are optical sources that have high output power and excellent coherence. They are very suitable for precise material processing. Nowadays significant success has been realized in high power lasers in terms of low cost per photon, availability of high power continuous wave and pulsed lasers and high wall plug efficiency. All these facts rationalize the industrial laser-based manufacturing. Due to the advantages such as localized heating, non-contact processing, low environment temperature processing, the laser-based processing is an ideal approach for semiconductor device fabrication. It is believed to be an effective way of fabrication of microelectronic and optoelectronic devices with low cost. It is a well-known fact that lasers have already been utilized in ion implantation damage annealing, solar cell device fabrication such as edge isolation [17], selective emitter formation [18], module level patterning [19], drilling holes for emitter-wrap-through solar cell [20]. More importantly, by means of short pulsed lasers, not only the manufacturing cost can be potentially reduced, many optoelectronic devices with novel functionality and high performance can be realized which cannot be achieved with conventional processing methods. The ultrafast heating and cooling characteristics of laser material interaction result in special optical and electronic properties of the material processed by short pulsed lasers. Thus, pulsed lasers are becoming a unique tool to realize some novel optoelectronic devices.

### **1.4 Objective of this research**

To overcome the challenges for Ge-based semiconductor devices fabrication as well as to achieve high performance Ge-based optoelectronic devices, laser-based fabrication methods are very promising alternative routes. The primary objective of this research is to investigate the laser-based methods as an effective way to overcome the difficulties in Ge-based device fabrication as well as to improve the performance of Ge-based devices. To be specific, short pulsed lasers were investigated for three areas of Ge-based device fabrication:

1. Reduction of optical reflection at the incident surface is very critical to achieve high performance optoelectronic devices. Traditional anti-reflection coating using dielectric layers is only effective in a narrow spectral range. Surface microtexturing is an effective way to reduce the optical reflection over a broad spectral range and the resulting low surface reflection is insensitive to the incident angle. Unfortunately, there is no well-established cost-effective way to microtexture Ge surfaces. To find a cost-effective way of microtexturing Ge surface, short pulsed laser-based method needs to be investigated. The benefit of surface microtexturing in terms of improved Ge photodiodes performance needs to be demonstrated.
2. Challenges such as dopant out-diffusion, Ge substrate loss and shallow junction formation make it difficult to form high quality Ge junctions by traditional doping methods. In order to demonstrate an effective doping method which can circumvent these problems, laser-based doping process was investigated. High quality Ge junctions need to be realized by means of short pulsed laser doping. The quality of the junction needs to be characterized by devices based on laser-formed Ge junction.
3. Although Ge-based photodiode has the advantage of material and fabrication cost, the performance still needs to be improved in order to win over the photodetectors based on other materials. Especially the dark current needs to be reduced and the quantum efficiency

needs to be further improved. Sulfur (S) hyperdoping has been proven to be effective in improving the quantum efficiency of Si-based photodiode. The incorporated sulfur dopants in Si result in 20X gain in photo-response in the visible region. Moreover, photo-response in sub-bandgap wavelength spectrum is also observed. Since Ge and Si are similar semiconductor materials, S hyperdoping can be expected to enhance the performance of Ge-based photodiode as well as to extend the photo-response beyond Ge bandgap. In order to achieve high gain and sub-bandgap photo-response, S hyperdoping in Ge by short pulsed laser needs to be demonstrated as an effective method. The physical mechanism for this performance improvement needs to be explained.

## **1.5 Organization of the dissertation**

Chapter 1 provides an introduction of laser-based fabrication method in Ge-based optoelectronic devices and describes briefly the main objectives of this research.

Chapter 2 describes the laser microtexturing of Ge surfaces and the performance of photodiode fabricated on microtextured surfaces.

Chapter 3 presents Ge n-p junction formed by laser doping process and the junction performance is characterized.

Chapter 4 describes the experiments for laser hyperdoping of S in Ge and the improved performance of Ge photodiode is characterized.

Chapter 5 discusses the conclusion and future work.

Additional research work that has been accomplished during the course of this work is discussed in chapter 6.

## Chapter 2:

# Laser Microtexturing of Germanium for Broad Wavelength Photodetector Applications

## 2.1 Introduction

Owing to its higher carrier mobilities and low bandgap (0.66 eV), Ge has wide applications in high speed optoelectronic devices in the near IR range. Both epitaxial Ge layer on Si [7, 8] and Ge bulk photodetectors [9, 10] have been extensively investigated. Compared to photodetectors based on epilayers of III-V semiconductors [11, 12], the cost of the bulk Ge photodetector is relatively low because of the material itself and the compatible process flow with conventional Si CMOS technology. One drawback of the Ge is its high refractive index ( $n \approx 4$ ) [1] which causes the high optical reflection and thus the low performance of the Ge photodetectors. Anti-reflection coatings (ARC) using dielectric layers are only effective over a narrow spectrum. Multiple dielectric layers can reduce the reflection over a wider spectrum but it requires high-cost deposition equipment and expensive maintenance due to toxic and flammable gases used. Surface microtexturing is another traditional method to reduce the reflection. Reflection can be reduced over a broad spectrum and even at large incident angles [21]. Surface microtexturing can be achieved in many ways such as chemical texturing [22], natural lithography [23 - 25]. Compared to other techniques, laser microtexturing is low-cost and chemical-free. It can achieve extremely low reflection over a broad wavelength and selective

microtexturing without masking. The surface morphology can also be controlled by laser processing conditions. Laser microtexturing has been applied to different materials such as metals [26], Si [27] and Ge [28]. Optoelectronic devices with laser-microtextured surfaces such as Si solar cells [29] and photodetectors [30] showed good performance. Laser microtexturing has special value to Ge. To the best of our knowledge, there are no low cost ways of microtexturing Ge surfaces like chemical microtexturing, laser seems to be the only effective and low-cost method. Despite of several reports in the literature on microtexturing of Ge, no optoelectronic device that utilizes microtexturing have been reported. In this work, microtextured Ge surfaces were achieved by a pulsed laser. More importantly, the benefits of microtexturing were demonstrated, for the first time, by realization of Ge photodetectors with laser-microtextured surfaces. Devices with microtextured surfaces exhibit an average about 15% higher external quantum efficiency (EQE) over a broad spectrum compared to devices with flat surfaces with other characteristics such as dark current density and speed similar.

## **2.2 Experimental**

### **2.2.1 Laser microtexturing of Ge**

A pulsed nanosecond laser (IPG GLP-10, wavelength 532 nm, 1 nanosecond pulse width) was used for microtexturing Ge. The Ge sample was placed on a stage and the laser beam was scanned across the wafer by means of a galvometer. The laser power density and number of laser shots received by every spot on the wafer can be controlled by varying the percentage of the laser output power and the scan speed of the laser beam. The surface morphology was examined

by scanning electron microscopy (SEM). Crystal structures were characterized by X-ray diffraction (XRD).

### 2.2.2. Photodiode fabrication on laser microtextured Ge

P-type Ge wafer (400  $\mu\text{m}$  thick,  $\langle 100 \rangle$ , resistivity  $\rho = 0.07 \text{ ohm}\cdot\text{cm}$ ) was purchased from Umicore Inc. The wafer was cleaned subsequently in  $\text{NH}_4\text{OH} : \text{H}_2\text{O}_2$ ,  $\text{HCl} : \text{H}_2\text{O}_2$  and diluted HF. The wafer was then laser microtextured. The laser beam was focused to a spot with energy density of approximately  $2.3 \text{ J}/\text{cm}^2$ . The laser beam was scanned across the wafer by means of a galvanometer. Every spot on the wafer underwent about 50 laser shots. After microtexturing, the samples were chemically etched in  $\text{NH}_4\text{OH} + \text{H}_2\text{O}_2 + \text{DI}$  solution for 2, 30 and 50 minutes to remove the laser-induced damage layer.

For  $\text{n}^+\text{-p}$  junction formation, room temperature ion implantation of phosphorus was carried out on laser-microtextured surface at implantation energy of 45 keV and a dose of  $6 \times 10^{15} \text{ cm}^{-2}$ . The implantation was done at  $7^\circ$  tilt to avoid channeling effect. After the ion implantation, a 50 nm  $\text{SiO}_2$  layer was deposited by plasma enhanced chemical vapor deposition (PECVD) to avoid dopant loss during annealing step [31]. Samples were annealed at  $600^\circ \text{C}$  for 2 minutes in vacuum using a rapid thermal annealing (RTA) system to remove the ion-implantation-induced defects. The mesa structure was formed by inductively coupled plasma etch. The etch conditions were: a  $\text{O}_2$  flow rate of 5 sccm, a  $\text{SF}_6$  flow rate of 20 sccm, an RIE power of 120 W, an ICP power of 200 W, and a pressure of 10 mTorr. Mesa diameters of 500  $\mu\text{m}$ , 350  $\mu\text{m}$ , 250  $\mu\text{m}$  and 180  $\mu\text{m}$  were formed through photolithography step. The height of the mesa was about 3  $\mu\text{m}$ . After the dry etch, the initial  $\text{SiO}_2$  capping layer was removed and a fresh 100 nm  $\text{SiO}_2$  film was

deposited by PECVD as an ARC layer. Both n-type and p-type contacts were patterned by photolithography. A stack of Ti/Au (20 nm/120 nm) was deposited by electron beam evaporation. Finally the contacts were thickened to approximately 8  $\mu\text{m}$  for devices that underwent 2 minutes post-microtexture etch and to 3  $\mu\text{m}$  for ones that underwent 30 and 50 minutes post-microtexture etch by electroplating of Au.

## **2.3 Results and discussion**

### **2.3.1 Laser microtexturing of Ge surfaces**

The laser power density is a critical parameter for forming cone-like microtexture morphology. The surface morphology under different laser power density is shown in Fig. 2.1. If the laser power density is too low, only shallow melting occurs. If the laser power density is too high, the laser beam ablates the material and causes deep grooves instead of forming conical microtexture features. The laser power density therefore needs to be above the melting threshold ( $\sim 1 \text{ J/cm}^2$  at 532 nm wavelength) while below the ablation threshold for Ge in order to create the conical structures.

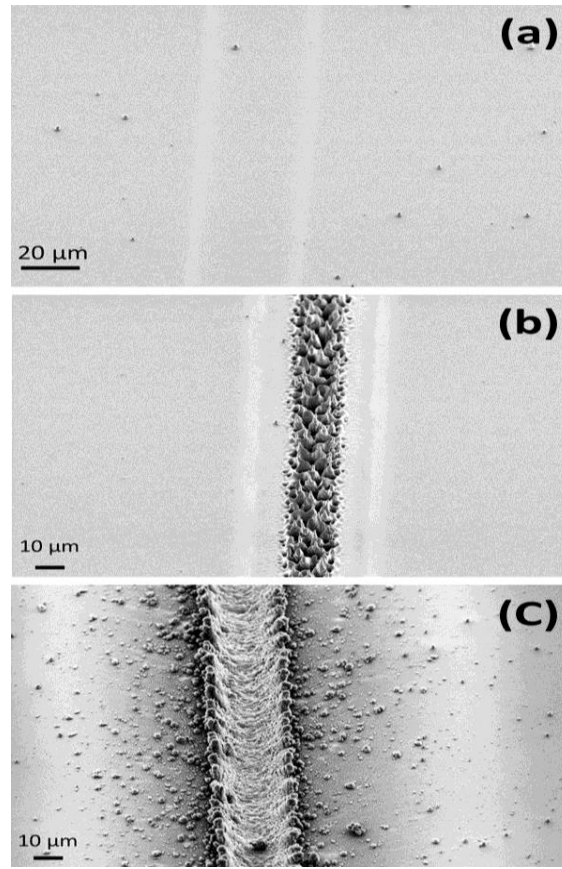


Fig. 2.1. SEM images of Ge surfaces after laser treatment at different power densities (a)  $0.68 \text{ J/cm}^2$  (b)  $0.9 \text{ J/cm}^2$  (c)  $2.6 \text{ J/cm}^2$ .

When the laser power density is in the appropriate range, the number of laser shots received by every spot on the wafer plays an important role. The evolution of the microtexture morphology at different number of laser shots under laser power density of  $1.9 \text{ J/cm}^2$  is shown in Fig. 2.2. When the number of laser shots is low, small circular waves are generated from random spots due to non-uniformities on micro-scale on the wafer as shown in Fig. 2.2 (a). When the number of laser shots increases, the circular waves propagate and interfere with each other and upon receiving more laser shots, small cone-like structures evolves. As a result of fast

solidification of the material, the conical structures retain their shape permanently after the laser pulse ends, as shown in Fig. 2.2 (b). Following the formation of initial small structures, subsequent pulses just sharpen and deepen these cones as shown in Fig. 2.2 (c) and (d). Also it can be seen in the SEM images that the tips and valleys in the microtexture are above and below the original surface level, which indicates that the major forming mechanism is actually due to melting and solidification rather than ablation of the material as observed for the femtosecond laser microtexturing [32].

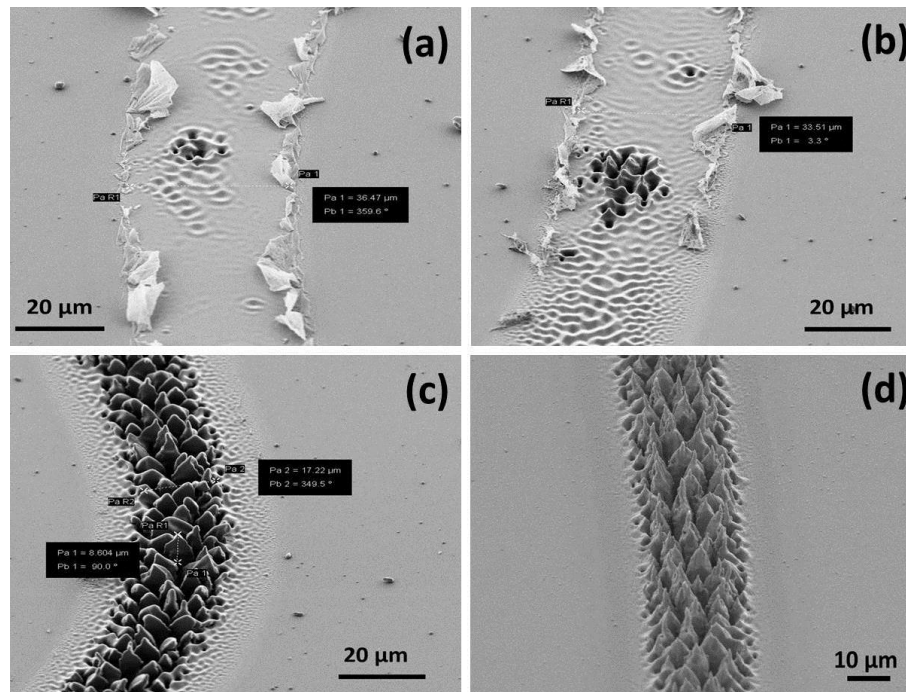


Fig. 2.2. Evolution of surface structures under laser power density about  $1.9 \text{ J/cm}^2$  as number of laser shots increases (a) 27 shots (b) 40 shots (c) 67 shots (d) 80 shots.

The evolution of the surface structure is about the same for different laser power density within the microtexture formation window. Only less number of laser shots is needed for the

formation of these microtexture morphologies under higher laser power densities. The SEM images of large area microtexturing under laser power density of  $2.3 \text{ J/cm}^2$  at different number of laser shots are shown in Fig. 2.3. The number of laser shots needed to evolve microtexture structures is less since the laser power density is larger. Also shown in the figure are the cross sectional SEM images corresponding to each number of laser shots. It has been observed that the height of the microtexture structures increases as the number of laser shots increases.

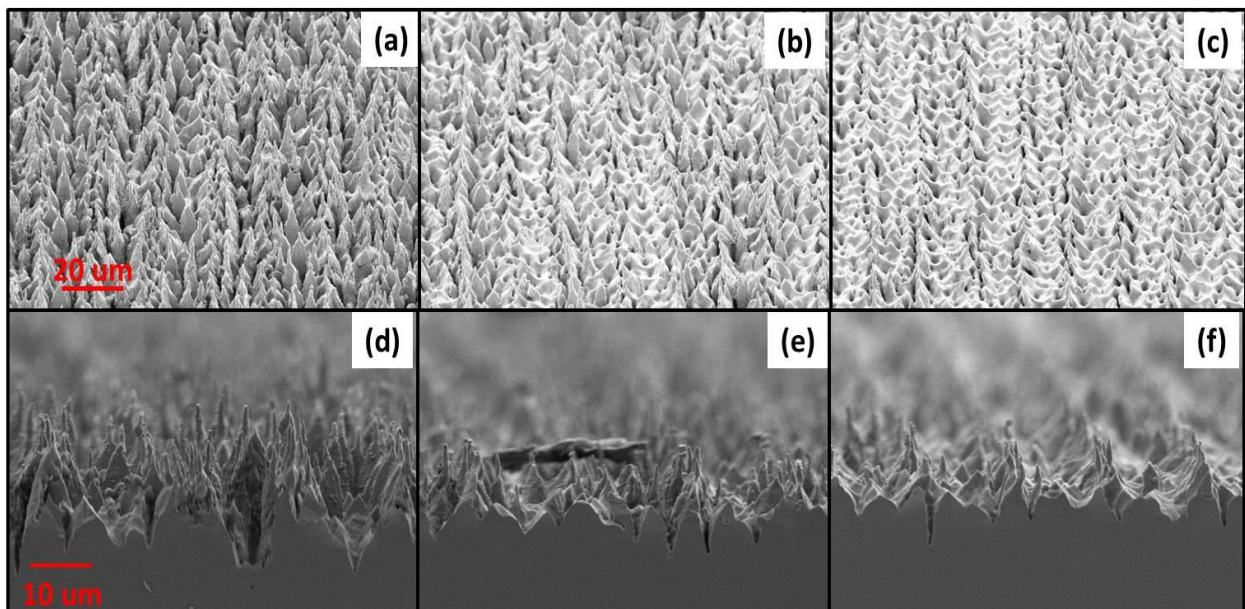


Fig. 2.3. SEM images of surface morphology microtextured Ge surfaces under laser power density of  $2.3 \text{ J/cm}^2$  for (a) 40, (b) 29 and (c) 22 laser shots. The corresponding cross sectional SEM images for 40, 29 and 22 laser shots are shown in (d), (e) and (f).

### 2.3.2 Optical and structural properties of microtextured Ge surfaces

The total integrating light scattering (sum of specular reflection, scattering) was measured by an integrating sphere (Model#RTC-060-SF, Labshpere Inc.). Individual laser diodes of different wavelength (850 nm, 980 nm, 1310 nm and 1550 nm) were used as the light sources. A Ge detector (model#818-IR-L, Newport Corp.) was used to measure the optical power. The results are shown in Fig. 2.4 (a). The optical reflection of Ge surface is reduced from 40% for the polished surface to as low as 8% for the microtextured surface. This shows that the laser microtexturing can effectively reduce the optical reflection of Ge surfaces over a broad spectrum. Moreover, the reflection remains below 8% at an incident angle from  $5^\circ$  to  $40^\circ$  for different wavelength as shown in Fig. 2.4 (b), which indicates that the low optical reflection is insensitive to incident angle.

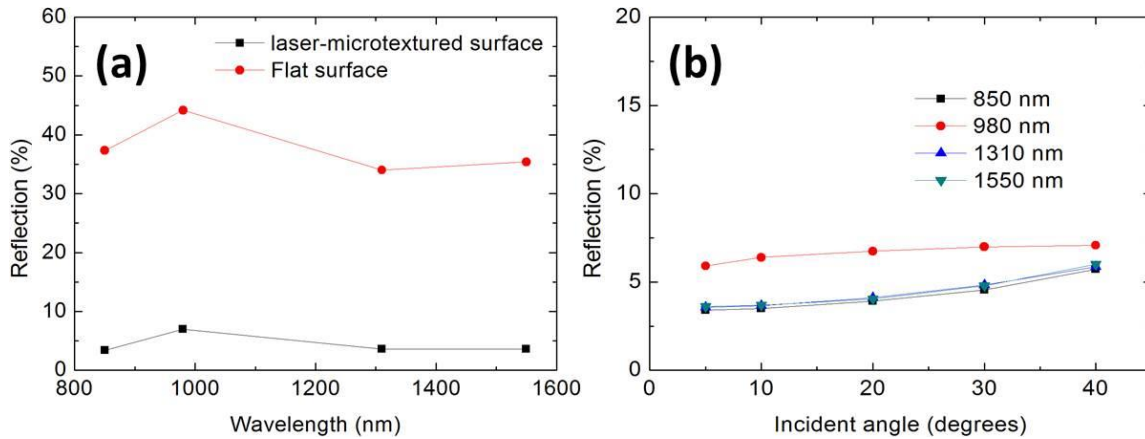


Fig. 2.4. (a) Total integrated scattering of laser-microtextured Ge surface and flat surface. (b) Total integrated scattering of laser-microtextured Ge surface at different incident angle.

The optical property of the microtextured surface is greatly improved in terms of the reduction of total integrating light scattering. In order to apply in optoelectronic devices, the electronic property of the microtextured surfaces is also very important and the effect of laser microtexturing on electronic property needs to be investigated. During the laser microtexturing, crystal defects are created in the material due to the violent interaction between the laser beam and the material. Also the microtexturing was done in the air environment, impurities will be introduced into the material such as oxygen, nitrogen, carbon, etc. A chemical etch is needed to remove the damage and contaminant layer. After laser microtexturing, the samples were chemically etched in  $\text{NH}_4\text{OH} + \text{H}_2\text{O}_2 + \text{DI}$  solution for various amount of time to remove the surface layer which contains the laser-induced defects and impurities. The crystalline quality after chemical etch was examined by XRD and the results are shown in Fig. 2.5. The as-microtextured and chemically-etched microtextured Ge showed a major (100) peak. The inset of Fig. 2.5 shows the magnified plot of the (100) peak. Since longer chemical etch removed more damaged portion, the residue stress, defects and impurities left in the material reduces as the chemical etch is done for a longer time and thus the crystalline quality is more restored to the virgin material. This is indicated by the reduction of the (100) peak width after the chemical etch. The chemical etch can effectively improve the crystalline structure of the microtextured material and thus the electronic properties.

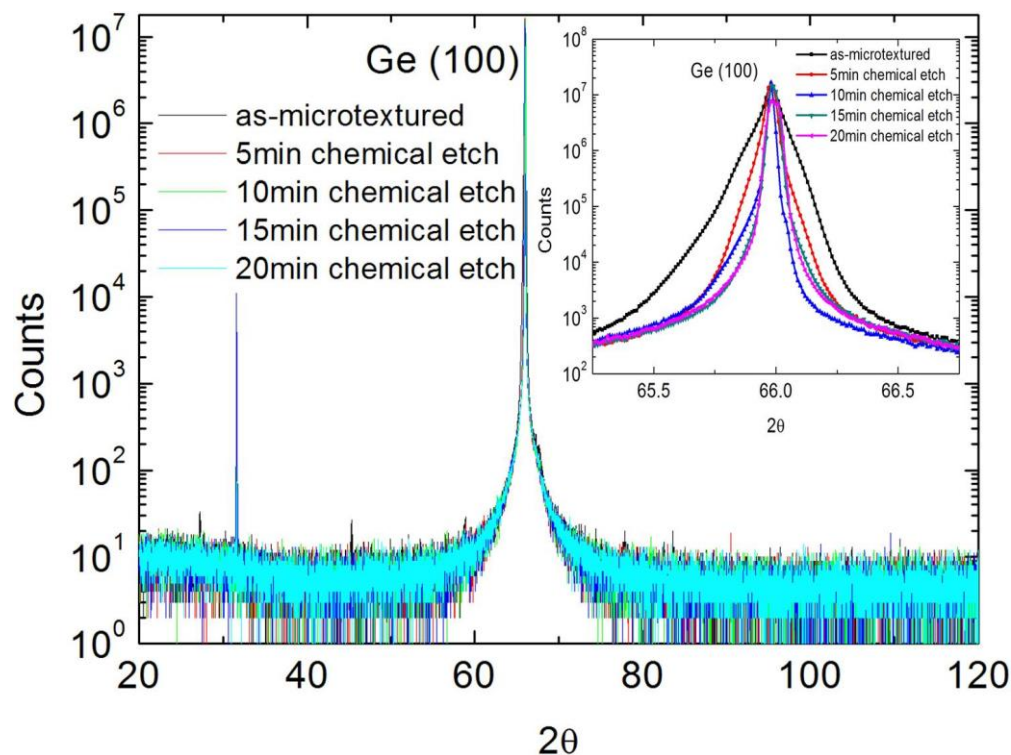


Fig. 2.5. XRD results of microtextured Ge and chemically-etched microtextured Ge. The inset shows the magnified plot of Ge (100) peak.

As the crystalline structure is improved after removal of damaged material by chemical etch, the optical reflection increases as a result of smoothening of the surface. The total integrated scattering is measured for each chemical etch time and the results are shown in Fig. 2.6. The corresponding surface morphologies are shown in Fig. 2.7. As can be seen, the optical reflection increases when the chemical etch time increases since the microtexture structures become shallower and smoother. Thus the number of reflection before the light bounces back into the air is reduced, which increases the optical reflection. As a result, there exists a trade-off between better optical properties and better electronic properties of the microtextured material. A

balance between greater absorption of incident light and better extraction of the photo-generated carriers needs to be found for optoelectronic device applications.

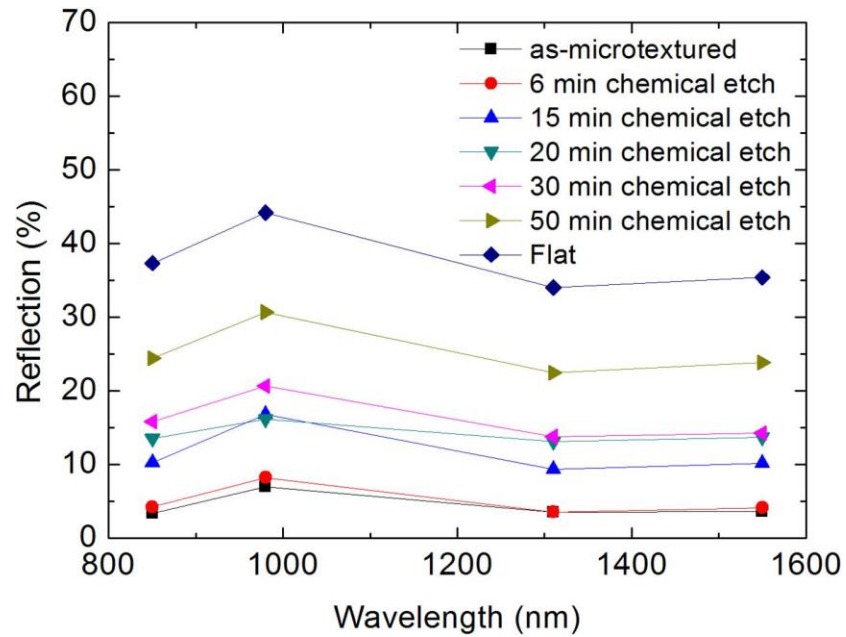


Fig. 2.6. Total integrated light scattering of microtextured Ge surface after various amount of chemical etching.

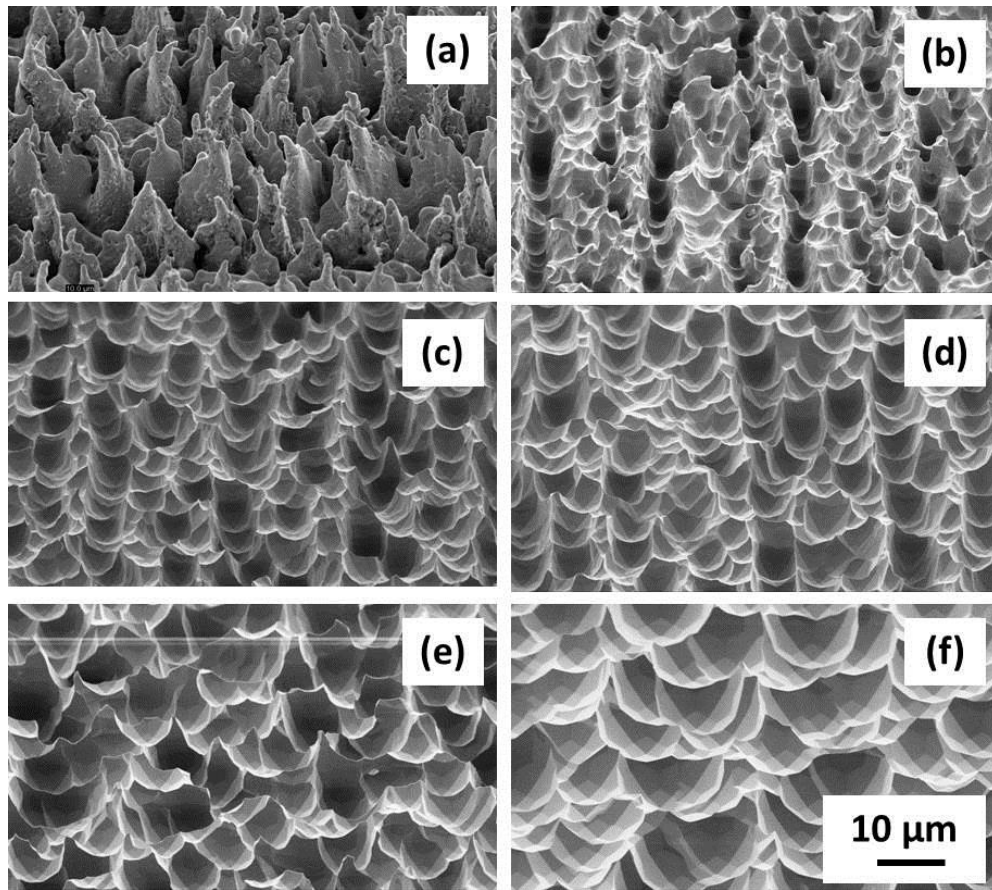


Fig. 2.7. SEM images of the laser-microtextured Ge surfaces after different amount of chemical etch (a) as-microtextured (b) 6 minutes (c) 15 minutes (d) 20 minutes (e) 30 minutes and (f) 50 minutes.

The crystalline quality improves after the chemical etching. As a trade-off, the optical reflection increases. Another way to lower the reflection further is to deposit an additional ARC layer. The traditional dielectric materials for ARC are  $\text{SiO}_2$  and  $\text{Si}_3\text{N}_4$ . Theoretically speaking,  $\text{Si}_3\text{N}_4$  is a better material for ARC on Ge since it has higher refractive index ( $\sim 1.9$ ) than  $\text{SiO}_2$  ( $\sim 1.46$ ). But in our experiments, 100 nm  $\text{SiO}_2$  was used instead of 70 nm  $\text{Si}_3\text{N}_4$  because the devices with  $\text{Si}_3\text{N}_4$  ARC suffered shunt problems as shown in Fig. 2.8 (a). The speculated reason

is explained below and schematically shown in Fig. 2.8 (b) [33]. Positive charges accumulate at the interface between Ge and  $\text{Si}_3\text{N}_4$  dielectric layer. These positive charges invert the side wall of the mesa and could create a n-type surface layer. Surface leakage current can flow through this inverted surface layer and may cause shunting problem. In order to use  $\text{Si}_3\text{N}_4$  as ARC, a different deposition recipe is needed to avoid the build-up of positive charge at the interface. The reflection of the flat and laser-microtextured surfaces before and after  $\text{SiO}_2$  deposition is shown in Fig. 2.9. As can be seen, the reflection can be brought down by around 20% for the flat surface and around 10% for the laser-microtextured surfaces.

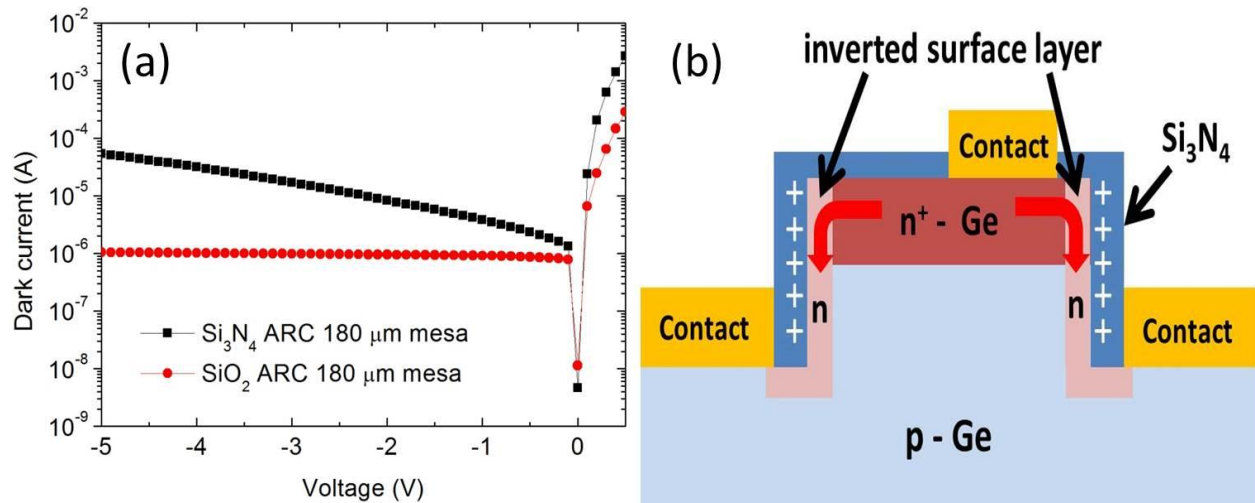


Fig. 2.8. (a) Dark I-V characteristics of mesa device with  $\text{SiO}_2$  and  $\text{Si}_3\text{N}_4$  coatings on it. (b) Schematic shows the mechanism of inverted surface layer caused by  $\text{Si}_3\text{N}_4$  layer. The white positive signs indicate the accumulated positive charges at the interface between  $\text{Si}_3\text{N}_4$  layer and Ge. The red arrows indicate the current path way through the inverted surface layer.

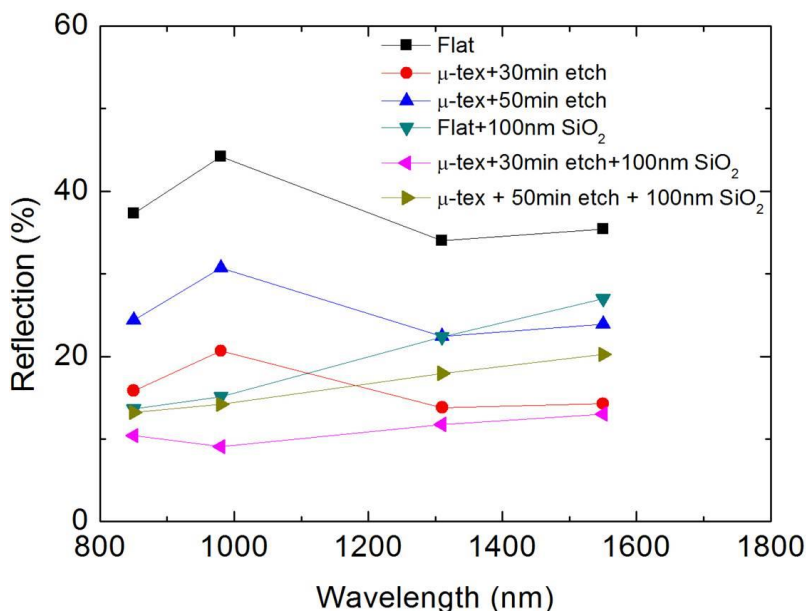


Fig. 2.9. Optical reflection of flat and laser-microtextured surfaces before and after SiO<sub>2</sub> deposition.

### 2.3.3 Device results

The microtextured surface morphology after 2, 30 and 50 minutes chemical etch was examined by SEM and the images are shown in Fig. 2.10. As shown in the figure, the structures on microtextured surface that has undergone 2 minutes post-microtexture etch have an average height of about 14  $\mu\text{m}$ . The structures have blunt and round tips and steep edges. The surface that has undergone 30 minutes post-microtexture etch had an average height of about 10  $\mu\text{m}$  and the tips of structure became sharp. It also had sharp edges and deep valleys. The surface that underwent 50 minutes post-microtexture etch had an average height of about 4  $\mu\text{m}$ . The tips and edges of the structures were not as sharp as the surface that had undergone 30 minutes etch. The crystallographic planes became obvious.

The optical reflection was measured using an integrated sphere at four wavelengths. The results are shown in Fig. 2.11. The reflection of the surface that underwent 2 minutes post-microtexture is much lower than for the flat surface. With longer etching time, the reflection becomes higher which is resulted from the reduction in surface roughness. With 100 nm SiO<sub>2</sub> ARC layer, the overall reflection is reduced.

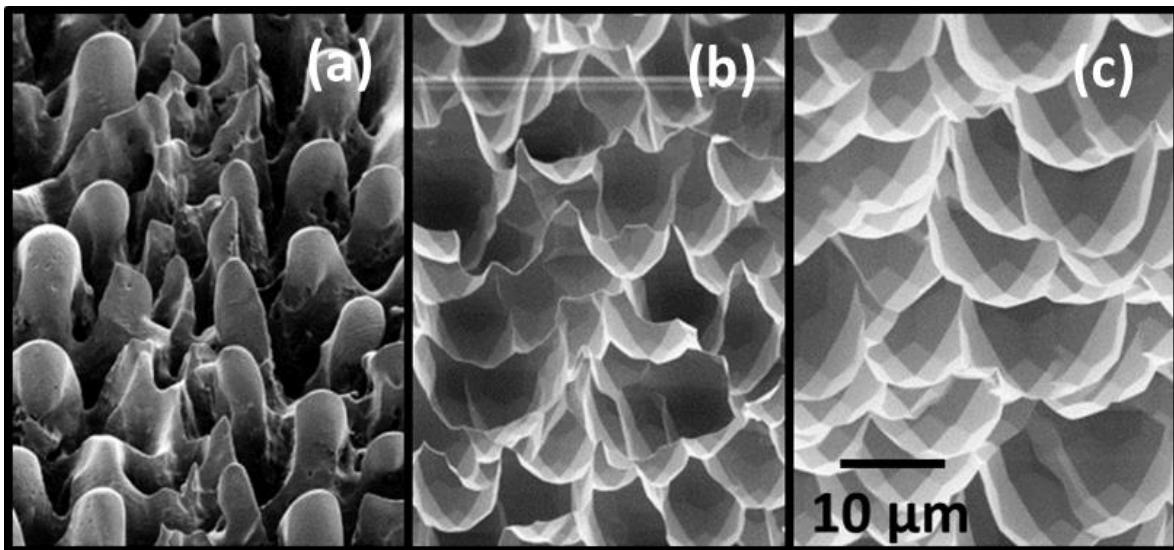


Fig. 2.10. SEM images of (a) 2 minutes (b) 30 minutes and (c) 50 minutes post-microtexture etched Ge surface.

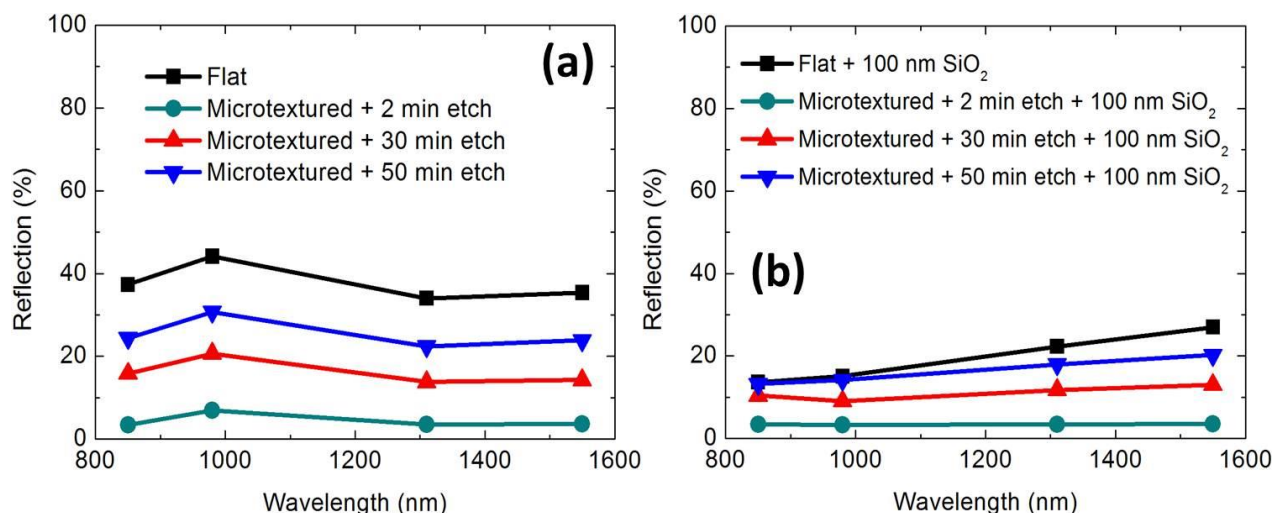


Fig. 2.11. Optical reflection of flat and microtextured Ge surface (a) without SiO<sub>2</sub> coating (b) with 100 nm SiO<sub>2</sub> ARC layer on top.

The dark current (I) – bias voltage (V) characteristic of the Ge p-n junction photodetector is shown in Fig. 2.12 (a). The dark current of device on surface that underwent 2 minutes post-microtexture etch is almost four orders of magnitude higher than other devices. The device suffered small shunt resistance. The possible reasons for this high dark current and small shunt resistance are explained as follows. Since the edges of the microtexture structures are very steep, the edges don't receive enough effective ion doses due to the small effective cross-sectional area facing the incoming ion beam during the ion implantation. This causes the low dopant concentration on these regions. The situation is worsened by the fact that the ion implantation was done at 7° tilt to avoid the channeling effect. As a result, some steep edge regions were shaded from the incoming ions by the blunt and round tips of the microtexture structures and thus these steep edges are lack of dopant atoms. Furthermore, the SiO<sub>2</sub> capping layer which was used to prevent the dopant out-diffusion was not uniformly deposited by the PECVD especially

on the steep edges. There could be very thin or even no capping layers on the steep edges. The dopant out-diffusion could be significant in those regions during the subsequent ion implantation damage annealing. Consequently, dopant concentration was further reduced on those steep edges where the doping level was already very low due to the shadowing effect. Combining the shadowing effect during the ion implantation and dopant out-diffusion due to the insufficient capping layer, the steep edges may act as local shunt path which cause the small shunt resistance and thus the high dark current. The situation is schematically showed in Fig. 2.13. Although the surface that underwent 2 minutes post-microtexture etch had the lowest optical reflection, the performance of the resulting device was poor. The surface morphology has a great impact on the final device performance and a trade-off between optical and electrical performance needs to be balanced.

The dark current for the other three devices had the same trend. The dark current remains flat from 0 V to -2 V and grow up exponentially at higher reverse bias voltage. The dark current at -1 V bias of different mesa sizes was investigated and the results are shown in the Fig. 2.12 (b). The dark current was approximately proportional to the mesa size which indicates that the dark current at -1 V bias was mainly from the sidewall. So the dark current values are very close for the three different devices. The flat device had the lowest dark current since it has the least front surface and junction area. The device which underwent 30-minute post-microtexture etch had the most front surface and junction area and hence the largest dark current.

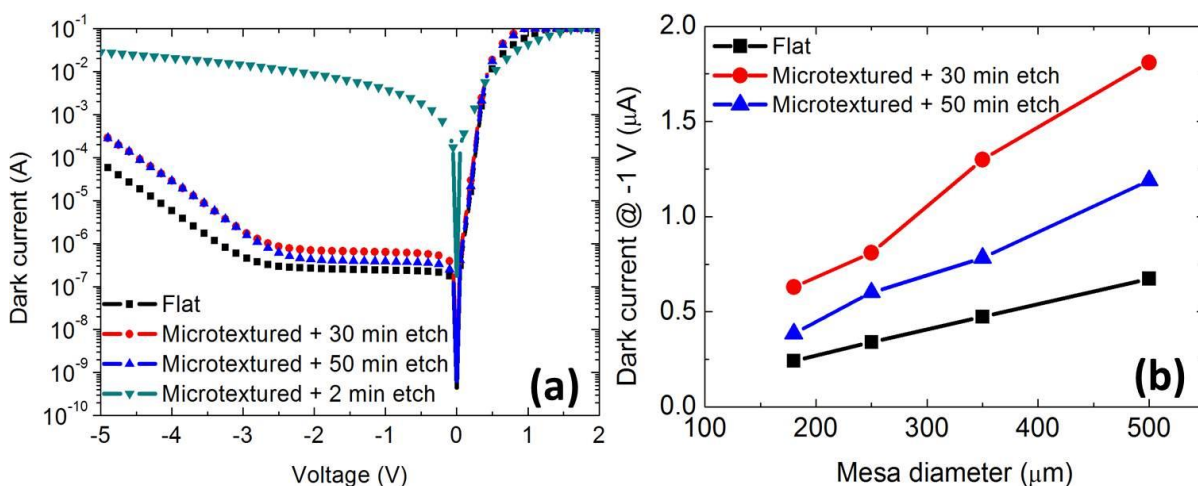


Fig. 2.12. (a) I-V characteristics of devices with flat, 30 minutes and 50 minutes post-microtexture etched surfaces. Device mesa size was  $180 \mu\text{m}$  in diameter. (b) Plots of dark current at -1 V bias as a function of mesa diameter.

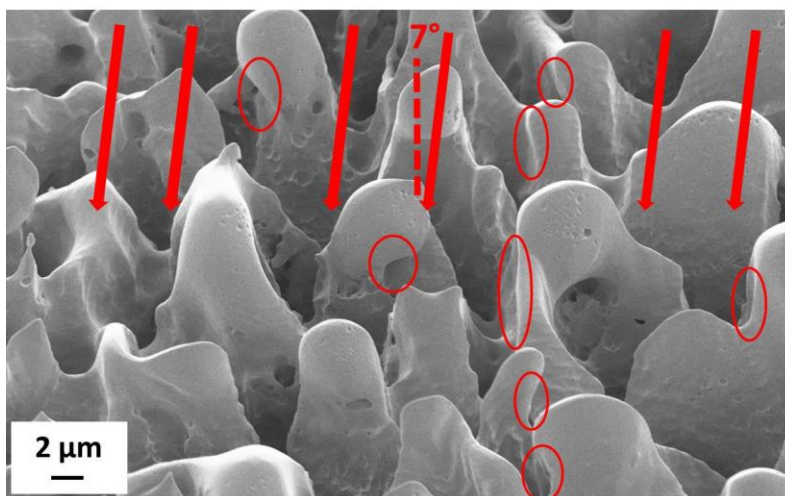


Fig. 2.13. Schematic shows the shadowing effect during ion implantation. The red arrow indicates the incoming ions. The red circles indicate the possible regions which are shaded from incoming ions. Those areas are also likely to have insufficient capping layers.

The temperature-dependence of dark current was measured to investigate the carrier transport mechanism. The results are shown in Fig. 2.14. For the three devices, the activation energies at -1 V were approximately half of the band gap of Ge. This indicates that the dark current is dominated by the Shockley-Read-Hall recombination-generation mechanism at low reverse bias. At higher reverse bias region, the rapid increase of the dark current is probably due to the end-of-range (EOR) defects generated by ion-implantation [34]. Since the temperature to crystallize the amorphous Ge is lower than the temperature to cure these EOR defects, these defects could still exist after the thermal annealing. With the presence of these defects, trap-assisted tunneling could dominate if these defects are included into the depletion region at higher reverse bias [35]. These EOR defects can be reduced by annealing at higher temperatures.

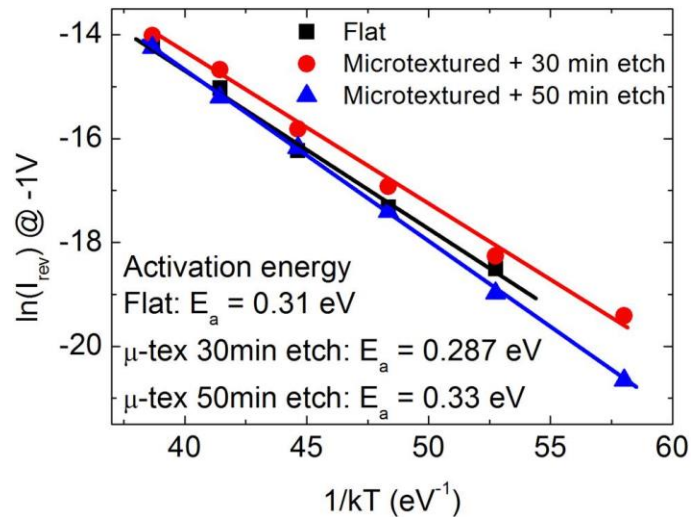


Fig. 2.14. Calculation of activation energy from the dark current at -1 V at various temperatures.

The EQE at -1 V bias was measured and the results are shown in Fig. 2.15. Overall, the EQE is higher for microtextured device than for the flat device over a broad spectrum. The EQE of the microtextured device is much higher than that of the flat device in the visible region. The higher EQE is not because of the low reflection since it is similar for the three devices. One possible reason is the role of EOR defects as explained below. If the light is absorbed deeper than the EOR defects region, fewer photo-generated carriers contribute to the photocurrent since recombination occurs when they reach the EOR defect region. The photons are absorbed in a shallower region for the microtextured device than the flat device due to refraction in Ge when the light enters the microtextured surface. In microtextured device, more photons are absorbed before they reach the EOR defects region. This generates higher photocurrent and thus the higher EQE. The EQE of the flat device approaches to the microtextured device at around 1500 nm. After 1500 nm, the EQE of the microtextured device is only a little higher than that for the flat. With better ARC layer, better starting Ge wafer and lower residual defects after thermal annealing, the EQE can be further improved.

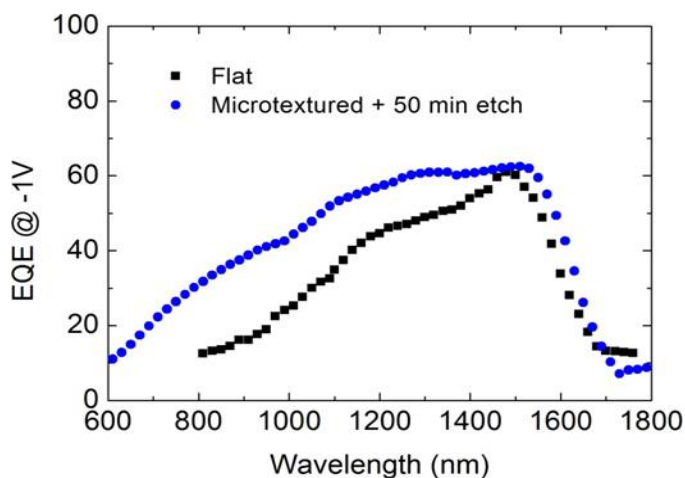


Fig. 2.15. EQE at -1 V bias for the flat and microtextured device.

The results of junction capacitance as a function for reverse bias voltage of the flat and microtextured devices are shown in Fig. 2.16. The junction capacitance decreases with reverse bias voltage due to the widening of depletion region. The flat device has the smallest junction capacitance while the device that underwent 30 minutes etch has the largest. The junction capacitance approximately follows the surface morphology [36]. The largest surface roughness of the device undergone 30 minutes etch which corresponds to the largest junction area and thus the higher junction capacitance while the smallest junction area of flat device corresponds to the smallest junction capacitance.

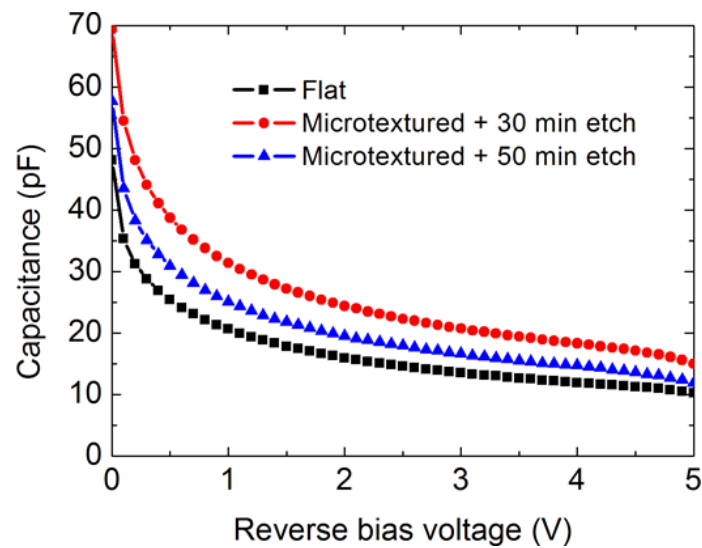


Fig. 2.16. Junction capacitance of 180  $\mu\text{m}$  mesa device as a function of reverse bias voltage.

The speed of the device was measured by temporal response to a 1.55  $\mu\text{m}$  wavelength picosecond laser pulse under -1 V bias. The transient response is shown in Fig. 2.17 (a). The full

width at half-maximum (FWHM) of the flat and microtextured device undergone 30 and 50 minutes etch are approximately 1.5 ns, 2 ns and 3 ns, respectively. The speed of the devices exactly follows the trend of junction capacitance. The -3 dB bandwidth was determined by Fourier transform of the temporal response of the photodetector and the result is shown in Fig. 2.17 (b). The -3 dB bandwidth was determined to be around 100 MHz for the three devices. At 1.55  $\mu\text{m}$  illumination, the carriers are generated deep inside the substrate and thus the speed of the device is limited by the slow diffusion in the quasi-neutral region.

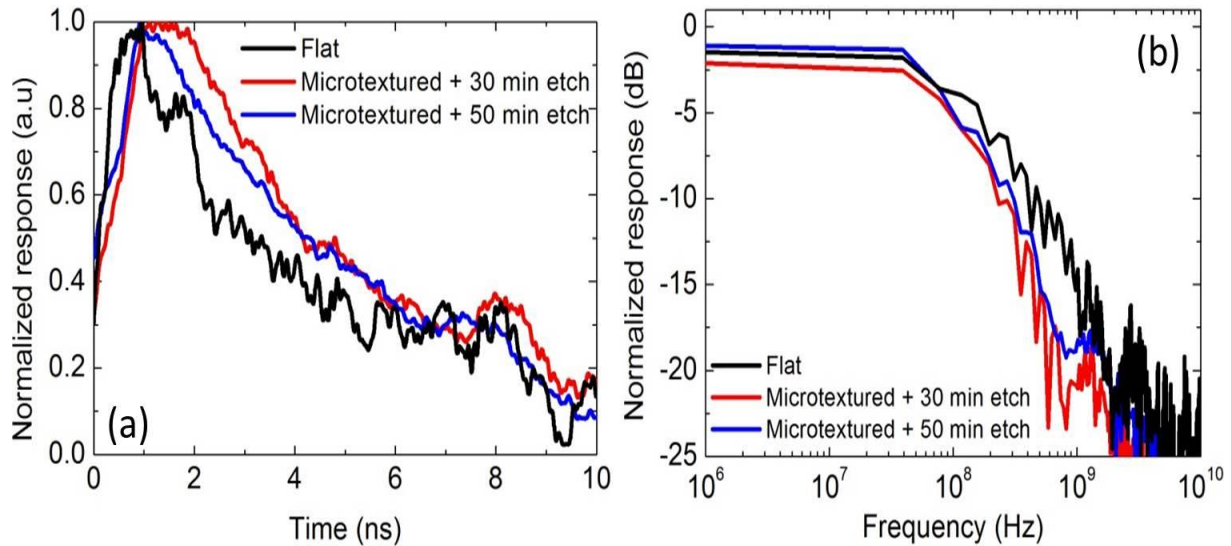


Fig. 2.17. (a) Transient response to the 1550 nm wavelength picosecond laser pulse under -1 V bias. (b) -3 dB bandwidth determined by Fast Fourier transform of the transient response. Mesa size is 180  $\mu\text{m}$  in diameter.

## 2.4 Summary

The Ge surface has been successfully microtextured by pulsed laser processing. Cone-like structures of a few micrometers both in height and in spacing can be created. The as-microtextured surface had a surface reflection of lower than 5% over a broad wavelength. The effect of chemical etch to remove the laser-induced damage in order to improve the crystalline quality was studied by XRD. The anisotropic chemical etch was proven to be effective in removing the defects. The crystalline quality became better as the chemical etching time increased. With a combination of laser-microtexture structures and ARC, the surface reflection can be very low. For the first time, Ge p-n junction photodetectors with laser-microtextured surface were fabricated and characterized. The device on surface that underwent 2 minutes post-microtexture etch suffered small shunt resistance and high dark current possibly because of the shadowing effect during ion implantation and dopant out-diffusion due to insufficient capping layer on steep edges. Comparing to flat devices, chemically post-etched microtextured devices have similar low dark current values and -3 dB bandwidth. The dark current is dominated by generation-recombination mechanism. The EQE of microtextured devices was about 15% higher than that of the flat devices over a broad wavelength. Laser microtexturing was shown to be an effective and low-cost way of reducing the optical reflection over broad wavelength and angular range and enhancing the performance of Ge photodetectors.

## **Chapter 3:**

# **Laser Doping of Ge for Microelectronic and Photonic Device Applications**

### **3.1 Introduction**

Ge has gained renewed interest recently. Due to its high carrier mobilities, Ge has potential applications in high speed electronics. Due to its low bandgap (0.66 eV), Ge also has many applications in optoelectronic devices in the near IR range. Much work has been done to realize Ge-based devices such as MOSFETs [4, 5] and photodetectors [7-10, 37]. Since the p-n junction is the basic building block of semiconductor devices, the formation of high-quality p-n junctions is crucial for high performance semiconductor devices. The conventional methods of p-n junction formation include ion-implantation [38], gas-phase doping [9, 39] and thermal diffusion from solid dopant source [40]. Each of the methods has its own drawbacks. After the ion-implantation process, the crystal defects caused by the violent bombardment of ions need to be thermally annealed. The high dark current caused by residual defects after thermal annealing is detrimental for either electronic or optoelectronic device applications. In order to reduce the dark current, high thermal budget is needed to reduce the defect density to minimum levels. However, the junction is deepened during the thermal annealing process especially at high thermal budget due to the fast diffusion of n-type dopant species. Thus, a trade-off exists between the defect annihilation by thermal annealing and the need for shallow junctions. Out-

diffusion of dopants during thermal annealing is also a challenge [41], which can cause undesirable reduction of the activated dopant concentration and thus the lowering of the conductivity of doped region. Formation of junction from solid dopant source such as spin-on-dopant (SOD) on Ge through thermal diffusion has been investigated [42]. However, surface desorption during thermal treatment due to reaction between Ge and oxygen was also reported in the literature [43]. The reported mechanism is based on the thermal decomposition of  $\text{GeO}_2$  at the interface between Ge and  $\text{GeO}_2$ , which produces volatile GeO [44]. At the same time, the oxygen in the environment reacts with Ge to replenish the  $\text{GeO}_2$  for the decomposition reaction, which causes further surface desorption. A competition exists between dopant in-diffusion and substrate loss due to the surface desorption. In our experiments, severe surface damage was observed whenever either the SOD containing a high concentration of phosphorus was used or the thermal diffusion was done at a high temperature for a long time under low vacuum condition. Ge substrate loss caused by the reaction between oxygen and Ge during thermal treatment was speculated to be the reason. One example of the damaged surface is shown in Fig. 3.1. It seems that gas-phase doping is well suited for Ge junction formation. But conventional facilities for Si gas-phase doping cannot be directly applied on Ge. Since the oxidation of Si is inevitable after the decomposition of  $\text{POCl}_3$  gas into phosphorus oxide [45], severe substrate loss due to the oxidation of Ge could be anticipated if the same gas environment was used for the Ge junction formation. Different chemical mechanism and careful design of the system are required for the system to avoid the oxidation. Metal-organic vapor phase epitaxy (MOVPE) has been used for gas-phase doping of Ge [39]. Like ion-implantation and thermal diffusion, high cost instruments and maintenance is required for gas-phase doping due to the sophisticated gas flow control system and toxic and flammable gas sources such as tertiarybutylarsine (TBAs) and hydrogen.

To overcome the difficulties associated with dopant out-diffusion and Ge substrate loss due to the thermal process and improvements in the thermal budget as well as to achieve direct selective doping, a laser doping process was investigated. Junction formation by laser doping has been widely investigated for Si solar cells [46, 47]. Laser provides a doping method with low cost system, low thermal budget and capability of selective doping without masking. Furthermore, laser treatment induces a localized heating above melting temperature within a very short time period on the order of microseconds for each laser pulse hitting on the surface. This short heating period can minimize the reaction between Ge and oxygen and thus the Ge substrate loss and at the same time induce enough dopant diffusion. Also, the full wafer is not heated as laser only heats the surface, which avoids the degradation of the bulk material. So laser doping is a very attractive process for the formation of Ge junction. In this work, laser doping of Ge was investigated and photodetector was fabricated on Ge  $n^+$ -p junction formed by laser doping and its performance was characterized.

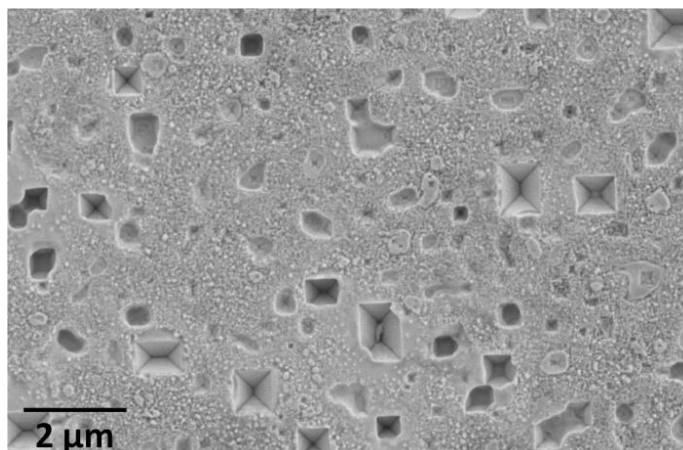


Fig. 3.1. SEM image of morphology of the Ge surface after thermal diffusion with high concentration SOD (P509) at 580 °C for 4 minutes.

### 3.2 Ge n<sup>+</sup>-p junction formation and photodiode fabrication

A p-type Ge wafer (MTI Inc., 2 ~ 4 ohm cm, 500  $\mu\text{m}$  thickness) was used in the experiment. The wafer was cleaned subsequently in  $\text{NH}_4\text{OH} : \text{H}_2\text{O}_2$ ,  $\text{HCl} : \text{H}_2\text{O}_2$  and diluted HF. Residual moisture was evaporated by a soft bake at 130  $^\circ\text{C}$  for 5 minutes. About 160 nm of SOD (Filmtronics, P507) was applied by spin coating. The coated sample was baked at 200  $^\circ\text{C}$  for 15 minutes to evaporate the solvents in SOD. The sample was then placed on a computer-controlled X-Y translational stage for laser scanning. A 1064 nm wavelength pulsed fiber laser (IPG laser, YLP-RA series) was used to irradiate the sample at a repetition rate of 30 kHz. The laser beam was focused to a 100  $\mu\text{m}$  spot and the scanning speed was kept at 10 mm/s. The laser energy density was chosen from 0.85  $\text{J}/\text{cm}^2$  to 2.65  $\text{J}/\text{cm}^2$  for doping. A 30% overlapping of the laser scan lines was used to ensure the uniformity of the doping. After the doping, the SOD was removed in dilute HF.

The mesa structure was formed by reactive ion etching. The etch conditions are listed as follows: a  $\text{O}_2$  flow rate of 5 sccm, a  $\text{SF}_6$  flow rate of 20 sccm, a RIE power of 120 W, an ICP power of 200 W, and a pressure of 10 mTorr. The etching was done at room temperature for 6 minutes to form a mesa of about 3  $\mu\text{m}$  height. A 100 nm  $\text{SiO}_2$  layer was then deposited by PECVD as an anti-reflection coating. The contacts were patterned by photolithography and a stack of Ti/Au (25 nm/ 120 nm) was deposited by e-beam evaporation for both the p- and n-type contacts. The contacts were thickened to about 3  $\mu\text{m}$  by electroplating of Au.

### 3.3 Results and discussion

The surface morphology after laser doping was examined using SEM and the results are shown in Fig. 3.2. At low laser power density of  $0.85 \text{ J/cm}^2$ , which is close to the Ge melting threshold, the surface was still smooth. At medium laser power density of  $1.7 \text{ J/cm}^2$ , the surface showed wave-like morphology resulted from the melting and re-solidification. At high laser power density of  $2.65 \text{ J/cm}^2$ , the wavy structures became more obvious and surface turned rougher. With the increasing laser power, the change of the surface morphology became more significant. The sheet resistance was measured using four-point probe and the results are shown in Table 3.1. The sheet resistance of n-type doped region could be varied from  $6.75 \text{ ohm/sq}$  to  $90 \text{ ohm/sq}$  when the laser power density ranged from  $2.65 \text{ J/cm}^2$  to  $0.85 \text{ J/cm}^2$ .

The phosphorus doping profile result obtained by SIMS measurements is shown in Fig. 3.3. The peak concentration was  $1.2 \times 10^{19} \text{ atoms/cm}^3$  and the junction depth was  $850 \text{ nm}$ . Typically, thermally diffused junction from SOD source provides a box-like doping profile with a surface concentration of  $2 \times 10^{19} \text{ atoms/cm}^3$  [38, 48]. At temperature of  $580 \text{ }^\circ\text{C}$ , the junction depth formed by thermal diffusion using SOD can range from  $250 \text{ nm}$  for an effective diffusion time of  $3.5 \text{ minutes}$  to  $550 \text{ nm}$  for  $10 \text{ minutes}$  [40]. Unlike the box-like dopant profile in junction formed by thermal diffusion, the junction formed by laser doping has a Gaussian profile.

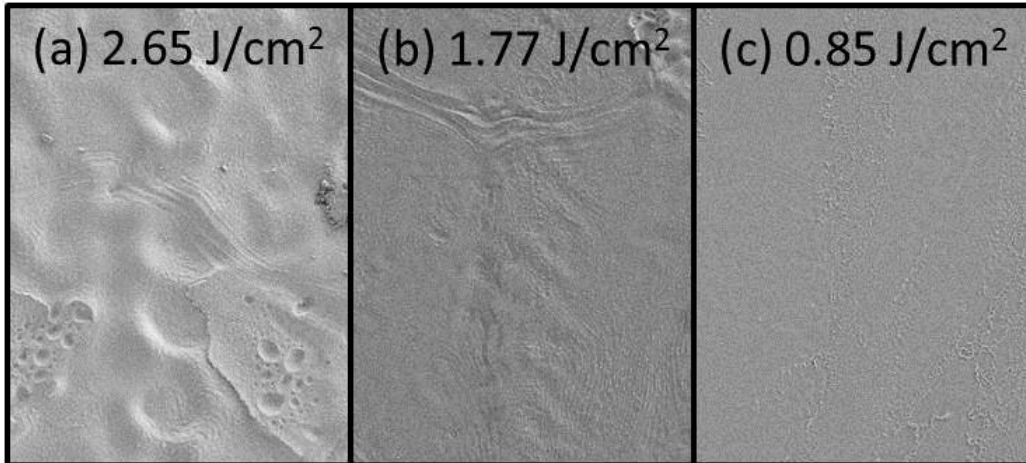


Fig. 3.2. SEM images of Ge surface morphology after laser doping at laser energy density of (a)  $2.65 \text{ J/cm}^2$  (b)  $1.77 \text{ J/cm}^2$  and (c)  $0.85 \text{ J/cm}^2$ .

Table 3.1. Sheet resistance values at different laser power density.

Laser power density ( $\text{J/cm}^2$ )	Sheet resistance (ohm/sq)
2.65	6.75
2.21	15.3
1.77	44.1
1.33	47.25
0.85	90

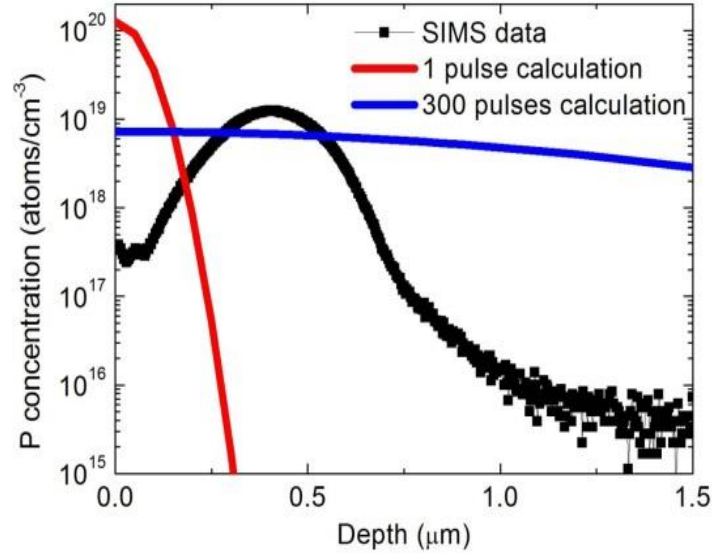


Fig. 3.3. Phosphorus doping profile obtained by SIMS measurements and qualitative calculation. The carrier concentration of the p-type Ge substrate was  $5 \times 10^{16}$  atoms/cm<sup>3</sup>. The junction depth was 850 nm.

A simple qualitative calculation can show physical mechanism about the laser doping process. As shown in Fig. 3.3, the dopant profile for one laser pulse was calculated. The dose was chosen to approximately match the SIMS profile and the latent heat of phase change was ignored here. The effective time period during which Ge is molten was assumed to be 50 ns for each laser pulse of 50 ns duration. A diffusivity of  $4 \times 10^{-4}$  cm<sup>2</sup>/s was used in the calculation for phosphorus atoms diffusion in liquid Ge [49]. The calculation for dopant profile after 300 laser shots was done in the same way assuming the effective melting time was simply 300 times of 50 ns since each spot on the wafer was irradiated by 300 laser pulses. Usually upon the first or the second laser pulse at this laser fluence, Ge is melted and the generated heat ablates part of the SOD film. The phosphorus atoms in SOD are captured by the molten Ge and embedded in a shallow region near the surface. As can be seen from the calculation, after the first pulse

phosphorus atoms are incorporated into a shallow region and the junction depth is about 250 nm. The subsequent laser pulses further drive the existent phosphorus deeper into the substrate. According to the calculation for the dopant profile after 300 laser pulses, the junction should be much deeper than the SIMS results. The difference is due to the wrong assumption that all the diffusion happens in liquid phase Ge. The absorption depth of Ge at 1064 nm wavelength is about 900 nm [50], little melting is expected beyond this depth. The diffusion in solid Ge during each short laser pulse can be neglected due to the short diffusion time and much lower diffusivity in solid phase than in liquid phase. Also at 30 kHz laser repetition rate, no significant accumulation of heat is expected between pulses. Thus phosphorus diffusion is limited to about 900 nm in thickness as indicated in SIMS data. Hence the real junction depth is much shallower than the calculation. In other words, laser is only effective for driving dopant atoms down to certain depth for a certain laser fluence. Beyond that depth, the heat is not enough to drive them further. The difference is also caused by the movement of the solid-liquid interface. Upon the laser irradiation, a molten pool was created in Ge substrate. The solid-liquid interface moves from surface towards the deeper region. After the laser pulse ceases, the interface returns from deeper region towards the surface. Thus the amount of time during which Ge is in liquid phase is less for the deeper region than for the upper shallow region. Hence the dopant atoms will diffuse more in shallow region than in deeper region. This causes a sharp drop in the dopant profile in SIMS results. The exact dopant profile could be acquired by solving thermal diffusion equation with moving boundary condition taking into account the phase change during laser treatment [49]. The low surface concentration in the SIMS result is probably caused by the out-diffusion of the dopant atoms during laser irradiation since laser pulses ablated the SOD film and hence there was no capping layer on the surface to prevent the out-diffusion.

Figure 3.4 (a) shows the dark current (I) - bias voltage (V) characteristics of the Ge  $n^+$ -p diode formed by laser doping with mesa diameters ranging from 180 to 500  $\mu\text{m}$ . For comparison, the dark I-V data for the  $n^+$ -p diode formed by rapid thermal diffusion with a mesa diameter of 180  $\mu\text{m}$  is also shown in Fig. 3.4 (a). The thermally diffused  $n^+$ -p junction was formed by applying SOD and subsequent diffusion in a rapid thermal annealing system for 130 s at 580  $^\circ\text{C}$ . An ideality factor of 1.34 was calculated for the laser-doped diode in the forward bias region. The roll off at high bias voltage is due to the effect of series resistance caused by low surface doping level. The calculated ideality factor of thermally diffused diode was reported as 1.03 [51] which indicates a diffusion-dominated current with low defect density. The ideality factor for the ion-implanted diodes was reported as 1.45, showing a high recombination-dominated current related to high defect density. The higher than 1 ideality factor for laser-doped diode is due to laser-induced defects, resulting in recombination-generation current. In the forward bias region of the I-V curve for thermally diffused diode, the current is dominated by the Schottky metal contact to p and  $n^+$  regions. In the reverse biased region, it can be seen that the laser-doped devices show dark current comparable to the thermal diffused devices. However, the dark current value of 7.5  $\text{mA}/\text{cm}^2$  is much lower than reported value of 560  $\text{mA}/\text{cm}^2$  for ion implantation based device [9]. A numerical fitting of the dark current in reverse biased region is shown in Fig. 3.4 (b). Diffusion, recombination-generation and surface leakage components are included in the fitting. The surface leakage component is also included using the value calculated from Fig. 3.5. For the generation-recombination components, the defect level is assumed to be located in mid-bandgap according to the result of temperature dependence of dark current shown in Fig. 3.6. The fitting gives an effective carrier lifetime of 2.6  $\mu\text{s}$  for laser-doped junction region and 20  $\mu\text{s}$

for thermally-diffused junction in the depletion region. This further shows the existence of laser-induced defects which lowers the effective lifetime of the laser-doped junction.

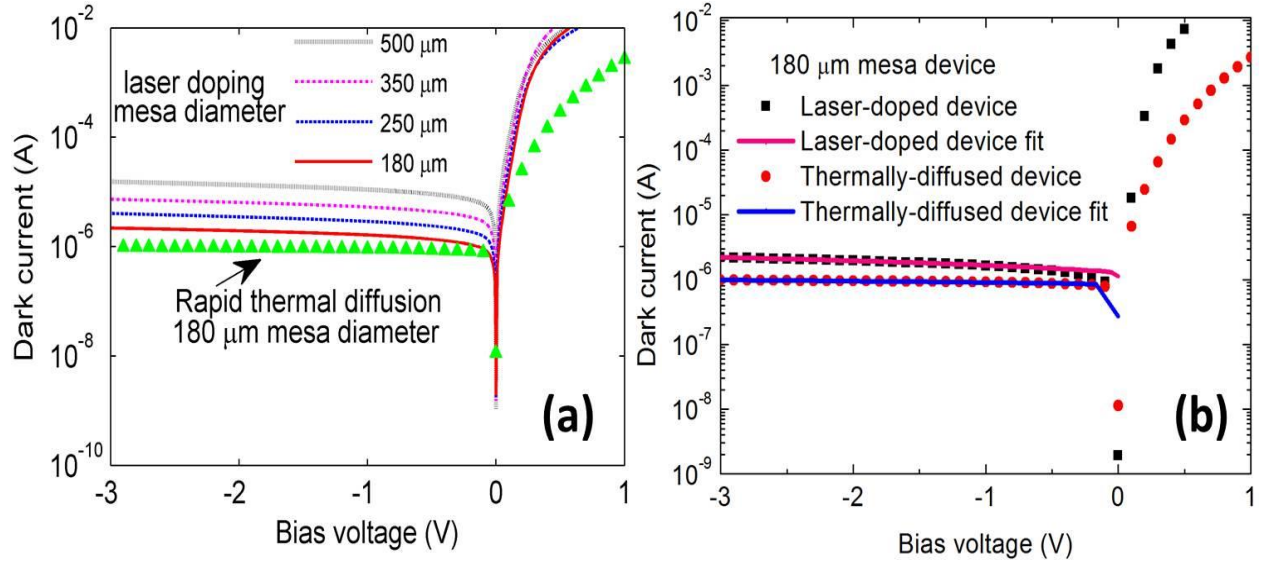


Fig. 3.4. (a) I-V characteristics of  $n^+$ -p junctions formed by laser-doping and rapid thermal diffusion process. (b) Numerical fitting of  $n^+$ -p junctions of 180 μm mesa diameter formed by laser-doping and rapid thermal diffusion process.

To explicitly compare the measured results with the reported results, the dark current density of devices of different mesa sizes was investigated and the results are shown in Fig. 3.5.

The total dark current  $I_{dark}$  is made of bulk and surface components

$$I_{dark} = J_{bulk} \cdot \pi \cdot r^2 + J_{surf} \cdot 2\pi \cdot r$$

where  $r$  is the mesa radius,  $J_{surf}$  is surface leakage current density and  $J_{bulk}$  is bulk leakage current density. The  $J_{bulk}$  was found to be 5.4 mA/cm<sup>2</sup> and  $J_{surf}$  was 2.0 μA/cm. Our surface leakage current component is comparable to the value of 8.4 μA/cm reported by Takenaka's group using SiO<sub>2</sub> surface passivation [9]. Takenaka's group has shown that by using GeO<sub>2</sub>

surface passivation layer, the surface leakage can be further reduced by a factor of 30 and bulk leakage current density was reported as  $0.032 \text{ mA/cm}^2$ . In our laser-doped device, the surface leakage can be expected to be reduced further with  $\text{GeO}_2$  passivation layer. However, the bulk leakage in laser-doped device is still higher, possibly due to the laser-induced defects which can be further reduced through thermal annealing process.

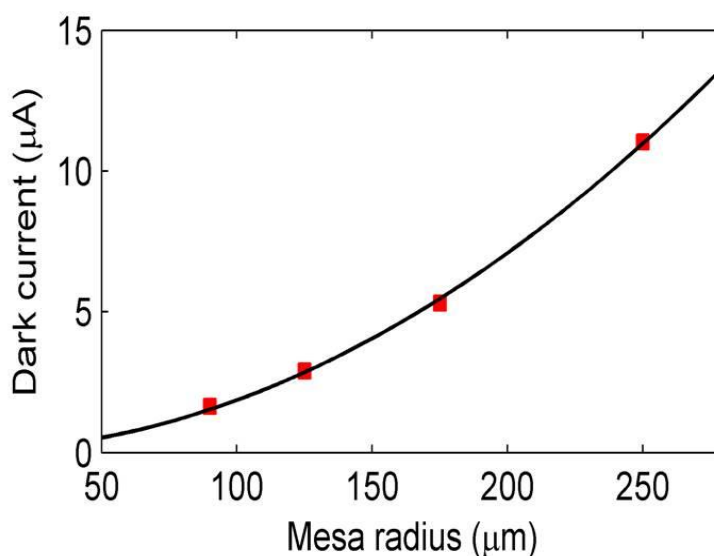


Fig. 3.5. Dark current as a function of the mesa radius for the  $\text{SiO}_2$ -passivated Ge photodetectors with laser-doped junctions.

The temperature dependence of the dark current was carried out to investigate the carrier conduction mechanism [52]. The results are shown in Fig. 3.6. The activation energy was calculated to be  $0.35 \text{ eV}$  at  $-1 \text{ V}$  reverse bias, which corresponds to half of the band gap of Ge. This result indicates that the Shockley-Read-Hall recombination-generation is the dominating mechanism for the dark current.

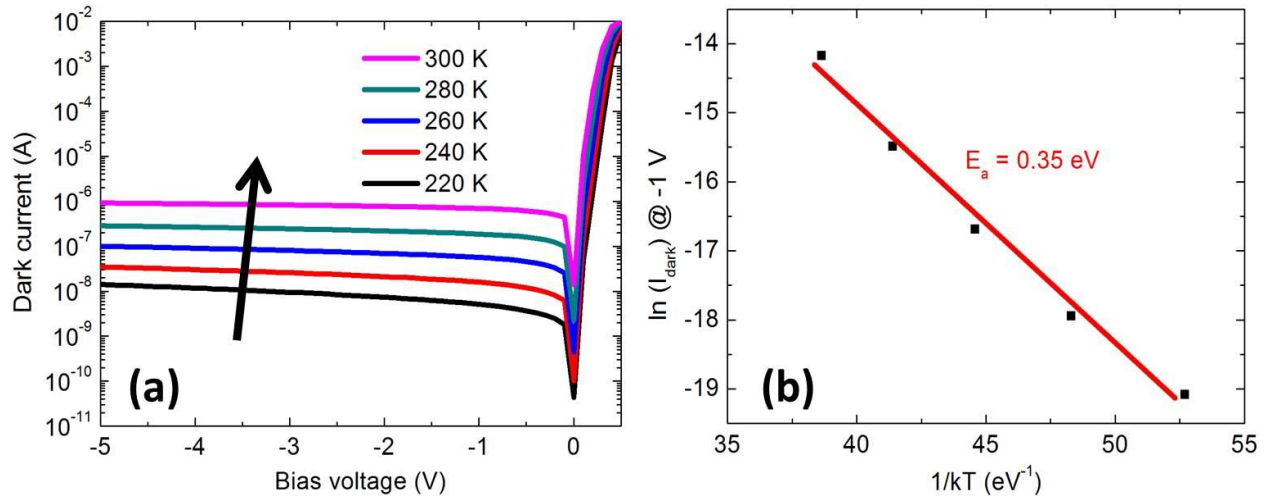


Fig. 3.6. (a) Dark current at different temperature. The arrow indicates the varying temperature from 220 K to 300 K in step of 20 K. (b) Activation energy of dark current at -1 V bias for Ge  $n^+$ -p junction mesa device formed by laser-doping.

To show the applicability of the laser-doped p-n junctions in photodetector applications, I-V characteristics were measured under light illumination. A  $1.55 \mu\text{m}$  laser beam was coupled into an optical fiber to illuminate the device. The I-V results under light illumination power of  $45 \mu\text{W}$  are shown in Fig. 3.7. The variation of dark current with bias voltage is also shown in the Fig. 3.7 as a reference. A photo-response can be seen from the I-V curve under illumination. The responsivity was calculated to be  $0.46 \text{ A/W}$  at 0 V bias. Although this value is lower than the values of  $0.55 \text{ A/W}$  in the literature [9], this can be further improved by optimization of the junction depth and post-doping annealing to remove the laser-induced defects.

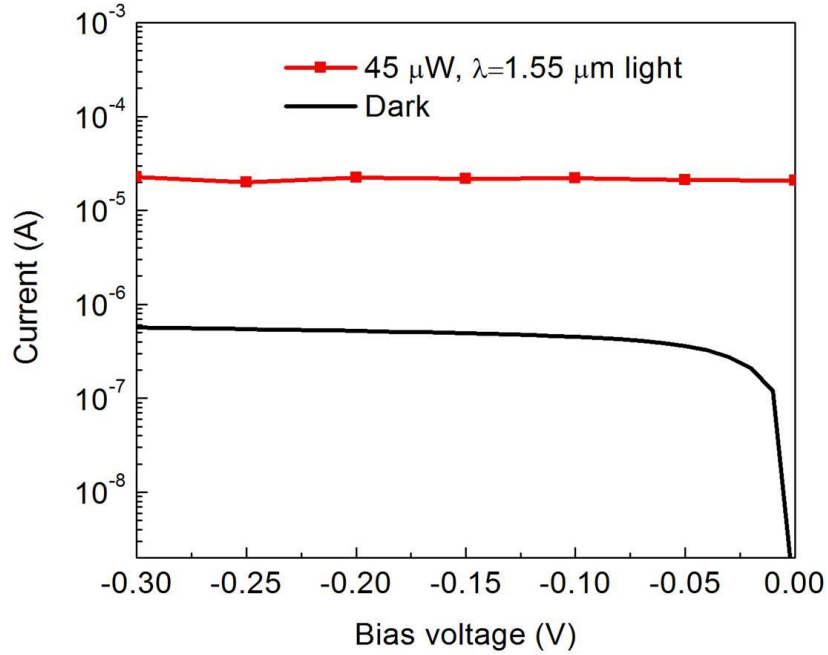


Fig. 3.7. I-V characteristics of Ge photodetector with laser-doped junction under dark and 1.55  $\mu\text{m}$  wavelength light illumination.

The speed of the device was measured by the transient response of the device to a 1.55  $\mu\text{m}$  wavelength picosecond laser pulse under 0 V bias. The transient response is shown in Fig. 3.8 (a). As a comparison, the speed of the thermally diffused device is also shown in the figure. The full width at half-maximum (FWHM) was about 2 ns for the laser doped device and 1ns for the thermally diffused device. The -3 dB bandwidth was calculated by Fourier transform of the temporal response and the results are shown in Fig. 3.8 (b). The bandwidth was determined to be 190 MHz for the laser-doped device which is slightly smaller than the bandwidth of 230 MHz for thermally diffused device.

At 1.55  $\mu\text{m}$  wavelength illumination, the carriers are generated deep inside the device. The temporal response is limited by slow carrier diffusion. The high responsivity and good bandwidth under 0 V bias operation suggest the applicability for low power imaging systems.

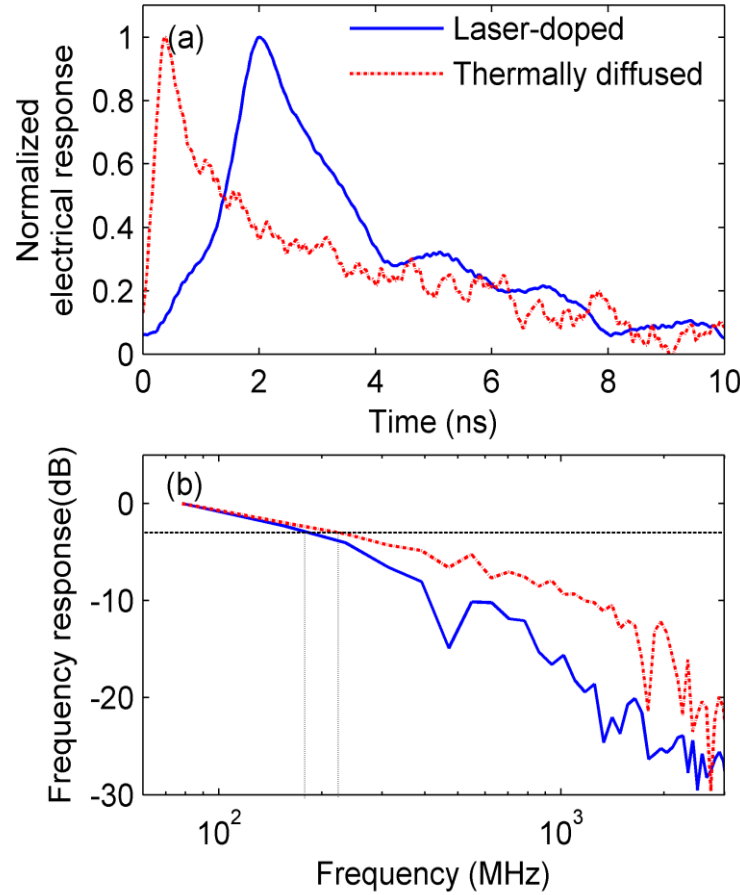


Fig. 3.8. (a) Transient response of the Ge photodetector of 130  $\mu\text{m}$  mesa diameter to a 1.55  $\mu\text{m}$  wavelength picosecond laser pulse under 0 V bias condition, and (b) Fourier transform of the transient response. Dash line is for thermally diffused device and solid line is for laser-doped device.

### 3.4 Summary

A  $n^+$ -p junction formation in Ge using laser doping process has been successfully demonstrated. The physical mechanism of laser doping is discussed. The dopant atoms have a Gaussian profile as a result of the multi-pulse laser treatment. An  $n^+$ -p junction device was fabricated. The junction had a low bulk leakage current density of 5.4  $\text{mA}/\text{cm}^2$  and a surface leakage current density of 2.0  $\mu\text{A}/\text{cm}$ . The major part of dark current is coming from the laser-

induced defects in the bulk Ge material. The temperature-dependent dark current measurement showed that the main mechanism of the dark current is dominated by the carrier generation-recombination in the depletion region. To show the application in optoelectronic devices, the photo-responsivity of the laser-doped device was measured to be 0.46 A/W at 1.55  $\mu\text{m}$  wavelength at 0 V bias. The 130- $\mu\text{m}$ -diameter device had a -3 dB bandwidth of 190 MHz. It is demonstrated that laser doping is an effective method for forming Ge p-n junctions for photonic and microelectronic device applications.

## Chapter 4:

# Sulfur-Hyperdoping of Germanium by Pulsed Laser

### 4.1 Introduction

Deep level impurities could be introduced into semiconductors to produce intermediate band (IB), which could be useful for high performance optoelectronic or photovoltaic devices. IB formed by deep level dopants of chalcogen [53-55] and Ti [56] in Si has been extensively investigated. Chalcogen-hyperdoped Si shows strong sub-bandgap optical absorption due to the IB formed by the deep level chalcogen atoms in the bandgap of Si [15, 57]. Moreover, rectifying junctions can be formed by the chalcogen-doped Si [58, 59]. The chalcogen atoms act as n-type deep level donors which provide electrons to the conduction band of Si [53]. Photodiodes based on chalcogen-doped Si were realized [59, 60]. In order to form rectifying junctions using chalcogen as donors, the chalcogen atoms should be incorporated into Si to a supersaturated concentration. Typically the required concentration is several orders of magnitude higher than the solid solubility limit [61]. Such supersaturated concentration cannot be achieved by conventional doping methods. In order to achieve such high concentration, the melt solidification speed should be much higher than the diffusive speed of the solute to cause significant solute trapping [62]. Thus, ultrafast thermal process is necessary to achieve this deviation from equilibrium condition. The supersaturated concentration of chalcogen in Si can be achieved either by femtosecond laser irradiation of Si in SF<sub>6</sub> environment [63] or by ion implantation followed by pulsed laser melting [64].

Ge belongs to the same group as Si in the periodic table and recently has been receiving renewed interest both for microelectronic and photonic applications. A significant amount of work has been devoted to realize high speed MOSFETs [65] and photodetectors [9, 10]. Compared to devices based on III-V semiconductors, devices based-on Ge have lower cost due to the material itself and compatible fabrication process with Si [11, 12, 24, 66]. As reported in the literature, photodiodes fabricated on chalcogen-hyperdoped Si had external quantum efficiency (EQE) much higher than unity [16]. Whether chalcogen atoms can be incorporated into Ge to improve the device performance remains a question and needs to be investigated. Although there are reports in the literature on individual chalcogen impurity levels in Ge [67], to the best of our knowledge, no literature exists for chalcogen doping of Ge to supersaturated concentration. Photodiodes based on chalcogen-hyperdoped Ge material have never been reported either. In this work, sulfur (S) was successfully incorporated into Ge to high concentration levels by short pulsed laser doping in SF<sub>6</sub> environment. Photodiode based on S-hyperdoped Ge was realized and characterized for the first time. In most wavelength region, EQE is close to 100%, which indicates internal quantum efficiency (IQE) higher than unity. The -3 dB bandwidth of the device was measured to be about 20 MHz. S-hyperdoping is demonstrated to be an effective way to improve the Ge device performance.

## **4.2 Experimental**

### **4.2.1 S doping**

Various types of Ge wafers were used: 1) p-type, 0.23 ~ 0.24 Ω·cm; 2) p-type, 10 ~ 15 Ω·cm; 3) p-type, 0.06 Ω·cm; 4) undoped. Chemical cleaning of the wafer was done sequentially

in  $\text{NH}_4\text{OH} : \text{H}_2\text{O}_2$ ,  $\text{HCl} : \text{H}_2\text{O}_2$  and diluted HF. The cleaned sample was placed in a vacuum chamber, which was filled with  $\text{SF}_6$  gas to a pressure of 500 mbar. A 532 nm pulsed fiber laser (IPG GLP-10, 1 ns pulse width) was used to irradiate the 0.06  $\Omega\text{-cm}$  p-type wafer. The laser beam was focused to a spot with an energy density of approximately  $2.1 \text{ J/cm}^2$  and scanned across the wafer by means of a galvanometer. Every spot on the wafer received about 200 laser pulses. A 1064 nm wavelength, pulsed fiber laser (IPG Photonics, YLP-RA series, 50 ns pulse width) was used to irradiate the other types of Ge wafers at a repetition rate of 30 kHz. The laser beam was focused down to a 100  $\mu\text{m}$  spot and a fluence of  $2 \text{ J/cm}^2$ ,  $2.3 \text{ J/cm}^2$  and  $2.6 \text{ J/cm}^2$  was used to irradiate the samples. The beam was scanned across the sample also by means of a galvanometer and every spot on the sample received about 300 laser pulses. After the doping, the sample was rinsed with diluted HF to remove any oxide.

#### **4.2.2 Photodiode fabrication**

A 100 nm  $\text{SiO}_2$  capping layer was coated on the laser-doped sample by plasma-enhanced chemical vapor deposition (PECVD). The sample was annealed at different temperatures for 2 minutes in vacuum using RTA system to activate the S dopants. The mesa structures was patterned by photolithography and formed by inductively coupled plasma etch. The etch conditions were: a  $\text{O}_2$  flow rate of 5 sccm, a  $\text{SF}_6$  flow rate of 20 sccm, and an RIE power of 120 W, an ICP power of 200 W, and a pressure of 10 mTorr. After the dry etching, the initial  $\text{SiO}_2$  capping layer was removed in diluted HF and a fresh ARC of 100 nm  $\text{SiO}_2$  was deposited by PECVD. The metal contacts were patterned by photolithography. A stack of Ti/Au (25 nm/ 120

nm) contacts were deposited by electron beam evaporation. Finally the metal contacts were thickened to about 3  $\mu\text{m}$  by Au electroplating.

## 4.3 Results and Discussion

### 4.3.1 Results of device hyperdoped using 532 nm wavelength nanosecond pulsed laser

The dark current (I) – voltage (V) characteristics of the device hyperdoped using 532 nm nanosecond laser are shown in Fig. 4.1 (a). Although some rectifying behavior is observed in the figure, the device suffered from a severe shunt problem as shown in the reverse bias region. The possible reasons for this shunt problem are explained below. The SEM image of the device is shown in Fig. 4.1 (b). Upon the irradiation of 532 nm nanosecond laser at a laser fluence of 2.1  $\text{J}/\text{cm}^2$ , not only the S atoms were incorporated into the sample, but the surface was also heavily microtextured. As discussed in chapter 2, the coverage of the  $\text{SiO}_2$  capping layer on microtextured surfaces was non-uniform using PECVD. The steep edge regions might not be fully covered. During the thermal activation process, out-diffusion of the S dopant atoms could occur in these uncovered areas. This was confirmed by the black material deposited on the quartz cover slide on top of the sample during the thermal activation process. The quartz cover slide is shown in Fig. 4.2. The thermal activation was done at 300  $^\circ\text{C}$  for 2 minutes. Ge material doesn't desorb at this low temperature [43]. Thus the black material was speculated to be the out-diffused S dopant atoms during the thermal activation process. However, this out-diffusion barely occurred on S-doped Ge with flat surfaces. This further indicates that the non-uniform coverage of the  $\text{SiO}_2$  capping layer should be accounted for the out-diffusion of S atoms. Furthermore, the penetration depth of Ge at 532 nm wavelength is very small ( $\sim 20$  nm) [50]. As

a result, the S atoms were embedded in a very shallow region beneath the front surface using a laser of 532 nm wavelength. This shallow doping made the out-diffusion even more severe. This point was further proved by the fact that the out-diffusion of S dopant atoms was not observed even without SiO<sub>2</sub> capping layer for the samples doped using a laser of 1064 nm wavelength at which Ge has a larger optical absorption depth. Although the microtextured surfaces have high optical absorption, the out-diffusion of S dopant atoms during thermal activation leads to the failure of the devices. Thus, if heavily microtexture surface is to be used for device fabrication, effective method for uniform capping layer deposition should be found in order to avoid the dopant out-diffusion. Also, very shallow incorporation of S is not desired since it has higher possibility of dopant out-diffusion. So for the rest of the work, only devices with relatively flat surfaces and hyperdoped using 1064 nm wavelength laser will be discussed.

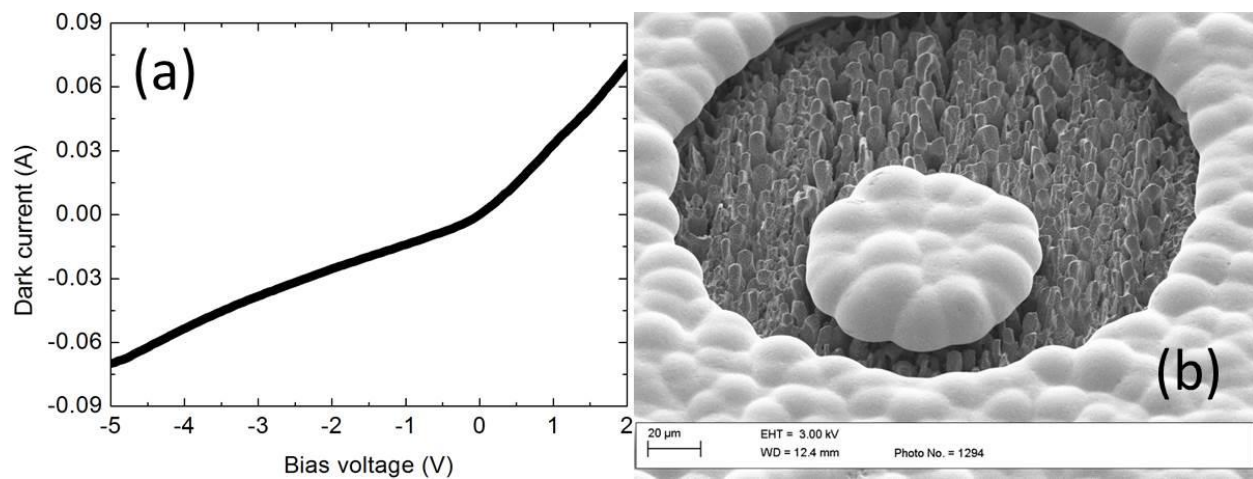


Fig. 4.1. (a) I-V characteristics of S-doped Ge photodiode using a 532 nm wavelength nanosecond pulsed laser. (b) SEM images of the mesa device.



Fig. 4.2. Black material deposited on the quartz cover slide during thermal activation at 300 °C for 2 minutes. The black material in the red circle is speculated to be out-diffused sulfur.

### 4.3.2 Sulfur doping profile

The S concentration profile in the Ge hyperdoped using 1064 nm pulsed laser was investigated by secondary ion mass spectrometry (SIMS). The S profile before and after rapid thermal annealing (RTA) are both shown in the Fig. 4.3. Both profiles show a high peak concentration of around  $10^{19} \text{ cm}^{-3}$  at the surface. The concentration decreases sharply to around  $10^{17} \text{ cm}^{-3}$  at 5 nm depth. Then a gradual exponential decrease follows the initial sharp one. The high concentration profile is confined in a very shallow region near the surface and the junction depth is less than 50 nm. The optical absorption depth for Ge at 1064 nm wavelength is around 1  $\mu\text{m}$  and Ge surface is melted under the used laser fluence irradiation conditions. Considering the

fast diffusion of dopants in liquid phase Ge, the junction should be much deeper than 100 nm. There are three possible reasons for the shallower junction than expected: photochemical etching, out-diffusion of the dopants and dopant segregation effect. First, laser-assisted chemical etching of Si in SF<sub>6</sub> environment has been reported in the literature [68]. SF<sub>6</sub> is a conventional gas source for dry etching of Ge. Similar laser-assisted photochemical etching can happen for Ge during the laser hyperdoping process. SF<sub>6</sub> possibly removed the surface layer which contained high concentration of S atoms formed by the previous laser pulses and as a result, only shallow doped region was left. Secondly, the out-diffusion of dopant atoms in Ge has also been reported in the literature [13]. Large amount of incorporated S atoms can diffuse out of the Ge surface during the hyperdoping process. So there exists a competition between the in-diffusion of S atoms in the laser-generated molten pool and the out-diffusion of S atoms. Moreover, the photochemical etching effect of SF<sub>6</sub> on Ge further decreased the doped region. As a result of these two effects, only shallow doped region was formed after the laser hyperdoping. Lastly, dopant segregation is another phenomenon which could happen during laser doping [69]. Incorporated dopant atoms tend to remain in the molten material rather than in the solid state. Consequently, the liquid-solid interface could sweep the S atoms from deeper region to the upper surface region during the solidification process after the laser pulse irradiation, which explains the high concentration of S atoms near the surface region. These three facts resulted in the shallow S dopant profile with high concentration at the surface as shown in the SIMS data. The S concentration after thermal annealing is a little lower than the concentration before thermal annealing possibly because of the in-diffusion of S atoms during the annealing process and annealing was carried out at relatively low temperature.

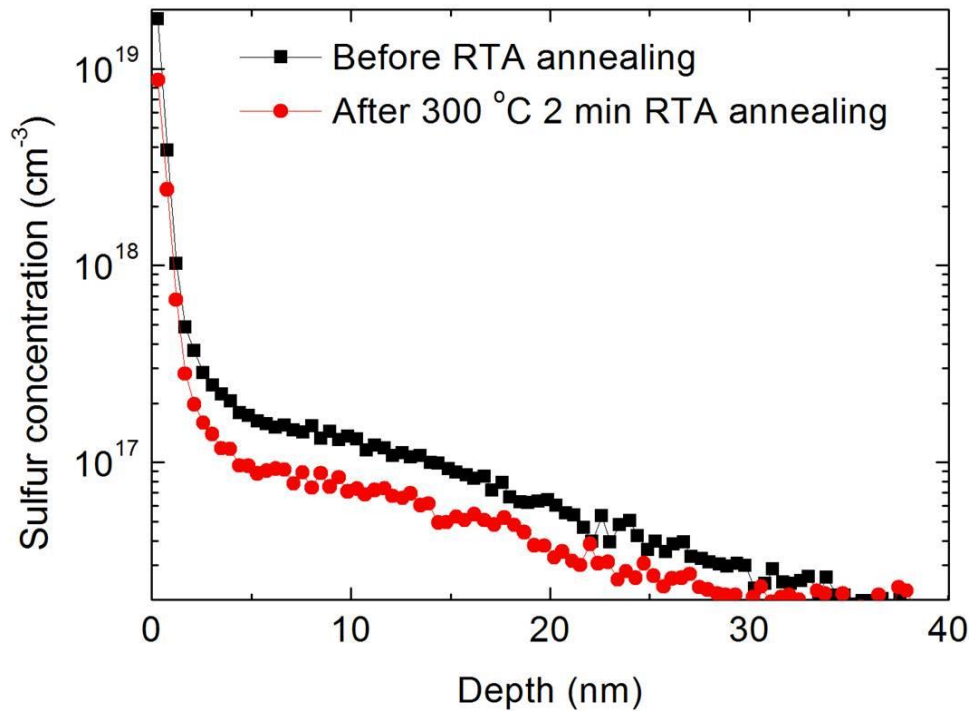


Fig. 4.3. S doping profile obtained by SIMS measurement for the laser-hyperdoped Ge sample before and after thermal annealing.

### 4.3.3 Effects of thermal activation

After the laser hyperdoping, the S atoms incorporated into Ge need to be activated by a high temperature thermal annealing process. The dark I-V characteristics of the devices that underwent no activation and 2 minute activation at 300 °C, 400 °C and 500 °C are shown in Fig. 4.4. The device with no activation showed resistor-like behavior. However, after 2 minute activation at 300 °C and 400 °C, the devices exhibited rectifying behavior. This rectifying behavior is not quite the same as the behavior of the conventional diodes. This behavior is due to the opposite serial connection of two diodes and will be explained in the next section. The rectifying behavior of the device that underwent 2 minute activation at 500 °C was greatly

reduced. The possible mechanism of the I-V behavior after different amount of activation is discussed below. After the laser hyperdoping, the S atoms were incorporated into Ge in such a way that their donor electrons did not contribute to conduction. The donor electrons might be locked up in traps. The embedded S atoms might occupy interstitial sites or they could have a coordination number larger than four. During the thermal activation, the bonding arrangements changed. The coordination number of the S atoms could be reduced to four and the S atoms might migrate to substitutional sites. Thus the electrons were freed up to the conduction band of Ge and contributed to conduction. Above 500 °C, the bonding environment of the S atoms was rearranged again to a new configuration or S atoms could form complexes so that the electrons were trapped again and did not contribute to the conduction. It was also possible that the S atoms diffused deeper into the wafer or out-diffused and the concentration is lower than the doping level of the Ge wafer. As a result, rectifying junctions were not established. The exact mechanism is still not clear and needs to be further investigated.

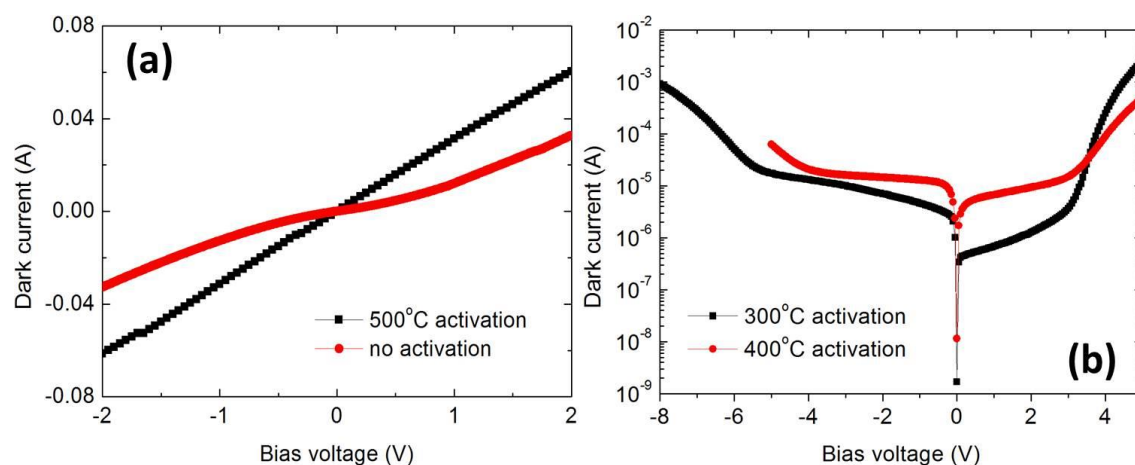


Fig. 4.4. Dark I-V characteristics of devices that underwent (a) no activation and 500 °C, (b) 300 °C and 400 °C 2 minutes activation.

#### 4.3.4 Results of devices on 10 ~ 15 $\Omega\cdot\text{cm}$ wafer hyperdoped using 1064 nm wavelength nanosecond pulsed laser

The I-V characteristics of the S-doped device on p-type 10 ~ 15  $\Omega\cdot\text{cm}$  Ge wafer after 300 °C thermal activation are shown in Fig. 4.5. The I-V characteristics of the devices hyperdoped at different laser fluence are similar. They do not show simple diode-like rectifying behavior. The circuit model is two opposite serial connected diodes as shown in Fig. 4.6. Since S atoms are believed to act as deep level donors [70], they can provide electrons into the conduction band of Ge. Thus the S-incorporated region is expected to be n-type. As a result, a diode is formed between the S-incorporated region and the p-type substrate which is represented by diode 1 in the figure. On the other hand, the Fermi level is pinned at the surface of n-type Ge. So there exists an energy barrier of around 0.57 eV for electrons at the interface between Ti contact and S-incorporated Ge region [71]. Hence a Schottky diode is formed by the Ti contact and S-incorporated region which is represented by diode 2 in the figure. It is the opposite series connection of these two diodes which results in the I-V characteristics of the device shown in Fig. 4.6. In the reverse-bias region (region 1 in Fig. 4.6), since diode 2 is forward-biased while diode 1 is reverse-biased, the current is limited by diode 1. Thus the current in region 1 represents the reverse-bias current of the diode 1, which is the normal reverse bias current of a semiconductor p-n junction diode including diffusion and generation-recombination components. In the forward bias region, diode 1 is forward biased while diode 2 is reverse biased. Thus the current is limited by diode 2. The current in bias region 2 and 3 represents the reverse bias current of the Schottky diode 2. The current in region 2 is the normal diffusion component of Schottky diode current. In region 3 starting from around 1.6 V forward bias, the current increases exponentially. The speculated mechanism is trap-assisted tunneling. Since S is a deep level dopant, it creates deep

level traps inside Ge bandgap. Also, the concentration of incorporated S is high as shown in the SIMS results. Thus trap-assisted tunneling current starts to dominate at a low bias voltage. At high laser fluence of  $2.6 \text{ J/cm}^2$ , more S atoms were incorporated into the Ge wafer. Consequently, as shown in Fig. 4.5, the dark current in the forward bias region shoots up at a lower forward bias voltage than the devices hyperdoped at lower laser fluences of 2 and  $2.3 \text{ J/cm}^2$ . Another evidence of the trap-assisted tunneling is the temperature-dependence of dark current. The current in region 3 is very weakly dependent on temperature which is consistent with the trap-assisted tunneling current [72]. Thus in the forward biased region, the current is dominated by trap-assistant tunneling caused by deep S traps in the Schottky diode formed by metal contacts and S-hyperdoped region.

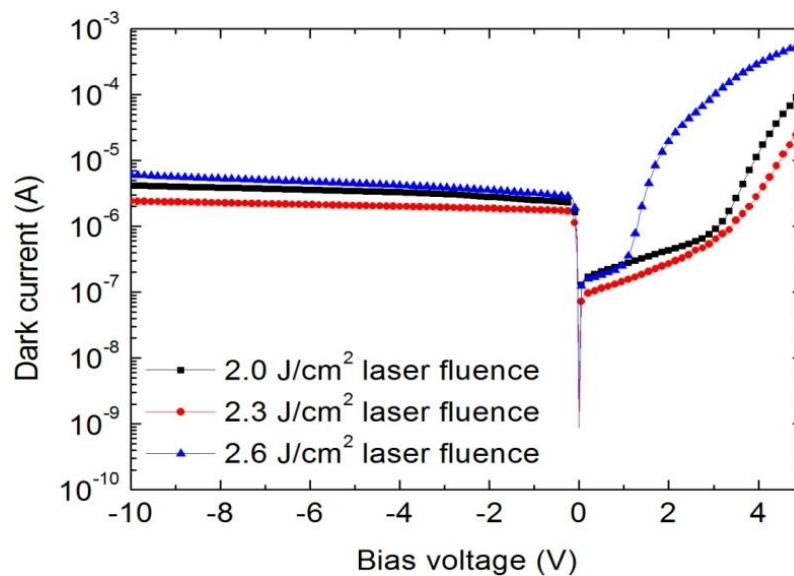


Fig. 4.5. I-V characteristics of S-doped Ge photodiode of mesa diameter  $180 \mu\text{m}$  fabricated on  $10 \sim 15 \Omega\cdot\text{cm}$  p-type Ge wafer using different laser fluence.

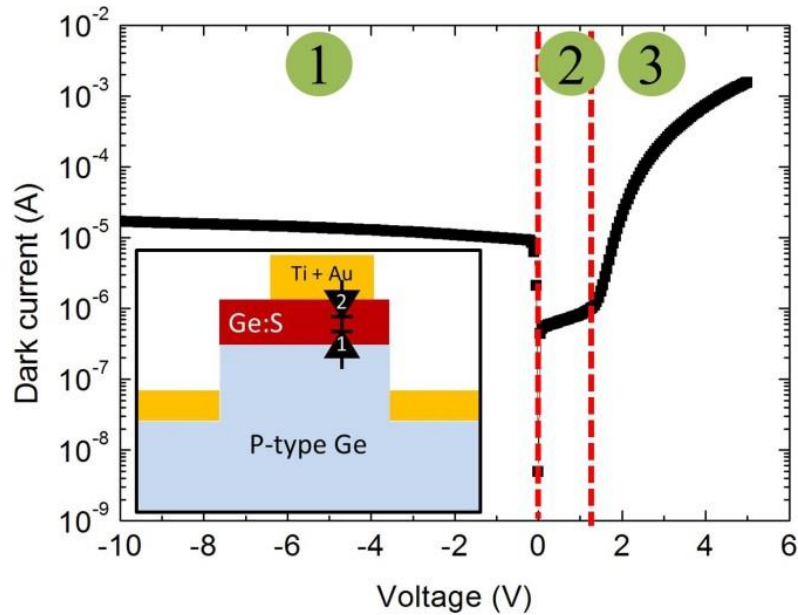


Fig. 4.6. I-V characteristics of S-doped Ge photodiode of mesa diameter 500  $\mu\text{m}$ . The inset shows the circuit schematic of the device.

The data for the EQEs of the photodiode fabricated on 10 ~ 15  $\Omega\cdot\text{cm}$  resistivity Ge wafer hyperdoped using different laser fluences are shown in Fig. 4.7 (a). The overall EQE of the device is high over a broad wavelength from ultraviolet (UV) to near infrared region (NIR). In the region of 260 ~ 300 nm and 700 ~ 1500 nm, the EQE is close to 100%. Taking into account of the optical reflection shown in Fig. 4.7 (b), the IQE is higher than 100%. In order to understand the mechanism governing the photo-response, the EQE of devices fabricated on the 10 ~ 15  $\Omega\cdot\text{cm}$  p-type wafer at different bias voltage are shown in Fig. 4.8. The EQE of a S-doped Ge photodiode fabricated on a 0.23 ~ 0.24  $\Omega\cdot\text{cm}$  p-type wafer using similar laser fluence is also shown in Fig. 4.8. The EQE of a commercial Ge photodetector is included in the figure as a comparison. As can be seen, the EQE of the S-doped Ge photodiode on the 10 ~ 15  $\Omega\cdot\text{cm}$  wafer is higher and extends to much lower wavelength spectrum than the commercial Ge photodetector.

There are three major characteristics of the EQE. First, the IQE is higher than unity, which cannot be explained by the conventional p-n junction theory. Also, the avalanche gain is not possible due to the weak built-in electric field at such low bias voltages. Second, the EQE increases with increasing reverse bias voltage and saturates at around 0.5 V reverse bias voltage. Last, the EQE of the device fabricated on high resistivity wafer is much higher than for the device fabricated on low resistivity wafer. Combining the three characteristics, the mechanism of the high EQE value is speculated to be based on photoconductive gain. Since high concentration of S atoms incorporated in Ge form lots of deep level traps within the Ge bandgap, electrons can be trapped in these energy states once they are generated by incident light. During the time when electrons are trapped, holes can loop around the device many times in order to keep the charge neutrality which results in a photoconductive gain. The photo-response ceases when electrons are detrapped from the S traps and recombine with holes. It is this photoconductive gain mechanism which could give the device an IQE larger than unity. The photoconductive gain is determined by the ratio of the trapping time  $\tau_s$  of electron in S traps to the transit time  $\tau_t$  of holes across the device [1]. The faster the holes move, the lower will be the transit time  $\tau_t$  and the higher EQE the device will have. At higher bias voltage, the stronger electric field will accelerate the holes to a higher velocity which would result in a higher photoconductive gain. Moreover, at higher bias voltage, depletion region of the p-n junction formed between the S-incorporated region and the p-type Ge substrate becomes wider and more S traps are included into the depletion region to be able to trap electrons, which will increase the EQE of the device further. On the other hand, at around 0.5 V reverse bias voltage, the velocity of holes becomes saturated and the transit time stops to decrease anymore. Also the depletion region is widened to a depth where S concentration decreases to very low value according to the dopant profile so that no more

significant amount of S traps are included into the depletion region. Thus, the EQE of the device saturates around 0.5 V reverse bias voltage. The combination of the hole velocity enhancement and the depletion region widening explains the voltage-dependence of EQE under reverse bias voltage. The device fabricated on higher resistivity wafer has wider depletion region than for the device on lower resistivity substrate. Hence, the EQE is higher for device on high resistivity wafer than on low resistivity substrate. Furthermore, the original carrier lifetime of high resistivity wafer is higher than for the low resistivity substrate. Also, under light illumination, the carrier lifetime is determined only by minority carriers for the low resistivity wafer since it is under low level injection condition. On the contrary, the carrier lifetime is determined by the sum of minority and majority carriers under light illumination for the high resistivity wafer since it is under high level injection condition [73]. Due to these two facts, carriers in device on high resistivity wafer can survive much longer in S trap states before recombining with holes than the device on low resistivity wafer under illumination. This results in a higher  $\tau_s$  value and thus a higher EQE. As a result, the EQE is much higher for device on high resistivity wafer than on low resistivity wafer. The high EQE extends into the UV region where the photons are absorbed in a shallow region containing high concentration of S atoms. As a result, the corresponding photoconductive gain is high due to the large amount of available S traps. The gain of the current Ge device is not as high as reported for the S-doped Si photodiodes [16]. It is possibly related to the different properties of S trap states and trapping capabilities in Si and Ge. As explained, it can be expected that the gain could be further increased by either using even higher resistivity Ge wafers or incorporating more S atoms into Ge.

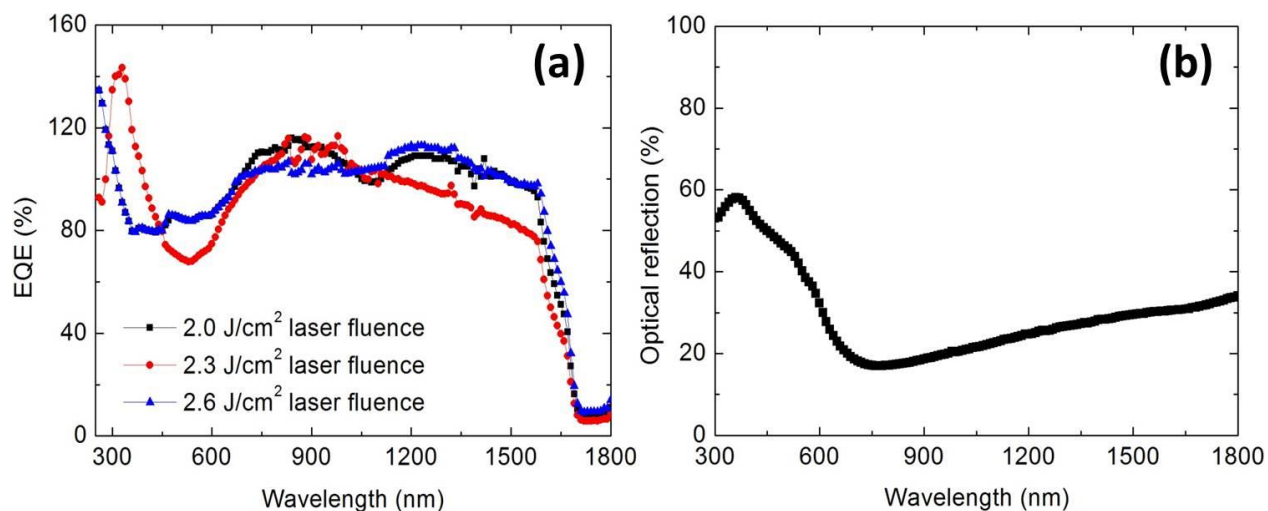


Fig. 4.7. (a) EQE of S-doped Ge photodiode fabricated on 10 ~ 15  $\Omega \cdot \text{cm}$  resistivity Ge wafers using different laser fluences. (b) Optical reflection of Ge with 100 nm SiO<sub>2</sub> ARC.

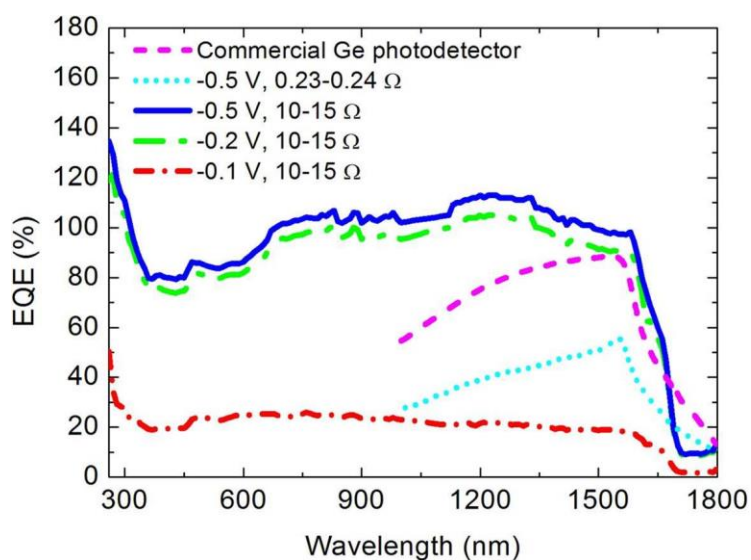


Fig. 4.8. EQE of S-doped Ge photodiode fabricated on different resistivity Ge wafers at various reverse bias voltages. EQE of a commercial Ge photodiode is also shown in the figure.

The device speed was measured by the temporal response to a picosecond laser pulse of 1310 nm wavelength. The result is shown in Fig. 4.9. The full width half maximum (FWHM) is 20 ns at 0.2 V reverse bias and 8 ns at 0.5 V reverse bias for all three devices fabricated using different laser fluences. This is expected because carriers are moving faster at higher bias voltage. The -3 dB bandwidth of the device at 0.5 V reverse bias was calculated to be about 20 MHz for the three devices by Fourier transform of the temporal response and the results are shown in Fig. 4.10. The bandwidth is much lower than about 200 MHz of the conventional Ge photodiodes [10] since the photoresponse is based on photoconductive gain mechanism and the speed might be limited by the slow detrapping of the electrons from the S traps. Although the speed is not high, the device is suitable in some broad wavelength high sensitivity imaging systems.

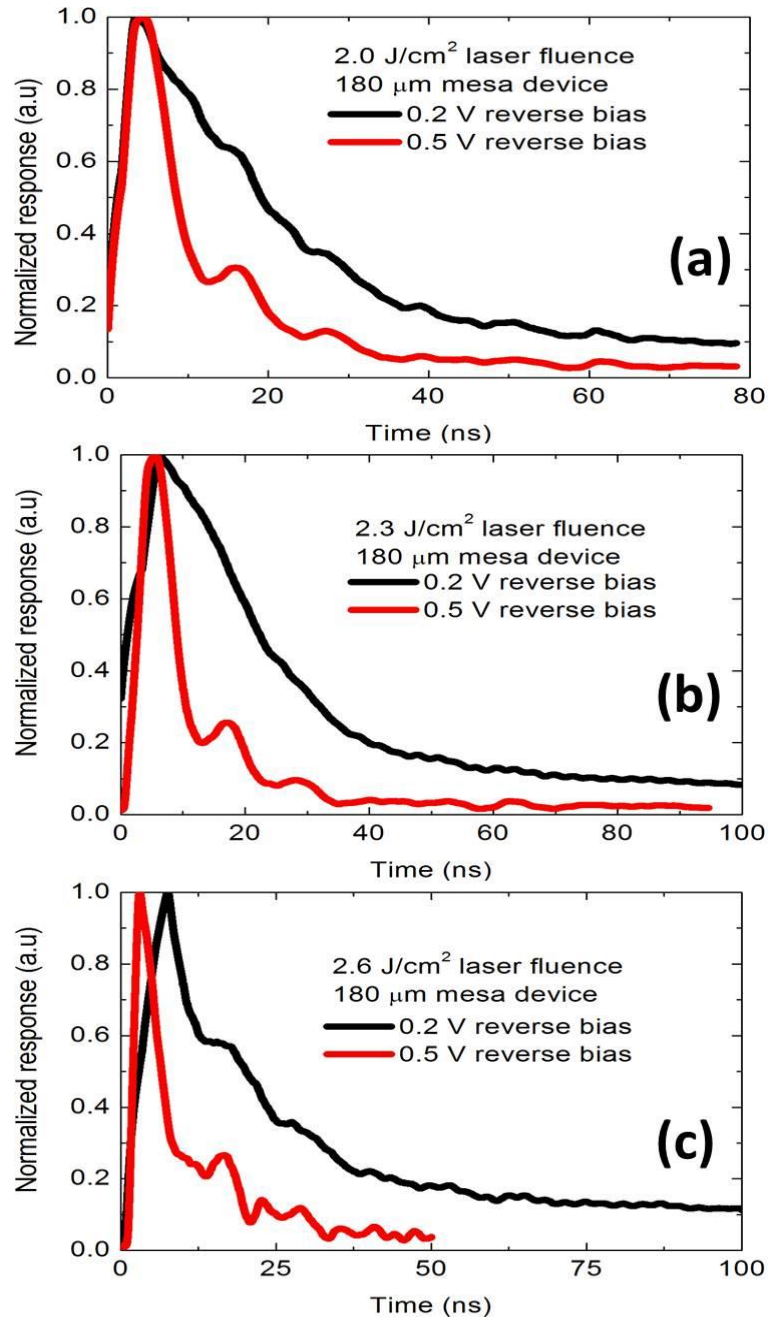


Fig. 4.9. Temporal response of S-doped Ge photodiode hyperdoped using laser fluences of (a) 2.0 J/cm<sup>2</sup>, (b) 2.3 J/cm<sup>2</sup> and (c) 2.6 J/cm<sup>2</sup> to a picosecond laser pulse of 1310 nm wavelength at 0.2 and 0.5 V reverse bias voltage.

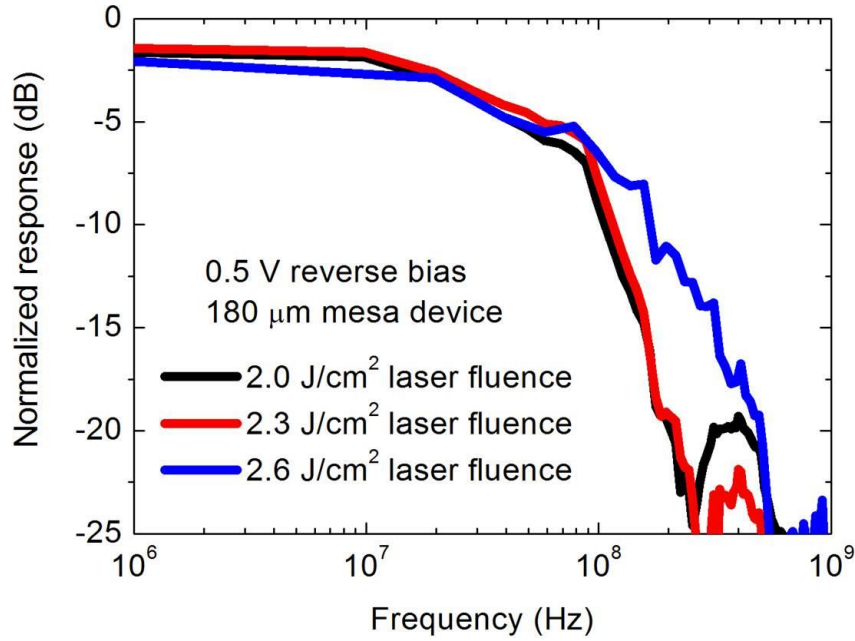


Fig. 4.10. -3 dB bandwidth of the S-doped photodiode calculated from Fourier transform of the temporal response.

The escape rate of electrons from the trap levels within the semiconductor bandgap is an exponential function of temperature

$$R \propto \exp\left(-\frac{E_T}{kT}\right)$$

where  $E_T$  is the trap level measured from the conduction band of the semiconductor,  $T$  is temperature and  $k$  is Boltzmann constant. If the device speed is limited by the detrapping of the electrons from the S traps, the decay rate of the photo-response of the device can reveal some information of the trap levels. So measurement of the decay rate of photo-response was carried out at different temperatures. The device was placed in a cryostat and the transient response to a 100 ns laser pulse of 1310 nm wavelength was measured from 200 K to 300 K. The results are

shown in Fig. 4.11. The decay rates of the photoresponse in the first stage are very close for all the temperatures but they differ in the second stage, which is somewhat opposite to the expectation. One explanation is that the mechanism of the device is not entirely dominated by the photoconductive gain. A large amount of photo-generated carriers still contribute to photo-current based on normal p-n junction mechanism while the rests contribute through photoconductive gain mechanism. Since the decay rate of the normal p-n junction response is faster than the response due to photoconductive gain mechanism, the decay in the first stage corresponds to the response based on normal p-n junction mechanism and hence it is very close at all temperatures. The decay in the second stage is based on the photoconductive gain mechanism and it increases with increasing temperature as expected from the equation. The second decay stage starts at a level of 20% of the total photo-response, which indicates the fact that only a portion of the photo-generated carriers were trapped on the S trap states and contributed to the photo-current through photoconductive gain mechanism. This is probably one of the reasons why the gain of the S-doped Ge photodiode is not as high as the value reported in the literature for the chalcogen-hyperdoped Si photodiode. Due to the high noise of the data, no useful information of the trap levels can be acquired from the results.

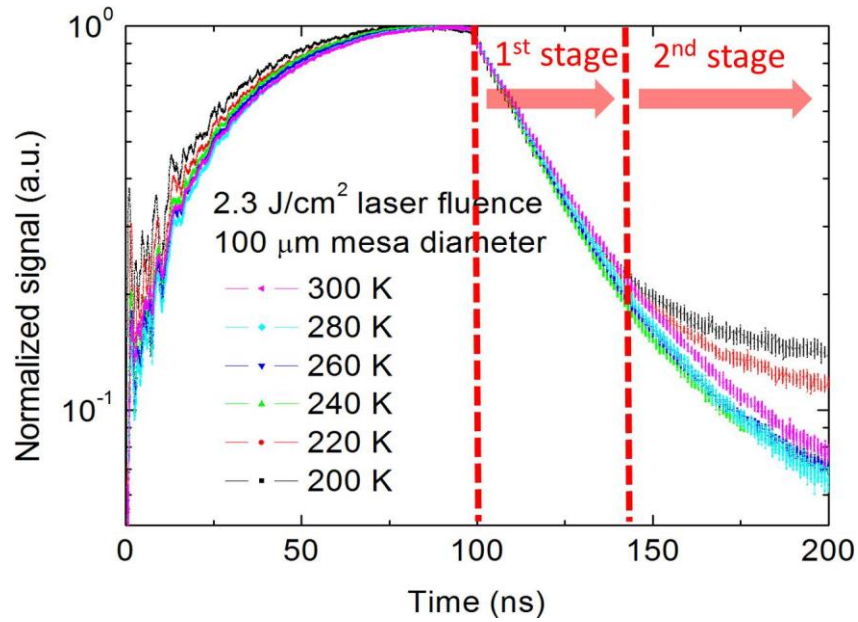


Fig. 4.11. Transient response of the device to a 100 ns laser pulse of 1310 nm wavelength.

#### 4.3.5 Results of devices on undoped wafer and hyperdoped using 1064 nm nanosecond laser

As discussed in the previous section, device fabricated on a higher resistivity wafer should have higher EQE based on photoconductive gain mechanism. To test this speculation, devices were fabricated on a nominally undoped Ge wafer. The dark I-V characteristics of the device are shown in Fig. 4.12 (a). The I-V characteristics of a Ge metal-semiconductor-metal (MSM) structure device fabricated on the same undoped Ge wafer and of a photodiode fabricated on the 10 ~ 15  $\Omega\cdot\text{cm}$  p-type Ge wafer are also shown in the figure as a comparison. The three device schematics are shown in Fig. 4.12 (b). Overall, the device fabricated on the undoped Ge wafer exhibited similar behavior as the device fabricated on the 10 ~ 15  $\Omega\cdot\text{cm}$  wafer, which is resulted from the opposite serial connection of diodes as explained previously. In the forward bias region, the dark current of the device is resulted from the Schottky junction. Since the

Schottky contact is formed between the metal contact and the S-hyperdoped region and the metal contacts have the same sizes for both devices, the I-V behavior of the device fabricated on the undoped Ge wafer resembles the device fabricated on the  $10 \sim 15 \Omega \cdot \text{cm}$  p-type Ge wafer. However, in the reverse bias region, the dark current of the device on the undoped Ge wafer is approximately two orders of magnitude higher than the device fabricated on the  $10 \sim 15 \Omega \cdot \text{cm}$  p-type Ge wafer. This high dark current should be due to the weak current rectification behavior of the diode formed between the S-hyperdoped region and the undoped Ge substrate. In the reverse bias region, diode 1 and diode 3 are forward-biased and thus the current through the device is limited by diode 2 for the device on the  $10 \sim 15 \Omega \cdot \text{cm}$  p-type Ge wafer and by diode 4 for the device on the undoped Ge wafer. According to the device schematics, diode 2 is a  $n^+$ -p junction established between the n-type S-hyperdoped region and the p-type Ge substrate while diode 4 is an  $n^+$ -n high-low junction established between the n-type S-hyperdoped region and the nominally undoped, actually very lightly n-type doped Ge substrate. Consequently, the current rectifying behavior of diode 2 is much stronger than diode 4 because of the stronger built-in electric field. As a result, the reverse-biased dark current of the device on the  $10 \sim 15 \Omega \cdot \text{cm}$  p-type Ge wafer is much lower than the device on the undoped Ge wafer. This effect is more drastic for the Ge MSM structure device due to the even weaker current rectifying behavior and the large area of the Schottky diode 7 formed between the undoped Ge wafer and the metal contact as illustrated in Fig. 4.12 (b). In short, devices on higher resistivity wafer have undesirable higher dark current which is not suitable for many high sensitivity applications.

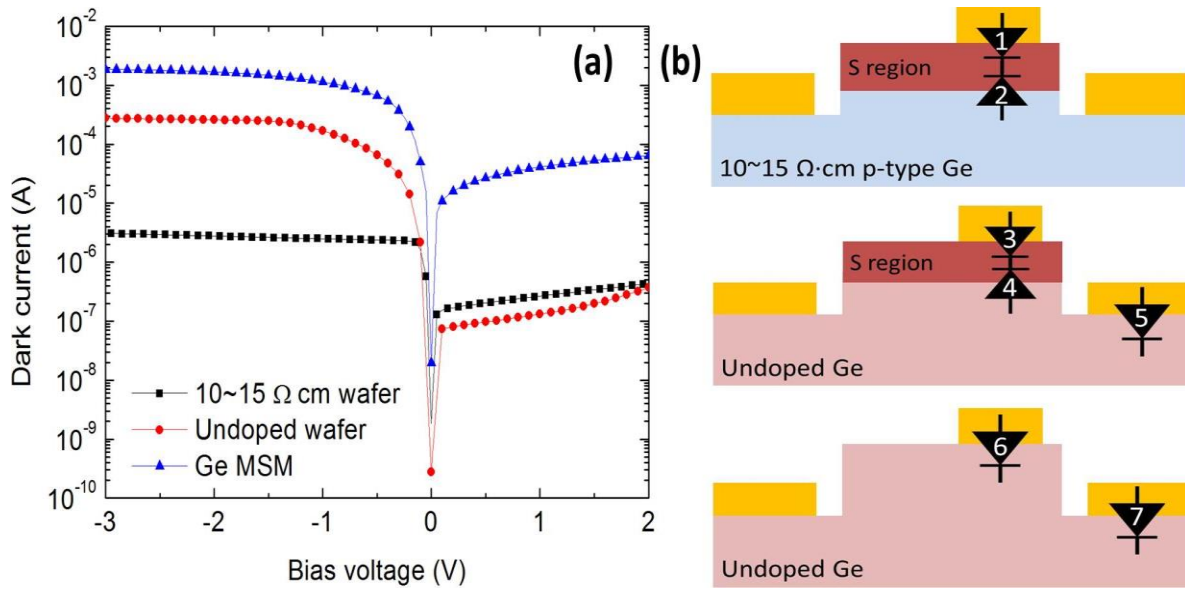


Fig. 4.12. (a) I-V characteristics of S-doped Ge photodiode of mesa diameter 180  $\mu\text{m}$  on undoped Ge wafer using different laser fluence. (b) Schematics of the three devices in (a).

Table 4.1. EQE at -0.5 V bias of three different types of S-hyperdoped Ge device at four different wavelength.

	1	2	3
532 nm	0.837	0.513	NA
633 nm	0.905	0.624	NA
1310 nm	1.08	0.765	NA
1550 nm	0.966	0.769	0.4

The EQE of the device on the undoped Ge wafer and the device of Ge MSM structure were measured at four wavelength (532 nm, 633 nm, 1310 nm and 1551 nm) using lasers as the excitation sources. The results are shown in Table 4.1. As a comparison, EQE of the device on the 10 ~ 15  $\Omega\cdot\text{cm}$  p-type Ge wafer is also listed in the table. Contrary to our expectation, the device on the 10 ~ 15  $\Omega\cdot\text{cm}$  p-type Ge wafer has an overall higher EQE than the device on the undoped Ge wafer. The device of Ge MSM structure has the lowest EQE. The reason for the lower EQE of the device on the undoped Ge wafer is likely due to the weak built-in electric field of the  $n^+n$  high-low junction. One function of the built-in electric field is to dissociate the photo-generated electron-hole pairs to reach into separate regions in order to prevent the recombination and in turn they can be collected. The stronger the built-in electric field, the more capable it is of separating the photo-generated electron-hole pairs. The device on the undoped Ge wafer has a weak built-in electric field and thus the separation of photo-generated electron-hole pairs is not as efficient as the device on the 10 ~ 15  $\Omega\cdot\text{cm}$  p-type Ge wafer, which in turn leads to a lower EQE. This effect is even more drastic for the MSM structure device. The electron-hole pairs are not effectively separated due to the lack of such built-in electric field. The carriers are not spatially separated and have to survive the recombination during a long-distance traveling to be collected by the top and bottom metal contacts. As a result, lots of recombination occurs during the travelling which results in the lowest EQE. On the other hand, the built-in electric field also accelerates the carriers when they are drifted across the junction. A stronger built-in electric field leads to a short transit time across the junction. As discussed previously, the photoconductive gain is inversely proportional to the carrier transit time  $\tau_t$ . As a result, the weaker built-in electric field of the device on the undoped Ge wafer leads to a longer transit time and thus a lower photoconductive gain. The Ge MSM device does not have S deep level traps and it lacks

photoconductive gain. In short, the overall EQE of the device on the undoped wafer is lower than the device on the  $10 \sim 15 \Omega\cdot\text{cm}$  p-type Ge wafer. The reason is the ineffective separation of the photo-generated carriers and long carrier transit time across the junction, both of which could be due to the weak built-in electric field. Thus, higher resistivity wafer does not guarantee a higher EQE and other factors should be taken into account while designing the device structure in order to improve the EQE.

#### **4.3.6 DLTS results**

The S trap levels in Ge were investigated by deep level transient spectroscopy (DLTS) measurement on the photodiode and the result is shown in Table. 4.2. There are three trap levels shown in the table. Although the DLTS signal is more sensitive to the traps in the lightly-doped side of the junction, some of the signal can still come from the heavily S-hyperdoped side. Moreover, the tail of the S profile extends into the lightly-doped p-type side. As a result, it is likely that one of the trap levels might be related to the incorporated S. The trap level of 0.203 eV is speculated to be associated with S according to the value reported in the literature [67]. The concentration of this trap might not indicate the real concentration of S traps in the device since the DLTS signal is not sensitive to the heavily-doped S-hyperdoped side and the S concentration in the lightly-doped p-type substrate is low. The capture cross section is small which indicates the weak trapping capability of these traps. The small capture cross section is probably the reasons why the photoconductive gain of the photodiode based-on S-hyperdoped Ge is much lower than its Si-based counterpart. The origins of the other two trap levels are not clear. They might be related to the laser-induced defects. Further investigation needs to be carried out. In

addition, more appropriate device structure needs to be designed for more detailed investigation of the S trap levels.

Table 4.2. DLTS result of trap levels in S-hyperdoped Ge photodiode.

Energy (eV)	Capture cross section (cm <sup>2</sup> )	Concentration (cm <sup>-3</sup> )
0.086	$9 \times 10^{-17}$	$2.6 \times 10^{12}$
0.105	$2 \times 10^{-18}$	$1.4 \times 10^{13}$
0.203	$2 \times 10^{-17}$	$1.9 \times 10^{13}$

#### 4.4 Summary

In conclusion, high concentration of S dopant atoms was successfully achieved into the Ge substrate by pulsed laser hyperdoping process. The S dopant profile was investigated by SIMS measurement. The profile had a sharp peak concentration of  $2 \times 10^{19} \text{ cm}^{-3}$  at the surface and extended only to about 50 nm into the bulk. The Ge photodiode based on S doping was fabricated and characterized. It has been found that the out-diffusion of the S atoms should be prevented and proper thermal activation of S atoms should be done in order to achieve a rectifying junction. The typical I-V characteristics showed the behavior of opposite series connection of two diodes. The EQE of the device fabricated on  $10 \sim 15 \ \Omega \cdot \text{cm}$  p-type Ge wafer remained high from UV to NIR region and IQE was higher than unity. The photoconductive gain mechanism as well as the conventional p-n junction mechanism governs the photo-response of the device with the latter being the majority part. The speed of the device was dominated by the

detrapping of electrons from S trap states and the -3 dB bandwidth of the device was measured to be 20 MHz. The choice of the starting wafer has a big impact on the final device performance. An optimum balance between wide depletion region and strong built-in electric field is crucial for the optimum performance of the device. The sulfur trap levels were measured by DLTS. One of the defect levels is speculated to be related to the S. The trapping capability was weak, which might explain the lower photo-gain compared to the photodiode based on S-hyperdoped Si. For the first time, S has been demonstrated to be an effective deep level dopant to improve the performance of Ge devices. The physical mechanism of this novel device was investigated.

## Chapter 5:

### Conclusion and Future Work

#### 5.1 Conclusion

In this work, to overcome the challenges of the conventional fabrication methods and improve the performance of the Ge-based optoelectronic devices, high power lasers were investigated in three areas of the device fabrication. Based on the studies, the following conclusions can be drawn:

1. Short pulsed laser is capable of producing microtextured Ge surface. The microtextured Ge surfaces had low optical reflections ( $< 8\%$ ) over broad spectrum and is insensitive to the incident angle.
2. The laser-induced defects generated during microtexturing process can be eliminated by shallow post-microtexture chemical etching.
3. The EQE of the Ge photodiode fabricated on the laser-microtextured surface was higher over a broad spectrum and extended to shorter wavelength compared to the flat surface device with other performance similar.
4. Laser doping has been demonstrated to be an effective doping method for Ge. High concentration of phosphorus atoms up to  $2 \times 10^{19} \text{ cm}^{-3}$  was incorporated into the Ge wafer. Sheet resistance can be varied by the laser fluence and the number of laser pulses.

5. The laser-doped Ge p-n junction showed similar dark current density as the Ge p-n junction formed by thermal diffusion. The dark current was dominated by the laser-induced defects.
6. High concentration of S atoms up to  $2 \times 10^{19} \text{ cm}^{-3}$  was successfully incorporated into Ge substrate by short pulsed laser. The high concentration profile was confined within 50 nm beneath the surface. The combination of laser-assisted photochemical etching, dopant out-diffusion and dopant segregation resulted in the shallow profile.
7. The laser-incorporated S atoms act as dopants in Ge. Rectification junction was formed based on S-hyperdoped Ge. The photodiode fabricated on S-hyperdoped Ge showed IQE larger than unity. The speed of the device was limited by the slow detrapping of electrons from the S trap states.
8. The working mechanism of the photodiode based on S-hyperdoped Ge was speculated to be based on photoconductive gain although majority of the photo-response was still dominated by conventional p-n junction mechanism.
9. DLTS measurement was carried out to investigate the S trap energy levels. The trap level was speculated to be 0.203 eV below the conduction band based on the DLTS results and the value reported in the literature. A crude calculation of band diagram was carried out and it matched the SIMS and DLTS results reasonably well.

So the three major steps in Ge-based optoelectronic device fabrication: reduction of surface reflection by microtexturing, Ge junction formation by laser doping and high concentration doping of S on Ge were successfully demonstrated using pulsed laser processing method.

## 5.2 Future work

### 5.2.1 Ge device with nanoscale textured surface

Although the microtextured Ge surfaces show very low optical reflection, the structures need to be chemically etched to remove the laser-induced defects for optoelectronic device applications. The post-microtexture chemical etching inevitably smoothens the surface and increases the optical reflection. Ideally speaking, only very thin surface layer of about 1  $\mu\text{m}$  material which contains defects and impurities needs to be removed to restore the good electrical properties and at the same time the optical reflection is still kept low. Unfortunately, the surface morphology with deep structures after short-time post-microtexture chemical etching is not suitable for doping purposes. For ion implantation, the sharp edges don't receive enough dopant ions during the ion bombardment due to the small effective cross-sectional area and shadowing effect from the blunt tips of the microtexture structures. The situation is worsened by the fact that the ion implantation is usually done at a tilted angle to avoid the channeling effect. The device shunting problem and illustration of the shadowing effect are shown in Fig. 2.12 (a) and Fig. 2.13 respectively. As a result, the heavily-microtextured surface morphology does not lead to uniform doping. Thermal diffusion from spin-on-dopant does not work for the heavily-microtextured surface morphology either. The reason is that the spin-on-dopant solution P507 only sits in the deep valley regions instead of forming a uniform conformal coating on the surface after spin coating as shown in Fig. 5.1. After thermal diffusion, the sharp tip and edge regions are left undoped due to the absence of spin-on-dopant coating on them. As a result, the final device suffered low shunt resistance. More viscous spin-on-dopant solution P509 does form a conformal coating on the microtextured surface as shown in Fig. 5.2. But surface desorption pits were observed after thermal diffusion. The speculated reason for these pits is due to the

interaction between the chemicals in P509 and Ge. In short, spin-on-dopant is not capable of effectively doping the heavily-microtextured surfaces. Gas phase doping might work on heavily-microtextured surfaces but the cost is high and we do not have the capability. Thus, we encounter a difficulty that heavily-microtextured surface morphology is desired for low optical reflection but smoother surface morphology is required for uniform doping.

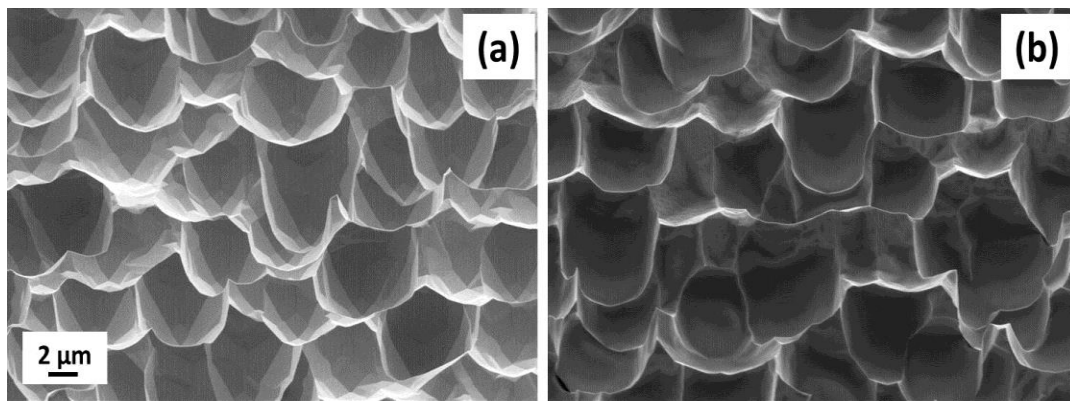


Fig. 5.1. (a) microtextured Ge surface before applying P507. (b) after applying P507.

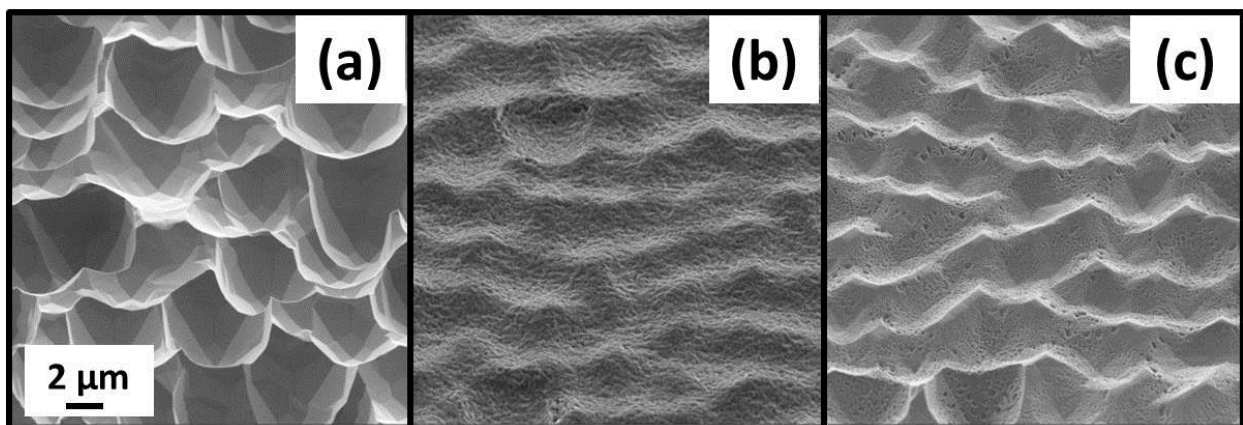


Fig. 5.2. (a) microtextured Ge surface before applying P509. (b) after applying P509. (c) after thermal diffusion at 580 °C for 2 minutes and removal of P509 coating.

One solution to this problem to achieve low optical reflection and effective doping is the nanoscale surface texturing. Many methods which can create nanoscale surface texture have been reported in the literature such as metal-assisted etching [74, 75], nanosphere lithography [23-25], block copolymer lithography [76, 77], cryogenic dry etching [78] and laser interference lithography [79]. When the spacing of the surface structures becomes smaller than the wavelength of the incident light, the low optical reflection is no longer due to multiple reflection of the incident light. The graded refractive index becomes the mechanism for reducing the optical reflection. The optical reflection of the nanoscale textured surface can be still below 1 %. More important, the optical reflection can still be kept very low even for the nanoscale surface structures with several hundreds of nanometer in height. The shallow surface morphology is expected to be suitable for effective doping. For ion implantation, the shadowing effect will be less than the deep structures. For thermal diffusion from spin-on-dopant source, P507 might form a conformal coating due to the shallow depth of the morphology. Thus, nanoscale texture could provide a surface with extremely low optical reflection as well as a good surface morphology for uniform doping. As a result, Ge optoelectronic device fabricated on the nanoscale textured surface is expected to perform better than the device fabricated on the laser-microtextured surface.

### **5.2.2 Sub-bandgap optical absorption of S-hyperdoped Ge**

As introduced in chapter 4, the S-hyperdoped Si shows strong optical absorption in the sub-bandgap spectrum. The mechanism of the sub-bandgap absorption is the optical transition of electrons involving the S intermediate band within the Si bandgap. The similar sub-bandgap

optical absorption would be expected for S-hyperdoped Ge. Some initial optical absorption measurement at sub-bandgap wavelength was carried out. A semiconductor laser diode of 2.35  $\mu\text{m}$  (SAR-2350-20, Sarnoff Corporation) was used as the light source. Due to the divergence of the beam, a lens and an iris were used to focus the beam onto the sample. The sample was mounted in an integrated sphere (Model#RTC-060-SF, Labsphere Inc.). A PbS photoconductor (PDA30G, Thorlabs) was mounted at the bottom of the integrated sphere to measure the optical power. A gold sample was used as white standard and a black standard purchased from Labsphere Inc. was used. The measured value from the sample was normalized to the dark and the white standard. The experimental setup is shown in Fig. 5.3. The results are listed in table 5.1. The bare Ge without any laser treatment showed no optical absorption at this wavelength since the photon energy is smaller than the bandgap. The Ge samples that underwent laser hyperdoping showed optical absorption at 2.35  $\mu\text{m}$ . Comparing the results for sample #2 and sample #3, the absorption increases with increasing laser fluence. At higher laser fluence, more S atoms could be incorporated into the Ge substrate and the S profile penetrates deeper, which would cause more optical absorption. Moreover, higher laser fluence creates deeper surface structures, which further enhances the absorption. The absorption of Ge hyperdoped using 1064 nm wavelength laser showed lower absorption than the sample hyperdoped using 532 nm wavelength laser. The possible reason could be due to the relative flat surface compared to the heavily-microtextured surface morphology created by the 532 nm wavelength laser. The sample hyperdoped in  $\text{O}_2$  also showed some sub-bandgap absorption, which is consistent with the literature [80]. Unfortunately, no rectification junction could be formed based on  $\text{O}_2$ -hyperdoped Ge. The absolute absorption values depend on the optical alignment. Although much effort has been made to get the best alignment but it was still not perfect due to the poor quality of the laser

diode beam. Also, the error could come from the PbS photoconductor, which is not well calibrated. But the general trend acquired from the results is correct.

These are just some preliminary sub-bandgap absorption measurements. More experiments should be done to investigate the extended absorption edge, effect of laser hyperdoping parameters on the sub-bandgap absorption, physical mechanism of the sub-bandgap absorption and thermal annealing effect on the sub-bandgap optical absorption. Also, more well-established experimental setup could be used for more accurate optical measurements. For example, an integrated sphere equipped with a more collimated broad wavelength mid-infrared light source can give better optical alignment and continuous absorption spectrum. Moreover, a well calibrated power meter could be used to measure the optical power.

Photodiodes based on S-hyperdoped Si have shown extended photoresponse beyond bandgap [16]. Whether the sub-bandgap photoresponse exists for photodiodes based on S-hyperdoped Ge needs to be verified. Although S-hyperdoped Ge shows optical absorption at 2.35  $\mu\text{m}$  wavelength, this doesn't necessarily indicate that the photodiode is photo-active up to this wavelength. The photo-generated carriers might not be effectively extracted from the device or the photoresponse might not extend that far beyond the Ge bandgap just like its Si counterpart [16]. Quantum efficiency measurements should be carried out to verify the sub-bandgap performance of the device. Usually a quantum efficiency measurement setup equipped with a Fourier transform infrared spectroscopy (FTIR) instrument could be used to give a continuous EQE spectra in mid-infrared wavelength.

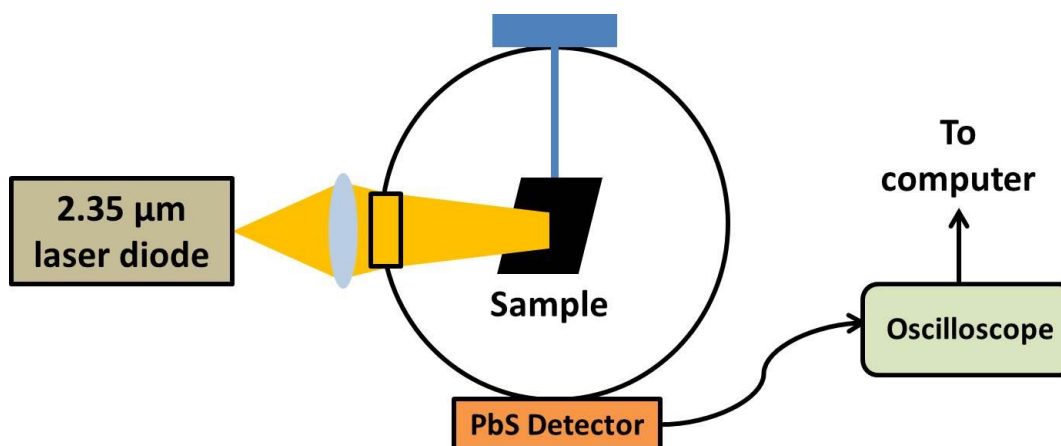


Fig. 5.3. Experimental setup for sub-bandgap optical absorption measurement.

Table 5.1 Optical absorption measurement of S-hyperdoped Ge samples at 2.35 μm wavelength.

Sample	Hyperdoping gas environment	Laser wavelength (nm)	Laser hyperdoping fluence ( $\text{J}/\text{cm}^2$ )	Optical absorption (%)
#1	NA	NA	NA	< 1
#2	SF <sub>6</sub>	532	1.4	60
#3	SF <sub>6</sub>	532	2.1	77
#4	SF <sub>6</sub>	1064	2.6	40
#5	O <sub>2</sub>	532	2.1	60

### 5.2.3 Determination of sulfur defect levels

The DLTS result didn't really give concrete information of the S trap energy levels inside the Ge bandgap. Due to the discussion in section 4.3.6, the value of 0.203 eV below the

conduction band is just a speculation based on the results in the literature. More accurate determination of S trap energy level should be acquired using a Schottky junction device structure or through other measurements such as temperature-dependent Hall and resistivity measurements [53].

#### **5.2.4 Investigation of the physical mechanism for lower photo-gain of device based on S-hyperdoped Ge**

Photodiodes based on S-hyperdoped Ge showed relatively low photo-gain while their Si counterparts showed photo-gain up to 20 times. The physical mechanism of this difference is not clear. It might be related to different configurations of S traps within Si and Ge. Experiments should be carried out to investigate the S trap properties within both materials. For example, DLTS measurement could provide the information of trap energy level and trap cross section but careful design of the structure is needed for the DLTS measurement in order to reveal the real defect levels. With detailed measured S trap parameters, the reason for low gain of S-hyperdoped Ge photodiode might be explained.

## **Chapter 6:**

# **Laser Sintering of Silicon Nanoparticles for Photovoltaic**

## **Applications**

### **6.1 Introduction**

Polycrystalline Si thin films have many applications in optoelectronic and electronic devices such as thin film solar cells and thin film transistors for large area displays. Polycrystalline Si thin films are traditionally grown by chemical vapor deposition, which is a relatively high-cost method. Si nanoparticles can be an alternative low-cost material source for Si thin films. These can be produced cost-effectively in bulk quantities. Also in industry, a large amount of raw materials gets wasted due to kerf losses when the Si ingots are cut into wafers. About 50 % of the Si is lost during sawing process [81]. This saw dust can also be used as an alternative material source for forming Si thin films. The deposition of particles onto a substrate followed by subsequent sintering can transform the particles into a continuous nano- or micro-crystalline Si layer. Recently, Si and Ge nanoparticle-based thin films have been formed using a plasma-based deposition method [82]. However, these films need to be sintered in order to achieve high density and the conventional furnace sintering requires high temperature and high pressure [81]. Laser processing is an alternative method for particle sintering as it eliminates the huge thermal budget required by furnace sintering and thus reduces the production cost. In this work, as an initial investigation, low-cost, commercially available Si nanoparticles were sintered

into a Si thin film by means of laser irradiation. To show the applicability of the layer in actual device applications, a solar cell was fabricated using a laser-sintered emitter and the device performance was studied.

## 6.2 Experimental

Spherical Si nanoparticles of 50 nm diameter were purchased from MTI Corporation. The nanoparticles were dispersed in ethanol with a concentration of 3 wt%. The solution was sonicated using an ultrasonic probe (Sonicator 3000, Misonix Inc.) for 30 minutes to further break the agglomerated raw particles. The solution was then spin-coated on 1.5 cm × 1.5 cm p-type Cz-Si wafer ( $\rho=1 \text{ } \Omega\cdot\text{cm}$ ; thickness 380  $\mu\text{m}$ ). The wafer was cleaned by acetone, methanol and a 5 minute dip in 5% HF prior to spin coating. A soft-baking step at 100 °C was done on a hot-plate for 10 minutes to evaporate the ethanol in the coating. Then the sample was dipped in 0.02 % HF to etch away the native oxide on the raw particles. Finally, the layer was sintered by a continuous wave 532 nm laser (Coherent V18). The laser beam was focused down to a spot of about 30  $\mu\text{m}$  diameter. The sample was placed in a vacuum chamber which was mounted on a computer-controlled X-Y stage and scanned during laser sintering. SEM was used to examine the morphology. XRD (Smart-Lab®, Rigaku. Inc) was used to examine the crystal structure.

The solar cell was fabricated using a traditional process flow [83]. The sintered layer was doped using spin-on-dopant (P509, Filmtronics) by thermal diffusion at 900 °C for 15 minutes. A 10 nm oxide layer was thermally grown and a 70 nm silicon nitride layer was deposited by PECVD as the surface passivation and as an antireflection coating. The back contact and back surface field were formed by Al paste (Ferro 53-038) with subsequent firing at 750 °C for 5

minutes in a furnace. The front contact was patterned by photolithography, and then a stack of Ti/Pd/Ag (50 nm/50 nm/1  $\mu\text{m}$ ) was deposited in sequence by e-beam evaporation. The front contact was thickened to about 1  $\mu\text{m}$  by silver electroplating to reduce the series resistance.

The device I-V measurements were carried out using a class B solar simulator purchased from PV Measurements, Inc. Device parameters such as short-circuit current, open-circuit voltage, fill factor, shunt resistance, series resistance and efficiency were extracted using the software. IQE measurements were performed using the same I-V setup. Individual wavelengths were selected from a tungsten halogen lamp using a 270M Jobin Yvon monochromator and the power of each wavelength was measured by a Newport 842-P power meter. Base minority carrier lifetime was measured using open-circuit voltage decay method [84]. Light-Beam Induced Current mapping (LBIC) was done by mounting the sample on a computer-controlled translational X-Y stage using a green diode laser. The short-circuit current was measured using the same setup and software as the I-V measurement.

## **6.3 Results and discussion**

### **6.3.1 Si nanoparticle sintering**

Sintering was carried out using a 532 nm CW laser. The incident laser beam was well absorbed by the particle layer because the absorption depth for bulk Si is about 1  $\mu\text{m}$  at 532 nm. The morphology of the sintered layer using different incident laser power is shown in Fig. 6.1. The particles in the layer became more interconnected as the laser power increased. At 14 W of laser power, the layer was melted and a solid Si thin layer was formed.

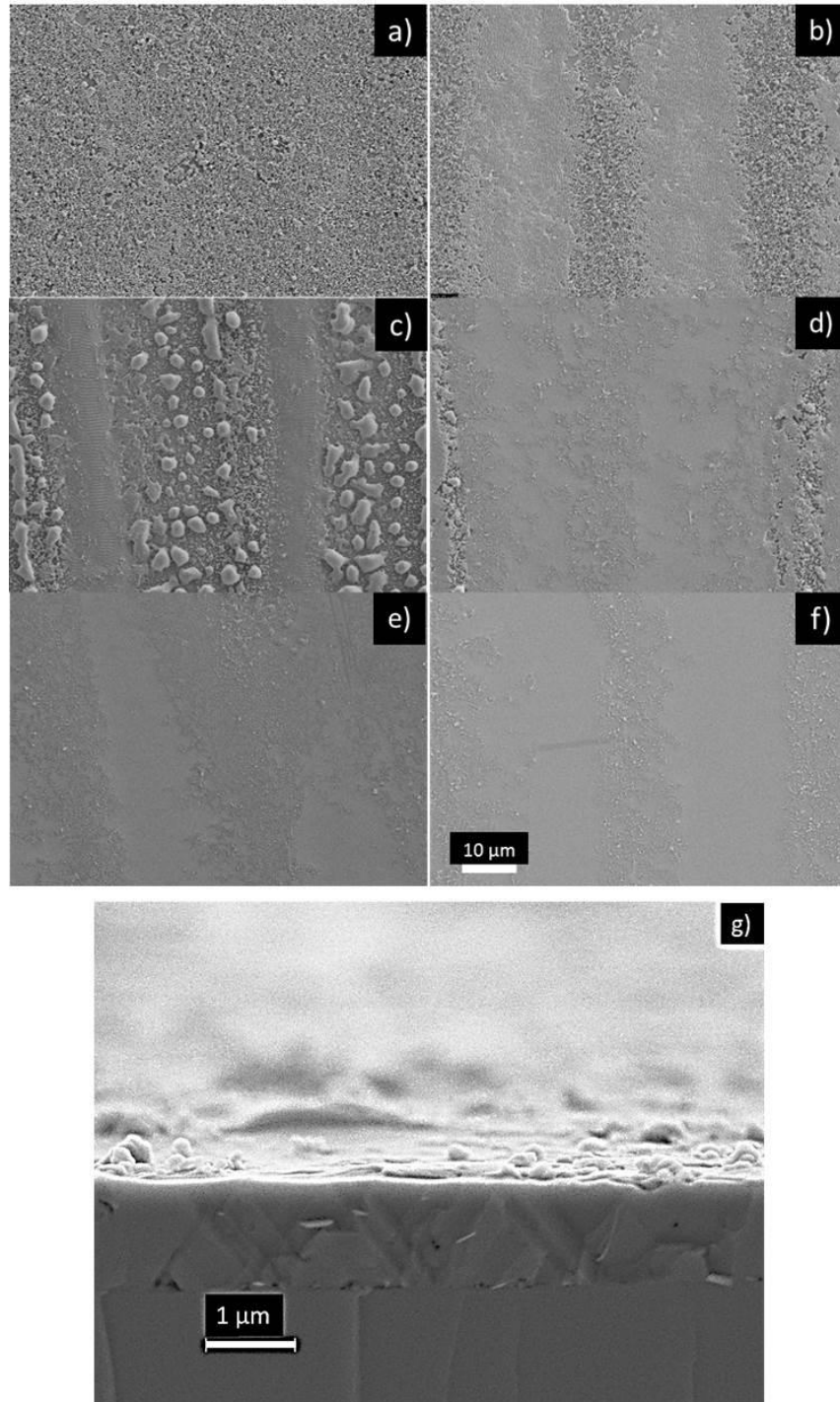


Fig. 6.1. Morphology of sintered layer under different incident laser power (a) 4 W (b) 6 W (c) 8 W (d) 10 W (e) 12 W (f) 14 W (g) cross section of laser-sintered sample using 14 W.

The crystal structure of the sintered film was evaluated using XRD. The results are shown in Fig. 6.2. Several peaks that were observed in the raw coating disappeared in the sintered layer, which indicates a more ordered crystalline structure. The main (400) peak of the sintered layer was broader compared to the substrate, which might come from small crystallite size in the sintered film or laser induced stress in the substrate.

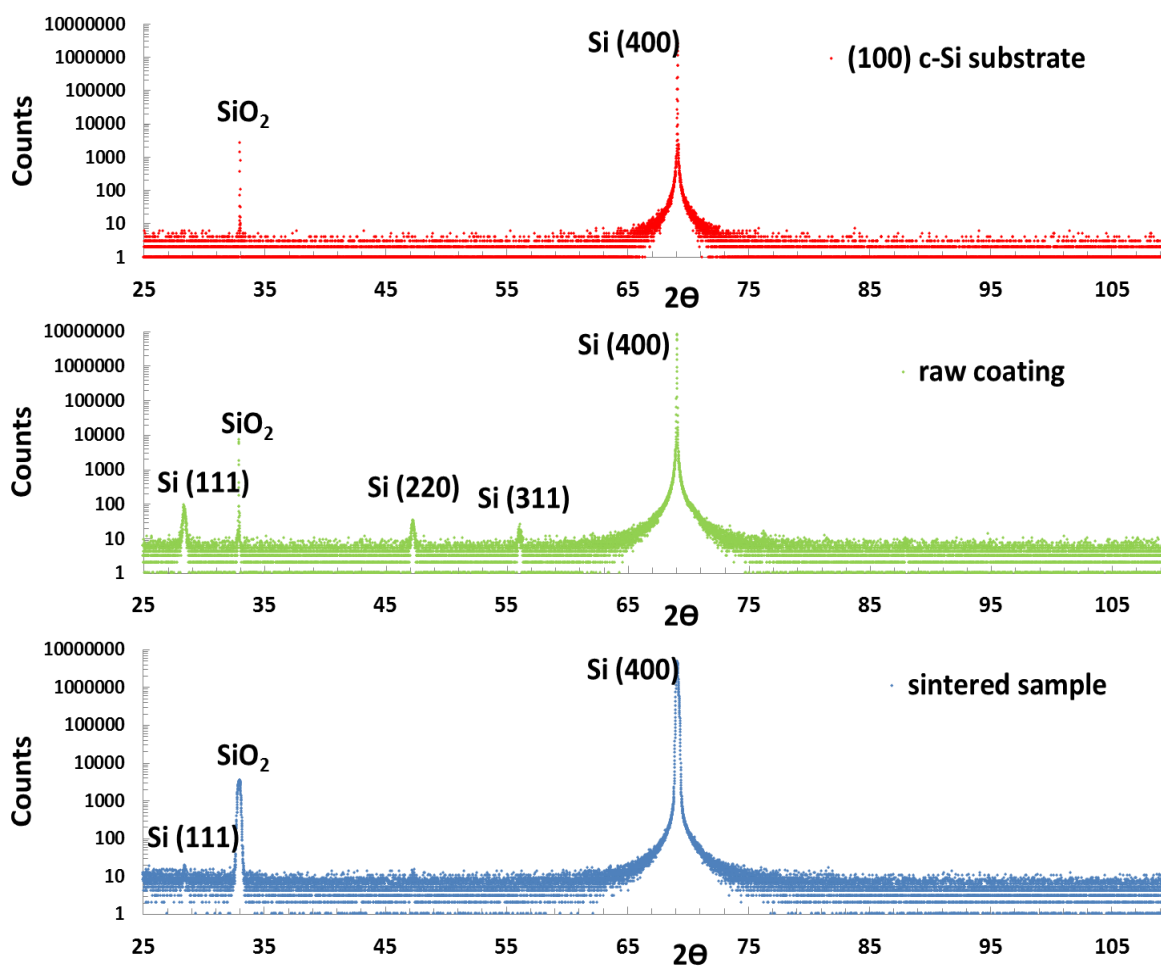


Fig. 6.2. XRD results of (100) c-Si substrate, raw coating and sintered sample.

### 6.3.2 Device characterization

The device based on sintered Si nanoparticles showed an efficiency of 2.6 % with an open-circuit voltage of 404 mV, a short-circuit current of 11.14 mA/cm<sup>2</sup> and a fill factor of 57.6%. The IQE of the devices with sintered emitter and standard emitter are shown in Fig. 6.3. Three characteristics can be observed in the device with sintered emitter. First, the peak in IQE from 400 nm to 440 nm is because of the efficient dissociation of photo-generated electron-hole pairs in the depletion region. Yet the IQE was still lower than the device with standard emitter due to the poor quality of the sintered layer. Secondly, above around 1000 nm the IQE increases slightly, which could be resulted from the back surface field formed by the alloy between the Si wafer and Al paste. Third, the IQE of the device with sintered emitter from 480 nm to 1000 nm is much lower than the device with standard emitter.

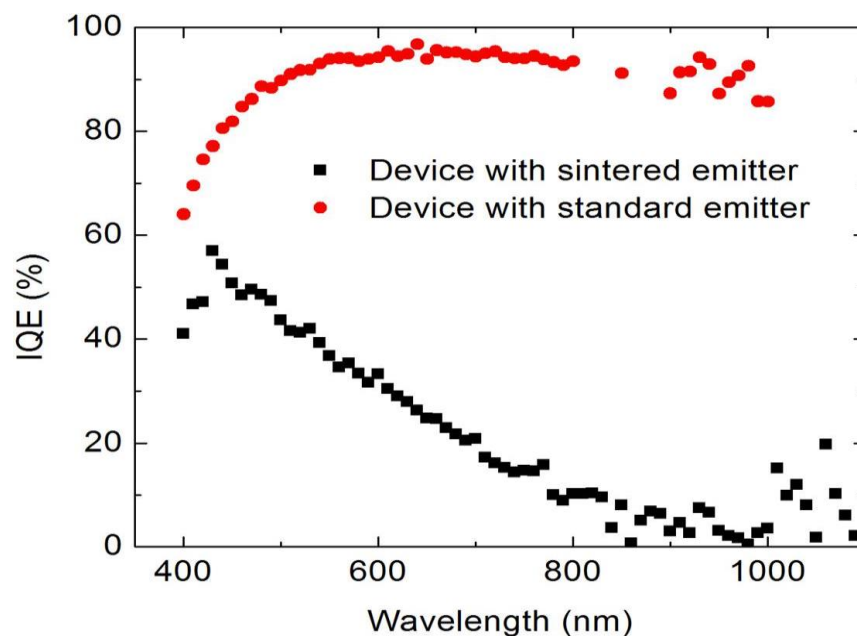


Fig. 6.3. IQE of the devices with sintered and standard emitter.

There could be two major reasons for the low IQE from 480 nm to 1000 nm. One could be the low minority carrier lifetime in the base. To test this hypothesis, the base minority carrier lifetime was measured using an open-circuit voltage decay method. A 980 nm laser diode was used to extract the information from the base. The result is shown in Fig. 6.4. The base minority carrier lifetime of the device with sintered emitter was comparable to the standard device. Therefore, minority carrier lifetime of the base was not the reason for the low IQE. The other reason could be the interface between the sintered layer and the substrate. Carriers can recombine at this interface. The cross-section SEM image in Fig. 6.5 shows some laser-induced melted regions at the interface, labeled by the red circles. The laser scanned lines are labeled by the blue arrows in the figure. The dark regions beneath the laser scanned paths are the melted area at the interface. After the laser energy being absorbed by the nanoparticles, the remaining laser energy melted the surface region of the substrate. The melting and cooling during the sintering process might have left some defects at the interface. These defects could cause a high recombination rate at the interface where the minority carriers generated in the base recombine at the interface before they are drifted across the junction and therefore do not contribute to the photocurrent. Thus, the IQE is low for long wavelengths. High recombination also could be due to inter-particle interfaces in the sintered film.

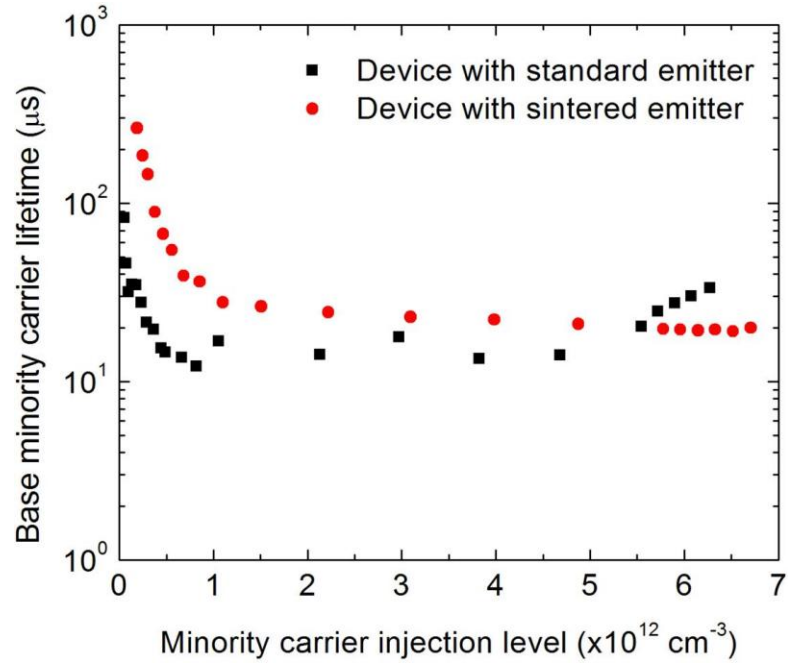


Fig. 6.4. Base minority carrier lifetime of the device with sintered and standard emitter.

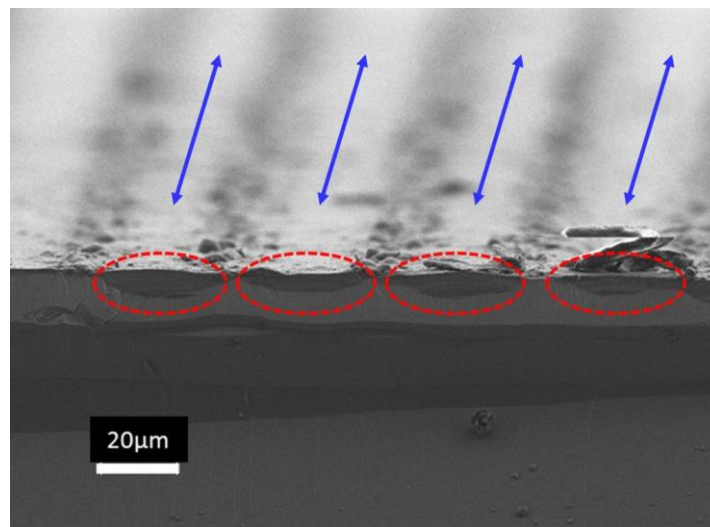


Fig. 6.5. Laser-induced melting pool at the interface. The melted pools are labeled by red circles and the blue arrows indicate the laser scan path.

LBIC was performed to show the spatial variation of the photo-generated current in the sintered emitter layer. A green diode laser was used to extract this information. The beam was focused down to about a 25  $\mu\text{m}$  spot through a microscope objective. A combination of two neutral density filters and one polarizer was used to reduce the incident light intensity down to 15  $\mu\text{W}$  to avoid high level injection effects. The short circuit current was measured at each spot, which gives the information of the quality of that spot of the sintered film. The results are shown in Fig. 6.6. Spatial non-uniformity of the layer can be seen by the varying color intensity. On top of randomly distributed dark spots, equally spaced parallel darker and brighter lines can be observed (see inset of Fig. 6.6), which are formed by the laser beam scan pattern during sintering. The darker lines correspond to the laser sintering paths while the brighter ones correspond to the overlap regions between two adjacent laser scan lines. The thickness of the laser-sintered emitter varies from 150 nm to 1  $\mu\text{m}$ . The thinner parts are the laser scan path while the thicker parts are the overlap regions between two adjacent paths. The darker lines correspond to those thinner parts because the interface is either closer or within the junction and thus fewer photo-generated carriers are drifted across the junction and contribute to the photocurrent without suffering recombination at the interface. Therefore, less photocurrent was generated from those lines. The brighter lines correspond to the thicker parts of the film along the same logic. The LBIC results indicated that the sintered film was active under illumination and contributed to the photocurrent. Thus, the applicability of the layer in solar cell application was demonstrated.

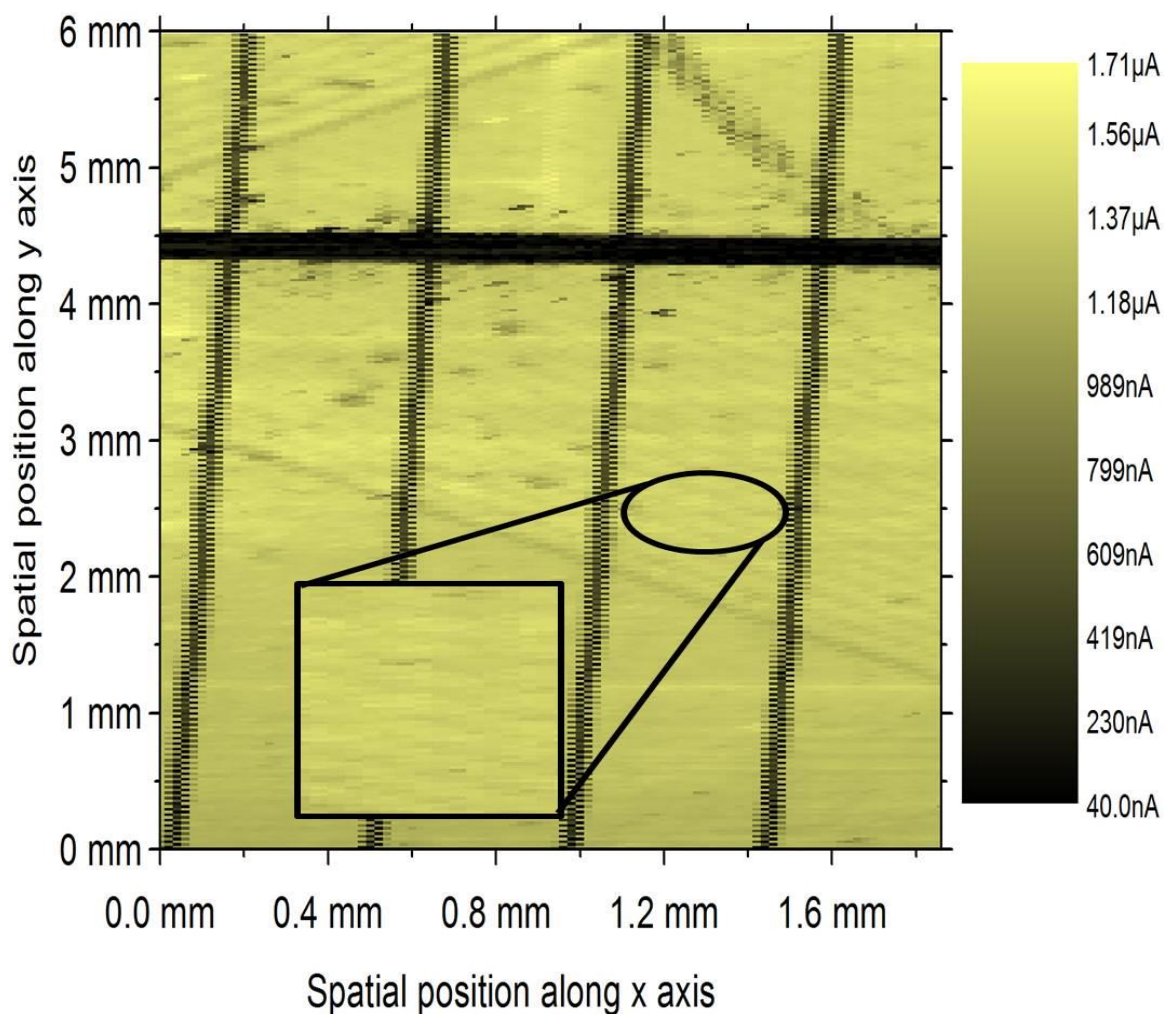


Fig. 6.6. LBIC results of the device with laser-sintered emitter. The solid black regions are the front metal contact areas. The inset shows the magnified image.

## 6.4 Summary

A low-cost approach for fabrication of Si thin films was demonstrated by laser sintering of Si nanoparticles. The application of sintered layers in optoelectronic devices was explored by fabricating a photovoltaic device which had the sintered layer as the emitter. Device performance was characterized using various methods. The sintered layer was shown to be photo-active. The

interfaces between particles in the sintered layer and the substrate were speculated to be the major reason for the low efficiency of the device. Further improvement could be attained through laser sintering parameter optimization, surface treatment prior to Si nanoparticle coating. Moreover, the cost can be further reduced and the fabrication steps can be simplified if doped Si nanoparticles are used.

## Bibliography

- [1]. S. M. Sze, "Physics of Semiconductor Devices", 2nd ed., Wiley, New York, 1999.
- [2]. H. Matsubara, T. Sasada, M. Takenaka, and S. Takagi, "Evidence of low interface trap density in GeO<sub>2</sub>/Ge metal-oxide-semiconductor structures fabricated by thermal oxidation", *Appl. Phys. Lett.*, vol. 93, pp. 032104 (2008).
- [3]. H. Shang, K-L. Lee, P. Kozlowski, C. D'Emic, I. Babich, E. Sikorski, M. Jeong, H. S. P. Wong, K. Guarini, and W. Haensch, "Self-aligned n-channel germanium MOSFETs with a thin Ge oxynitride gate dielectric and tungsten gate", *IEEE Electron Device Lett.*, vol. 25, pp. 135-137 (2004).
- [4]. K. Morii, T. Iwasaki, R. Nakane, M. Takenaka, and S. Takagi, "High performance GeO<sub>2</sub>/Ge nMOSFETs with source/drain junctions formed by gas phase doping", *Electron Device Meeting (IDEM), 2009 IEEE International*, pp. 681-684 (2009).
- [5]. C. H. Lee, T. Nishimura, N. Saido, K. Nagashio, K. Kita, and A. Toriumi, "Record-high electron mobility in Ge n-MOSFETs exceeding Si universality", *Electron Devices Meeting, 2009 IEEE International*, pp. 457-460 (2009).
- [6]. H. Wu, N. Conrad, W. Luo, and D. Ye, "First experimental demonstration of Ge CMOS Circuits", *Electron Device Meeting (IDEM), 2014 IEEE International*, pp. 227-230 (2014).
- [7]. M. Jutzi, M. Bettath, G. Wohl, M. Oehme, and E. Kasper, "Ge-on-Si vertical incidence photodiodes with 39-GHz bandwidth", *IEEE Photon. Tech. Lett.*, vol. 17, pp. 1510 (2005).
- [8]. M. Oehme, J. Werner, E. Kasper, M. Jutzi, and M. Berroth, "High bandwidth Ge p-i-n photodetector integrated on Si", *Appl. Phys. Lett.*, vol. 89, pp. 071117 (2006).

- [9]. M. Takenaka, K. Morii, M. Sugiyama, Y. Nakano, and S. Takagi, “Dark current reduction of Ge photodetector by GeO<sub>2</sub> surface passivation and gas-phase doping”, *Opt. Express*, vol. 20, pp. 8718 (2012).
- [10]. Y. Bao, K. Sun, N. Dhar and M. C. Gupta, “Germanium p-n junctions by laser doping for photonics/microelectronic devices”, *IEEE Photon. Technol. Lett.*, vol. 26, pp. 1422 (2014).
- [11]. B. Chen, W. Jiang, J. Yuan, A. L. Holmes Jr and B. M. Onat. “Demonstration of a Room Temperature InP-based Photodetector Operating beyond 3  $\mu\text{m}$ ”, *IEEE Photon. Technol. Lett.*, vol. 23, pp. 218-220 (2011).
- [12]. J. Yuan, B. Chen and A. L. Holmes Jr, “Near-infrared quantum efficiency of uncooled photodetectors based on InGaAs/GaAsSb quantum wells lattice-matched to InP”, *Electron. Lett.*, vol. 47, pp. 1144 – 1145 (2011).
- [13]. R. Duffy, M. Shayesteh, M. White, J. Kearney, and A. M. Kelleher, “Problems of n-type doped regions in germanium, their solutions and how to beat the ITRS roadmap”, *ECS Trans*, vol. 35 (2), pp. 185 (2011).
- [14]. B. P. Bob, A. Kohno, S. Chamvanichborikam, J. M. Warrender, and I. Umezu, “Fabrication and subband gap optical properties of silicon supersaturated with chalcogens by ion implantation and pulsed laser melting”, *J. Appl. Phys.*, vol. 107, pp. 123506 (2010).
- [15]. I. Umezu, J. M. Warrender, S. Charnvanichborikarn, A. Kohno, J. S. Williams, M. Tabbal, D. G. Papazoglou, X. C. Zhang, and M. J. Aziz, “Emergence of very broad infrared absorption band by hyperdoping of silicon with chalcogen”, *J. Appl. Phys.*, vol. 113, pp. 213501 (2013).
- [16]. A. J. Said, D. Recht, J. T. Sullivan, J. M. Warrender, T. Buonassisi, P. D. Persans, and M. J. Aziz, “Extended infrared photoresponse and gain in chalcogen-supersaturated silicon photodiodes”, *Appl. Phys. Lett.*, vol. 99, pp. 073503 (2011).

- [17]. A. Hauser, G. Hahn, M. Spiegel, H. Feist, O. Breitenstein, J. P. Rakotoniaina, P. Fath, and E. Bucher, "Comparison of different techniques for edge isolation", *Proc. 17th European Photovoltaic Solar Energy Conference*, pp. 1739-1741 (2001).
- [18]. U. Jager, M. Okanovic, M. Hortheis, A. Crohe, and R. Preu, "Selective emitter by laser doping from phosphosilicate glass", *24<sup>th</sup> European PV Solar Energy Conference and Exhibition*, Sept. 21-25, Hamburg, Germany (2009).
- [19]. J. J. Hank, "Laser processing technique for fabricating series-connected and tandem junction series-connected solar cells into a solar battery", U. S. Patent, No. 4,292,092, issued September 29, 1981.
- [20]. K. Lee, J-K. Lim, S-K. Kim, I-S. Moon, J-W. Seo, W-J. Lee, and E-C. Cho, "Impact of laser hole drilling on the breakage rate of multicrystalline silicon wafers", *Proc. 37th IEEE Photovoltaic Specialists Conference*, pp. 1473-1476 (2011).
- [21]. V. V. Iyengar, B. K. Nayak, and M. C. Gupta, "Optical properties of silicon light trapping structures for photovoltaics", *Sol. Energ. Mat. Sol. C.*, vol. 94, pp. 2251-2257 (2010).
- [22]. P. Papet, O. Nichiporuk, A. Kaminski, Y. Rozier, J. Kraiem, J. F. Lelievre, A. Chaumartin, A. Fave and M. Lemiti, "Pyramidal texturing of silicon solar cell with TMAH chemical anisotropic etching", *Sol. Energ. Mat. Sol. C.*, vol. 90, pp. 2319-2328 (2006).
- [23]. J. Leem, Y. Song and J. Yu, "Broadband antireflective germanium surfaces based on subwavelength structures for photovoltaic cell applications", *Opt. Express*, vol. 19, pp. 26308-263167 (2011).
- [24]. B. Chen, Q. Zhou, D. C. McIntosh, J. Yuan, Y. Chen, W. Sun, J. C. Campbell and A. L. Holmes Jr, "Natural lithography nano-sphere texturing as antireflective layer on InGaAs PIN photodiodes", *Electron. Lett.*, vol. 48, pp.1340-1341 (2012).

- [25]. Q. Zhou, D. C. McIntosh, Y. Chen, W. Sun, Z. Li and J. C. Campbell, "Nanosphere natural lithography surface texturing as anti-reflective layer on SiC photodiodes", *Opt. Express*, vol. 19, pp. 23664-23670 (2011).
- [26]. V. V. Iyengar, B. K. Nayak and M. C. Gupta, "Ultralow reflectance metal surfaces by ultrafast laser texturing", *Appl. Opt.*, vol. 49, pp. 5983-5988 (2010).
- [27]. B. K. Nayak and M. C. Gupta, "Micro texturing of silicon using pulsed N<sub>2</sub> – laser and formation mechanism", *Appl. Opt.*, vol.51, pp. 114-120 (2012).
- [28]. B. K. Nayak, M. C. Gupta and K. W. Kolasinski, "Spontaneous formation of nanospiked microstructures in germanium by femtosecond laser irradiation", *Nanotechnology*, vol. 18, pp. 195302 (2007).
- [29]. V. V. Iyengar, B. K. Nayak, and M. C. Gupta, "Silicon PV devices based on a single step for doping, anti-reflection and surface passivation", *Sol. Energ. Mat. Sol. C.*, vol. 94, pp. 2205 (2010).
- [30]. Z. Li, B. K. Nayak, V. V. Iyengar, D. McIntosh, Q. Zhou, M. C. Gupta, and J. C. Campbell, "Laser-textured silicon photodiode with broadband spectral response", *Appl. Opt.*, vol. 50, pp. 2508-2511 (2011).
- [31]. C. H. Poon, L. S. Tan, B. J. Cho and A. Y. Du, "Dopant loss mechanism in n<sup>+</sup>/p germanium junctions during rapid thermal annealing", *J. Electrochem. Soc.*, vol. 152, pp. G895-G899 (2005).
- [32]. M. C. Gupta, L. Wang, C. Rothenback, and K. Sun, "Pumped Solid State Lasers for Surface Microtexture", *J. Laser Micro Nanoeng.*, vol. 8, pp. 124-130 (2013).

- [33]. G. R. Savich, J. R. Pedrazzani, S. Maimon, and G. W. Wicks, "Suppression of surface leakage currents using molecular beam epitaxy-grown unipolar barriers", *J. Vac. Sci. Technol. B*, vol. 28, pp. C3H18 (2010).
- [34]. Claverie, S. Koffel, N. Cherkashin, G. Benassayag and P. Scheiblin, "Amorphization, recrystallization and end of range defects in germanium", *Thin Solid Films*, vol. 518, pp. 2307-2313 (2010).
- [35]. Chen, J. Yuan and A. L. Holmes Jr, "Dark Current Modeling of InP based SWIR and MWIR InGaAs/GaAsSb Type-II MQW Photodiodes", *Opt. Quant. Electron.*, vol. 45, pp. 271-277 (2013).
- [36]. Y. W. Ok, A. Rohatgi, Y. Kil, S. Park, D. Kim, J. Lee and C. Choi, "Abnormal dopant distribution in  $\text{POCl}_3$  – diffused  $n^+$  emitter of textured silicon solar cells", *IEEE Electron Device Lett.*, vol. 32, pp. 351 (2011).
- [37]. L. Colace, G. Masini, G. Assanto, Hsin-Chiao Luan, K. Wada, and L. C. Kimerling, "Efficient high-speed near-infrared Ge photodetectors integrated on Si substrates", *Appl. Phys. Lett.*, vol. 76, pp. 1231 (2000).
- [38]. C. O. Chui, K. Gopalakrishnan, P. B. Griffin, J. D. Plummer, and K. C. Saraswat, "Activation and diffusion studies of ion-implanted p and n dopants in germanium," *Appl. Phys. Lett.*, vol. 83, pp. 3275 (2003).
- [39]. M. Takenaka, K. Morii, M. Sugiyama, Y. Nakano, and S. Takagi, "Gas phase doping of arsenic into (100), (110), (111) germanium substrates using a metal-organic source," *Jpn. J. Appl. Phys.*, vol. 50, pp. 010105 (2011).

- [40]. N. E. Posthuma, J. Heide, F. Flamand, and J. Poortmans, "Emitter formation and contact realization by diffusion for germanium photovoltaic devices," *IEEE Trans. Electron Devices*, vol. 54, pp. 1210-1215 (2007).
- [41]. R. Duffy, M. Shayesteh, M. White, J. Kearney, and A. M. Kelleher, "Problems of n-type doped regions in germanium, their solutions and how to beat the ITRS roadmap," *ECS Trans.*, vol. 35 (2), pp. 185-192 (2011).
- [42]. M. Jamil, J. Mantey, E. U. Onyegam, G. D. Carpenter, E. Tutuc, and S. K. Banerjee, "High-Performance Ge nMOSFETs with  $n^+$ -p junctions formed by spin-on-dopant," *IEEE Electron Device Lett.*, vol. 32, pp. 1203-1205 (2011).
- [43]. N. Ioannou, D. Skarlatos, C. Tsamis, C. A. Krontiras, S. N. Georga, A. Christofi, and D. S. McPhail, "Germanium substrate loss during low temperature annealing and its influence on ion-implanted phosphorous dose loss," *Appl. Phys. Lett.*, vol. 93, pp. 101910 (2008).
- [44]. S. K. Wang, K. Kita, C. H. Lee, T. Tabata, T. Nishimura, K. Nagashio, and A. Toriumi, "Desorption kinetics of GeO from GeO<sub>2</sub>/Ge structure," *J. Appl. Phys.*, vol. 108, pp. 054104 (2010).
- [45]. G. Micard, A. Dastgheib-Shirazi, B. Raabe, and G. Hahn, "Diffusivity analysis of POCl<sub>3</sub> emitter SIMS profiles for semi empirical parametrization in Sentauros process," *Proc. 26th EU-PVSEC*, pp. 1446-1450 (2011).
- [46]. V. V. Iyengar, and M. C. Gupta, "Laser assisted doping for photovoltaic applications," *J. Laser Micro Nanoeng.*, vol. 4 (2), pp. 89-94 (2009).
- [47]. S. J. Eisele, T. C. Roder, J. R. Kohler, and J. H. Werner, "18.9% efficient full area laser doped silicon solar cell," *Appl. Phys. Lett.*, vol. 95 (13), pp. 133501 (2009).

- [48]. N. E. Posthuma, J. van der Heide, G. Flamand and J. Poortmans, "Development of low cost germanium photovoltaic cells for application in TPV using spin on diffusants", *AIP Conf. Proc.*, vol. 738, pp. 337 (2004).
- [49]. C. Wang, C. Li, S. Huang, W. Lu, G. Yan, M. Zhang, H. Wu, G. Lin, J. Wei, W. Huang, H. Lai, and S. Chen, "Phosphorus diffusion in germanium following implantation and excimer laser annealing," *Appl. Surf. Sci.*, vol. 300, pp. 208-212 (2014).
- [50]. S. Adachi, "Optical Constants of Crystalline and Amorphous Semiconductors", Kluwer Academic Publishers, Boston, Dordrecht & London, 43-48 (1999).
- [51]. M. Jamil, "Germanium and Epitaxial Ge:C Devices for CMOS Extension and Beyond", Ph.D. dissertation, Dept. Elect. Eng. The Univ. of Texas at Austin, Austin, USA (2011).
- [52]. B. Chen, J. Yuan, and A. L. Holmes Jr, "Dark Current Modeling of InP based SWIR and MWIR InGaAs/GaAsSb Type-II MQW Photodiodes", *Opt. Quant. Electron.*, vol. 45, pp. 271-277 (2013).
- [53]. M. Sher, and E. Mazur, "Intermediate band conduction in femtosecond-laser hyperdoped silicon", *Appl. Phys. Lett.*, vol. 105, pp. 032103 (2014).
- [54]. K. Guenther, T. Gimpel, S. Kontermann, and W. Schade, "Investigation of the sulfur doping profile in femtosecond-laser processed silicon", *Appl. Phys. Lett.*, vol. 102, pp. 202104 (2013).
- [55]. B. P. Bob, A. Kohno, S. Chamvanichborikam, J. M. Warrender, and I. Umezu, "Fabrication and subband gap optical properties of silicon supersaturated with chalcogens by ion implantation and pulsed laser melting", *J. Appl. Phys.*, vol. 107, pp. 123506 (2010).

- [56]. J. Mathews, A. J. Akey, D. Recht, G. Malladi, H. Efstathiadis, M. J. Aziz, and J. M. Warrender, "On the limits to Ti incorporation into Si using pulsed laser melting", *Appl. Phys. Lett.*, vol. 104, pp. 112102 (2014).
- [57]. K. Sanchez, I. Aguilera, P. Palacios, and P. Wahnou, "Formation of a reliable intermediate band in Si heavily coimplanted with chalcogens (S, Se, Te) and group III elements (B, Al)", *Phys. Rev. B.*, vol. 82, pp. 165201 (2010).
- [58]. M. Tabbal, T. Kim, J. M. Warrender, M. J. Aziz, and B. L. Cardozo, "Formation of single crystal sulfur supersaturated silicon based junctions by pulsed laser melting", *J. Vac. Sci. Technol. B.*, vol. 25, pp. 1847-1852 (2007).
- [59]. J. E. Carey, C. H. Crouch, M. Shen, and E. Mazur, "Visible and near-infrared responsivity of femtosecond-laser microstructured silicon photodiodes", *Opt. Lett.*, vol. 30, pp. 1773-1775 (2005).
- [60]. Z. Huang, J. E. Carey, M. Liu, X. Guo, and E. Mazur, "Microstructured silicon photodetector", *Appl. Phys. Lett.*, vol. 89, pp. 033506 (2006).
- [61]. M. T. Winkler, D. Recht, M. Sher, A. J. Said, E. Mazur, and M. J. Aziz, "Insulator-to-metal transition in sulfur-doped silicon", *Phys. Rev. Lett.*, vol. 106, pp. 178701 (2011).
- [62]. D. Recht, M. J. Smith, S. Charnvanichborikarn, J. T. Sullivan, M. T. Winkler, J. Mathews, J. M. Warrender, T. Buonassisi, J. S. Williams, S. Gradecak, and M. J. Aziz, "Supersaturating silicon with transition metals by ion implantation and pulsed laser melting", *J. Appl. Phys.*, vol. 114, pp. 124903 (2013).
- [63]. M. T. Winkler, M. J. Sher, Y. T. Lin, M. J. Smith, H. Zhang, S. Gradecak, and E. Mazur, "Studying femtosecond-laser hyperdoping by controlling surface morphology", *J. Appl. Phys.*, vol. 111, pp. 093511 (2012).

- [64]. B. P. Bob, A. Kohno, S. Charnvanichborikarn, J. M. Warrender, I. Umezu, M. Tabbal, J. S. Williams, and M. J. Aziz, "Fabrication and subband gap optical properties of silicon supersaturated with chalcogens by ion implantation and pulsed laser melting", *J. Appl. Phys.*, vol. 107, pp. 123506 (2010).
- [65]. K. Morii, T. Iwasaki, R. Nakane, M. Takenaka, and S. Takagi, "High performance GeO<sub>2</sub>/Ge nMOSFETs with source/drain junctions formed by gas phase doping", *Electron Device Meeting (IDEM), 2009 IEEE International*, pp. 681-684 (2009).
- [66]. B. Chen, and A. L. Holmes, "InP-based short-wave infrared and midwave infrared photodiodes using a novel type-II strain-compensated quantum well absorption region", *Opt. Lett.*, vol. 38, pp. 2750-2753 (2013).
- [67]. H. G. Grimmeiss, L. Montelius, and K. Larsson, "Chalcogens in germanium", *Phys. Rev. B.*, vol. 37, pp. 6916-6928 (1988).
- [68]. K. W. Kolasinski, D. Mills, and M. Nahidi, "Laser assisted and wet chemical etching of silicon nanostructures", *J. Vac. Sci. Technol. A*, vol.24, pp. 1474-1479 (2006).
- [69]. M. J. Aziz, "Model for solute redistribution during rapid solidification", *J. Appl. Phys.*, vol. 53, pp. 1158-1168 (1982).
- [70]. J. L. P. Castineira, L. M. R. Scolfaro, and J. R. Leite, Impurity levels of substitutional chalcogens-doped Ge", *Solid State Commun.*, vol. 79 (7), pp. 557-560 (1991).
- [71]. A. Dimoulas, P. Tsipas, and A. Sotiropoulos, "Fermi-level pinning and charge neutrality level in germanium", *Appl. Phys. Lett.*, vol. 89, pp. 252110 (2006).
- [72]. B. Chen, J. Yuan and A. L. Holmes Jr, "Dark Current Modeling of InP based SWIR and MWIR InGaAs/GaAsSb Type-II MQW Photodiodes", *Opt. Quant. Electron.*, vol. 45, pp. 271-277 (2013).

- [73]. S. Rein, T. Rehr, W. Warta, and S. W. Glunz, "Lifetime spectroscopy for defect characterization: Systematic analysis of the possibilities and restrictions", *J. Appl. Phys.*, vol. 91, pp. 2059-2070 (2002).
- [74]. S. K. Srivastava, P. Singh, M. Yameen, P. Prathap, C. M. S. Rauthan, Vadana, and P. K. Singh, "Antireflective ultra-fast nanoscale texturing for efficient multi-crystalline silicon solar cells", *Sol. Energy*, vol. 115, pp. 656-666 (2015).
- [75]. W. Wang, M. Tsai, J. Yang, C. Hsu, and M. Chen, "Efficiency enhancement of nanotextured black silicon solar cells using Al<sub>2</sub>O<sub>3</sub>/TiO<sub>2</sub> dual-layer passivation stack prepared by atomic layer deposition", *ACS Appl. Mater. Inter.*, vol. 7, pp. 10228-10237 (2015).
- [76]. M. Park, C. Harrison, P. M. Chaikin, R. A. Register, and D. H. Adamson, "Block copolymer lithography: periodic arrays of ~ 1011 holes in 1 square centimeter", *Science*, vol. 276, pp. 1401-1404 (1997).
- [77]. A. Rahman, A. Ashraf, H. Xin, X. Tong, P. Sutter, M. D. Eisaman, and C. T. Black, "Sub-50-nm self-assembled nanotextures for enhanced broadband antireflection in silicon solar cells", *Nat. Commun.*, doi: 10.1038/ncomms6963 (2015).
- [78]. L. Sainiemi, V. Jokinen, A. Shah, M. Shpak, S. Aura, P. Suvanto, and S. Franssila, "Non-reflecting silicon and polymer surfaces by plasma etching and replication", *Adv. Mater.*, vol. 23, pp. 122-126 (2011).
- [79]. J. Seo, J. Park, S. Kim, B. Park, Z. Ma, J. Choi, and B. Ju, "Nanopatterning by laser interference lithography: applications to optical devices", *J. Nanosci. Nanotechnol.*, vol. 14, pp. 1521-1532 (2014).

- [80]. M. A. Sheehy, L. Winston, J. E. Carey, C. M. Friend, and E. Mazur, "Role of background gas in the morphology and optical properties of laser-microstructured silicon", *Chem. Mater.*, vol. 17, pp. 3582-3586 (2005).
- [81]. P. Bellanger, M. Grau, A. Sow, A. Kaminski, D. Blangis, J. M. Serra, A. Vallera, S. Dubois, and A. Straboni, "Multicrystalline silicon wafers prepared by sintering of silicon bed powders and re-crystallization using ZMR", *24th European Photovoltaic Solar Energy Conference*, 21-25 September 2009, Hamburg, Germany.
- [82]. D. J. Rowe, R. J. Anthony, and U. R. Kortshagen, "Plasma assisted synthesis of silicon nanocrystals for thin film solar cells", *20th International Symposium on Plasma Chemistry*, 24-29 July 2011, Philadelphia, USA.
- [83]. B. K. Nayak, V. V. Iyengar, and M. C. Gupta, "Efficient light trapping in silicon solar cells by ultrafast-laser-induced self-assembled micro/nano structures", *Prog. Photovolt: Res. Appl.*, vol. 19, pp. 631-639 (2011).
- [84]. J. E. Mahan, T. W. Ekstedt, R. I. Frank, and R. Kaplow, "Measurement of minority carrier lifetime in solar cells from photo-induced open-circuit voltage decay", *Electron Devices, IEEE Trans on*, vol. 26, pp. 733-739 (1979).

## List of Publications

- [1]. K. Sun, Y. Bao, and M. C. Gupta, “Laser doping of germanium for photodetector applications”, *Proc. of SPIE*, vol. 9180, doi: 10.1117/12.2064283 (2014).
- [2]. Y. Bao, K. Sun, N. Dhar and M. C. Gupta, “Germanium p-n junctions by laser doping for photonics/microelectronic devices”, *IEEE Photon. Technol. Lett.*, vol. 26, pp. 1422 (2014).
- [3]. M. C. Gupta, L. Wang, C. Rothenbach, and K. Sun, “Diode pumped solid state lasers for surface microtexture”, *J. Laser Micro. Nanoen.*, vol. 8, pp. 124 – 130 (2013).
- [4]. B. K. Nayak, K. Sun, C. Rothenbach, and M. C. Gupta, “Self-organized 2D periodic arrays of nanostructures in silicon by nanosecond laser irradiation”, *Appl. Opt.*, vol. 50, pp. 2349-2355 (2011).
- [5]. B. J. Foley, D. L. Marlowe, K. Sun, W. A. Saidi, L. Scudiero, M. C. Gupta, and J. Choi, “Temperature dependent energy levels of methylammonium lead iodide perovskite”, *Appl. Phys.*, vol. 106, pp. 243904 (2015).
- [6]. K. Sun, and M. C. Gupta, “Sulfur-hyperdoping of germanium by pulsed laser”, to be published.